# Probing the X-ray Spectral and Timing Behaviour of the High-Mass X-ray Binaries EXO 2030+375 and Vela X-1

**Dissertation**

der Mathematisch-Naturwissenschaftlichen Fakultät
der Eberhard Karls Universität Tübingen
zur Erlangung des Grades eines
Doktors der Naturwissenschaften
(Dr. rer. nat.)

vorgelegt von
Yujia Du
aus Qiqihar/China

Tübingen
2025

Gedruckt mit Genehmigung der Mathematisch-Naturwissenschaftlichen Fakultät der Eberhard Karls Universität Tübingen.

| | |
|---|---|
| Tag der mündlichen Qualifikation: | 27.01.2026 |
| Dekan: | Prof. Dr. Thilo Stehle |
| 1. Berichterstatter/-in: | Prof. Dott. Andrea Santangelo |
| 2. Berichterstatter/-in: | Prof. Dr. Klaus Werner |

Ich erkläre, dass ich die zur Promotion eingereichte Arbeit mit dem Titel “Probing the X-ray Spectral and Timing Behaviour of the High-Mass X-ray Binaries EXO 2030+375 and Vela X-1” selbstständig verfasst, nur die angegebenen Quellen und Hilfsmittel benutzt und wörtlich oder inhaltlich übernommene Stellen als solche gekennzeichnet habe. Ich versichere an Eides statt, dass diese Angaben wahr sind und dass ich nichts verschwiegen habe. Mir ist bekannt, dass die falsche Abgabe einer Versicherung an Eides statt mit Freiheitsstrafe bis zu drei Jahren oder mit Geldstrafe bestraft wird.

| | |
|---|---|
| Ort/Place, Datum/Date | Unterschrift/Signature |

# Abstract

Accreting X-ray pulsars are high-mass X-ray binaries hosting a rotating, strongly magnetized neutron star that accretes matter from an optical companion. Although discovered about fifty years ago, many aspects of their emission remain puzzling. The X-ray radiation originates from the gravitational energy released by the accreted plasma, which is channeled by the magnetic field onto the neutron star's polar caps and thermalized into X-rays either upon impact with the stellar surface or within the accretion column. Many aspects of the emission from accreting X-ray pulsars remain poorly understood. Key open issues include the emission mechanism, the geometry and beaming pattern of the accretion structure, and the strength and configuration of the neutron star's magnetic field, as well as how it can be reliably measured.

This thesis presents a spectral and timing study of two accreting X-ray pulsars: the Be/X-ray binary EXO 2030+375 and the wind-fed system Vela X-1. The analysis of EXO 2030+375 is based on *Insight*-HXMT observations obtained during the 2021 Type II giant outburst and at the peak of a Type I outburst in 2022, while the analysis of Vela X-1 relies on long-term *Swift*/BAT monitoring data from 2005 to 2024 and *NuSTAR* observations from 2012 to 2024.

The *Insight*-HXMT observations enabled a comprehensive timing and spectral study of EXO 2030+375. During the 2021 giant outburst, pulse profiles were constructed at different luminosities and across multiple energy bands. The profiles exhibit a strong dependence on luminosity, with clear transitions in shape observed during the rising and decaying phases of the outburst, suggesting a change in the radiation beam pattern with luminosity. The profiles also show energy dependence, possibly due to variations in the beam pattern with photon energy and/or local absorption caused by the non-spherically symmetric distribution of matter within the system. The hardness-intensity diagrams suggests state transitions during the early and late phases of the outburst. These transitions coincide with the luminosity range at which the pulse profile shape changes occur, implying that the source reached the critical luminosity and switched between the super-critical and sub-critical accretion regimes. Both average and phase-resolved spectral analyses

were performed. The flux-resolved average spectra exhibit a stable spectral evolution with luminosity, while the phase-resolved analysis reveals that the dependence of spectral parameters on pulse phase varies with luminosity. Furthermore, the phase-resolved analysis performed during the 2021 giant outburst and the 2022 Type I outburst shows that the photon index reaches its maximum value around the main peak of the pulse profile.

Concerning Vela X-1, we investigate the long-term evolution of the cyclotron line energy, as well as the relationship between cyclotron line energy and luminosity. Based on archival *Swift*/BAT monitoring from 2005 to 2024, our results provide the confirmation that the long-term decay of the harmonic line energy ($E_{\mathrm{cyc,H}}$) in Vela X-1 has ended. We further report the first detection of a transient increase in $E_{\mathrm{cyc,H}}$ between 2020 and 2023, suggesting a sudden and significant change in the magnetic field configuration or accretion geometry. While previous studies found such variations only during the declining phase of long-term evolution, our results show that abrupt shifts can also occur when the cyclotron line is in a stable plateau, long-term plateau. No existing theoretical framework fully explains this behavior, and future observations of Vela X-1 and other sources (e.g., Her X-1, Cen X-3, 4U 1538-522) will be crucial for refining models of polar-cap dynamics and magnetic-field evolution. A pulse-to-pulse analysis of nine *NuSTAR* observations from 2012 to 2024 shows that $E_{\mathrm{cyc,H}}$ slightly decreases at low luminosities and flattens toward higher luminosities. The fundamental line energy ($E_{\mathrm{cyc,F}}$) remains nearly constant with time and luminosity.

# Zusammenfassung

Akkretierende Röntgenpulsare sind massereiche Röntgendoppelsterne, die einen rotierenden, stark magnetisierten Neutronenstern enthalten, der Materie von einem optischen Begleiter akkretiert. Obwohl sie bereits vor etwa fünfzig Jahren entdeckt wurden, sind viele Aspekte ihrer Emission nach wie vor ungeklärt. Die Röntgenstrahlung entsteht aus der Gravitationsenergie des akkretierten Plasmas, das durch das Magnetfeld auf die Magnetpole des Neutronensterns geleitet wird und dort beim Aufprall auf die Sternoberfläche oder innerhalb der Akkretionssäule in Röntgenstrahlung umgewandelt wird. Zahlreiche Eigenschaften der Emission solcher Systeme sind noch unzureichend verstanden. Zu den offenen Fragen gehören der Emissionsmechanismus, die Geometrie und das Strahlungsmuster der Akkretionsstruktur sowie die Stärke und Konfiguration des Magnetfelds des Neutronensterns und die Möglichkeiten, diese zuverlässig zu bestimmen.

Diese Dissertation präsentiert eine spektrale und zeitliche Untersuchung von zwei akkretierten Röntgenpulsaren: dem Be/X-ray-Doppelstern EXO 2030+375 und dem windgetriebenen System Vela X-1. Die Analyse von EXO 2030+375 basiert auf Beobachtungen mit Insight-HXMT während des großen Typ-II-Ausbruchs im Jahr 2021 und am Maximum eines Typ-I-Ausbruchs im Jahr 2022, während die Untersuchung von Vela X-1 auf langfristigen Swift/BAT-Überwachungsdaten (2005–2024) und NuSTAR-Beobachtungen (2012–2024) beruht.

Die HXMT-Beobachtungen ermöglichten eine umfassende spektrale und zeitliche Analyse von EXO 2030+375. Während des großen Ausbruchs im Jahr 2021 wurden Pulsprofile in verschiedenen Leuchtstärken und Energiebereichen erstellt. Die Profile zeigen eine starke Abhängigkeit von der Leuchtstärke mit deutlichen Formänderungen während der ansteigenden und abklingenden Phasen des Ausbruchs, was auf eine Änderung des Strahlungsmusters mit der Leuchtstärke hinweist. Ebenso zeigen die Profile eine Energieabhängigkeit, die möglicherweise auf Variationen des Strahlungsmusters mit der Photonenenergie und/oder auf lokale Absorptionseffekte durch die unsymmetrische Materieverteilung im System zurückzuführen ist. Das Härte-Intensitäts-Diagramm weist auf Zustandsübergänge in den frühen und späten Phasen des Ausbruchs hin. Diese Übergänge

fallen mit den Leuchtstärkebereichen zusammen, in denen Änderungen der Pulsprofilform auftreten, was darauf hindeutet, dass die Quelle die kritische Leuchtstärke erreicht und zwischen superkritischem und subkritischem Akkretionsregime wechselt. Sowohl spektrale Mittelanalysen als auch phasenaufgelöste Analysen wurden durchgeführt. Die flussaufgelösten mittleren Spektren zeigen eine stabile spektrale Entwicklung mit der Leuchtstärke, während die phasenaufgelöste Analyse zeigt, dass die Abhängigkeit der spektralen Parameter von der Pulsphase mit der Leuchtstärke variiert. Darüber hinaus zeigt die phasenaufgelöste Analyse während des großen Ausbruchs 2021 und des Typ-I-Ausbruchs 2022, dass der Photonenindex seinen Maximalwert in der Nähe des Hauptmaximums des Pulsprofils erreicht.

Für Vela X-1 wird die langfristige Entwicklung der Zyklotronlinienenergie sowie deren Beziehung zur Leuchtstärke untersucht. Basierend auf den BAT-Überwachungsdaten von 2005 bis 2024 bestätigen die Ergebnisse, dass der langfristige Abfall der harmonischen Linienenergie ($E_{\mathrm{cyc,H}}$) in Vela X-1 beendet ist. Zudem wird erstmals ein vorübergehender Anstieg von $E_{\mathrm{cyc,H}}$ zwischen 2020 und 2023 berichtet, was auf eine plötzliche Änderung der Magnetfeldkonfiguration oder der Akkretionsgeometrie hindeutet. Während frühere Studien solche Variationen nur während der abnehmenden Phase der langfristigen Entwicklung beobachteten, zeigen unsere Ergebnisse, dass abrupte Änderungen auch in stabilen, langzeitigen Plateaus auftreten können. Derzeit existiert kein theoretischer Rahmen, der dieses Verhalten vollständig erklären kann. Zukünftige Beobachtungen von Vela X-1 und anderen Quellen (z. B. Her X-1, Cen X-3, 4U 1538-522) werden entscheidend sein, um Modelle der Polar-Cap-Dynamik und der Magnetfeldentwicklung weiter zu verfeinern. Eine Puls-zu-Puls-Analyse von neun NuSTAR-Beobachtungen (2012–2024) zeigt, dass $E_{\mathrm{cyc,H}}$ bei niedrigen Leuchtstärken leicht abnimmt und sich bei höheren Leuchtstärken abflacht. Die fundamentale Linienenergie ($E_{\mathrm{cyc,F}}$) bleibt über Zeit und Leuchtstärke hinweg nahezu konstant.

# 0

# CONTENTS

# List of Acronyms and Abbreviations

**BAT** Burst Alert Telescope (onboard *Swift*)

**BeXRB** Be/X-ray Binary

**BH** Black Hole

**CRSF** Cyclotron Resonance Scattering Feature

**eXTP** enhanced X-ray Timing and Polarimetry Mission

**FoV** Field of view

**HE** High Energy telescope (onboard HXMT)

**HID** Hardness-Intensity Diagram

**HMXB** High-Mass X-ray Binary

**HXMT** Hard X-ray Modulation Telescope

**IXPE** Imaging X-ray Polarimetry Explorer

**LE** Low Energy telescope (onboard HXMT)

**LMXB** Low-Mass X-ray Binary

**NuSTAR** Nuclear Spectroscopic Telescope ARray

**ME** Medium Energy telescope (onboard HXMT)

**MJD** Modified Julian Date

**NS** Neutron Star

**PHA** Pulse Height Amplitude

**PI** Pulse Invariant

**TOV** Tolman-Oppenheimer-Volkoff

**WD** White Dwarf

**XRB** X-Ray Binary

**XRP** X-Ray Pulsar

To my parents, for their endless love and support.

# 0

# ACKNOWLEDGMENTS

Many people have contributed to this work, and I would like to thank all of them for making this thesis possible. First and foremost, I am deeply grateful to Prof. Dr. Andrea Santangelo for his wise and continuous supervision throughout the years, from my Master's studies to my PhD. I also sincerely thank Dr. Lorenzo Ducci, my co-supervisor, for always being approachable and responsive to my questions. I am especially thankful to Prof. Dr. Long Ji, who supervised my Master's thesis and co-authored my papers. Despite the time difference and long distance between us, he was always available for discussions and support.

This thesis is based on several published papers and would not have been possible without the contributions of my co-authors: Prof. Dr. Andrea Santangelo, Dr. Lorenzo Ducci, Prof. Dr. Long Ji, Dr. Pengju Wang, Dr. Lingda Kong, and Prof. Dr. Qingcui Bu. I am especially grateful to Dr. Pengju Wang, who consistently supported me and generously shared his ideas during the discussions of the papers. His openness and willingness to engage in thoughtful conversations were invaluable throughout this work. I also thank the members of the institute for the friendly and open working environment at IAAT. Sharing an office with Dr. Nhan Nguyen and Dr. Michailidis Miltiadis made my time there pleasant and enjoyable. I am grateful to Dr. Menglei Zhou and Dr. Honghui Liu, whose generous help and support have been invaluable to me during my time here. My sincere thanks also go to Dr. Santina Piranio and Sabine Lauer, whose timely kindness and help during difficult moments meant a great deal to me.

I would also like to thank my dear friends, Dr. Jianfeng Guo, Yuhan Guo, and Yuqiao Yang. You brought color and joy into my life, and without your companionship, I could not have completed the final stages of this thesis with such ease and happiness. Last but most importantly, I want to thank my parents for their unwavering support – both material and emotional – in everything I have chosen to pursue. Without your help, none of this would have been possible.

# 1

# INTRODUCTION

## 1.1 Stellar evolution and the origin of Neutron Stars

A star can be described as a self-gravitating sphere of high-temperature plasma, in which the inward gravitational force is balanced by the outward thermal pressure of the plasma. One of the most remarkable thermodynamic properties of such a system is its negative heat capacity. In contrast to ordinary systems, where energy loss leads to cooling, a star contracts when it loses energy, and this contraction raises its internal temperature. The key to the formation and evolution of stars is the contraction of gas driven by gravity and the initiation of nuclear fusion.

As primordial gas clouds collapse under their own gravity, the temperature and density in the core gradually increase. When the central conditions become sufficiently extreme, hydrogen nuclei begin to fuse into helium, releasing energy that provides the necessary pressure to counteract further gravitational collapse. At this stage, the object transitions from a protostar to a main-sequence (MS) star, achieving hydrostatic equilibrium between the outward thermal pressure and the inward gravitational pull. The main-sequence corresponds to a well-defined, continuous band on the Hertzsprung-Russell (HR), which plots stellar luminosity against surface temperature (Hertzsprung, 1911), as shown in Figure 1.1. During the MS phase, the star steadily fuses hydrogen into helium in its core, radiating energy and gradually contracting until its central hydrogen supply is exhausted. Since stars are predominantly composed of hydrogen, this phase constitutes the majority of their lifetimes. Once the star has settled onto the MS, its luminosity and effective temperature remain nearly constant for most of its lifetime. The duration of the MS phase is governed by the nuclear timescale, which is determined by the star's total mass and luminosity (Lipunov, 1987),

$$T_{\mathrm{MS}} = \frac{E}{L} = \frac{0.007\,(0.1 \times M)c^2}{L}. \tag{1.1}$$

As the hydrogen in the core becomes exhausted, the rate of nuclear energy generation decreases, leading to a drop in thermal pressure. Consequently, the core begins to contract under gravity. This contraction increases the temperature and density in the core, eventually reaching conditions sufficient to ignite helium fusion, converting helium into carbon and oxygen. At the same time, the hydrogen continues to burn in the outer layers of the star, providing enough energy to balance the gravitational forces. The excess energy generated in the core results in the expansion of the star's outer layers. At this stage, the star

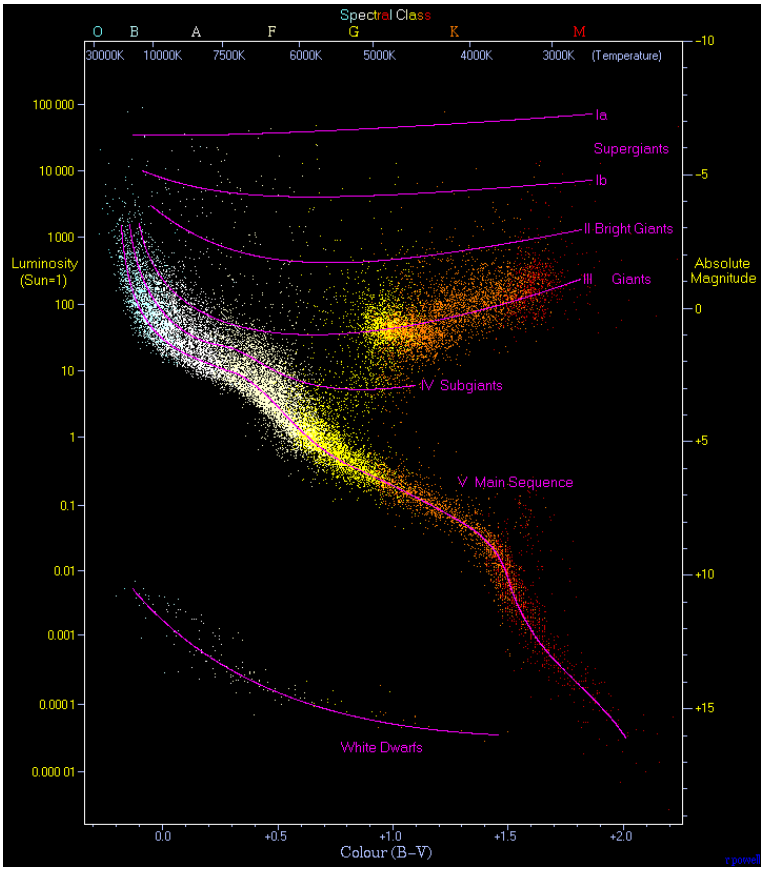


**Figure 1.1:** Hertzsprung–Russell (HR) diagram showing stellar luminosity versus colour. The main sequence extends from hot, luminous stars in the upper left to cool, faint stars in the lower right. White dwarfs occupy the lower-left region, while giants and supergiants lie above the main sequence. The Sun is located on the main sequence at $L = 1\,L_\odot$, $B - V = 0.66$, $T = 5780\,K$. Figure from `http://www.atlasoftheuniverse.com/hr.html` .

departs from the MS and evolves toward the giant branch of the HR diagram, becoming a red giant or supergiant depending on its initial mass.

The death of stars is of particular importance, as it gives rise to the three types of compact objects that are central to high-energy astrophysics. If the stellar mass exceeds about $\sim 8\,M_\odot$, successive stages of nuclear burning and gravitational contraction continue until the core becomes dominated by iron, at which point further fusion no longer releases energy. The final outcome of the star is determined by its initial mass and metallicity.

Stars with initial masses up to $\lesssim 8\,M_\odot$ typically end their lives as white dwarfs (WDs), leaving behind compact remnants with masses below the Chandrasekhar limit ($\leq 1.4\,M_\odot$, Chandrasekhar 1931).

If the progenitor star is even more massive, in the range $M \lesssim 20\,M_\odot$, a neutron star (NS) will form (final mass $1.4\,M_\odot \leq M \leq 2.2\,M_\odot$). The formation process of a neutron star proceeds as follows: once the entire core is converted into iron, fusion can

no longer proceed, and the core collapses under gravity. Electron degeneracy pressure is insufficient to halt the collapse, and electrons are captured by protons through inverse beta decay, resulting in the formation of neutrons and a degenerate neutron gas. The core is thus transformed into a neutron star (NS). They have been found in two ways. First, as the central objects of radio pulsars, which are rapidly rotating and magnetized neutron stars. Second, as compact companions in X-ray binary systems, where X-rays are produced by matter accreting from the normal star onto the NS.

When the mass of the progenitor star is $\gtrsim 20\ M_\odot$ and the mass of compact remnant exceeds $3\ M_\odot$ (Tolman-Oppenheimer-Volkoff (TOV) limit, Oppenheimer & Volkoff 1939), a black hole (BH) will form. A review of BHs and NSs formation is given by Heger et al. (2003).

## 1.2 Accreting X-ray Pulsars

This PhD work focuses on accreting X-ray pulsars (XRPs), which are rotating, magnetized neutron stars in binary systems that emit periodic X-ray pulses powered by the accretion of matter from a companion star (see Figure 1.2). Their rich phenomenology and typically high flux levels have made them key targets of observational and theoretical studies since the advent of X-ray astronomy. A detailed review of XRPs and their observational properties can be found in Accreting Strongly Magnetized Neutron Stars: X-ray Pulsars by Mushtukov & Tsygankov, included in the Handbook of X- and Gamma-ray Astrophysics (Bambi & Santangelo, 2022). The first coherent X-ray pulsations from Cen X-3, were discovered in the early 1970s by the X-ray observatory *UHURU* and were interpreted as the result of accretion onto a strongly magnetized neutron star (Lamb et al., 1973). Despite decades of study, the XRPs systems remain highly complex, and the physical mechanisms underlying many of their properties are still under debate. In the following, I provide an overview of the main observational and theoretical properties of accreting XRPs that are relevant to my PhD research.

### 1.2.1 X-ray binaries

Roughly half of the stars in our Galaxy are part of binary systems. These systems consist of two gravitationally bound stars orbiting their common center of mass. X-ray binaries are typically classified according to the nature of the compact object and/or the evolutionary type of the donor star. The compact object may be a neutron star (neutron star X-ray binaries; NSXBs) or a black hole (black hole X-ray binaries; BHXBs or BHBs). Systems in which the accretor is a white dwarf are known as cataclysmic variables (CVs),

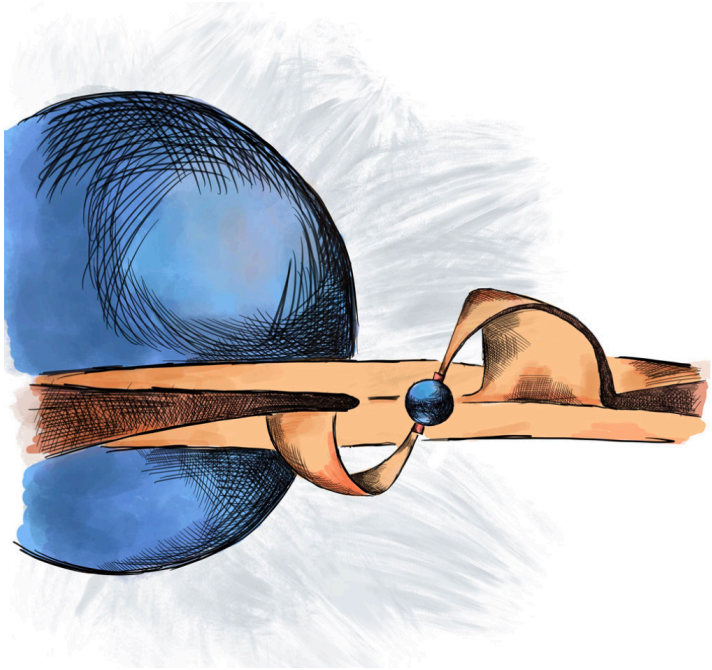

**Figure 1.2:** Schematic illustration of accretion geometry in X-ray pulsars. Figure from Tsygankov et al. (2022).

which share similar accretion processes but radiate predominantly at optical and ultraviolet wavelengths rather than in X-rays. Accretion of matter from the donor star onto the compact object gives rise to high-energy emission.

X-ray binaries are further divided into two main categories according to the mass of the donor star (Lewin et al., 1997). In high-mass X-ray binaries (HMXBs), the donor is an early-type (O or B) star with a typical mass of $\gtrsim 10\,M_\odot$. These systems are relatively young, and mass transfer occurs through either strong stellar winds or a circumstellar decretion disc (see details in Section 1.2.2; see also the Galactic HMXB catalogue by Neumann et al., 2023). In contrast, low-mass X-ray binaries (LMXBs) host a low-mass companion, usually a late-type star (spectral type A or later) or, in some cases, a white dwarf, with a mass of $\lesssim 1.5\,M_\odot$. These systems are generally older than HMXBs, and mass transfer primarily proceeds via Roche-lobe overflow (see details in Section 1.2.2; see also the Galactic LMXB catalogue by Avakyan et al., 2023).

One of the most numerous classes of XRPs is the systems with Be-type optical companions, known as Be/X-ray binaries (BeXRBs). The vast majority of known XRPs are transient sources that exhibit dramatic variations in X-ray luminosity, ranging from outburst timescales of weeks to months down to fluctuations occurring within seconds.

### 1.2.2 Mass transfer in binaries

Understanding the accretion mechanisms is essential for interpreting observational signatures and for probing the physical conditions in the extreme environments surrounding neutron stars. The distinctive nature of XRPs arises from their exceptionally strong magnetic fields, reaching up to $\sim 10^{12}$ G. Under such conditions, the accreted material forms a highly ionized plasma that is strongly influenced by the Lorentz force, which governs its motion within the magnetic field of the neutron star. At large distances from the compact object, the accretion flow is not significantly affected by the stellar magnetic field, and models describing disc or spherical accretion can be applied. However, in the vicinity of the NS, the magnetic field becomes sufficiently strong to dominate the dynamics of the inflowing plasma, channeling it along the field lines toward the magnetic poles and thus shaping the overall geometry of the accretion flow.

Three different ways of mass transfer can take place in XRPs: Roche lobe overflow (RLO, e.g. Her X-1), wind accretion (e.g. Vela X-1) and decretion disc in BeXRBs (e.g. V 0332+53). These mechanisms will be discussed below.

### Roche lobe overflow

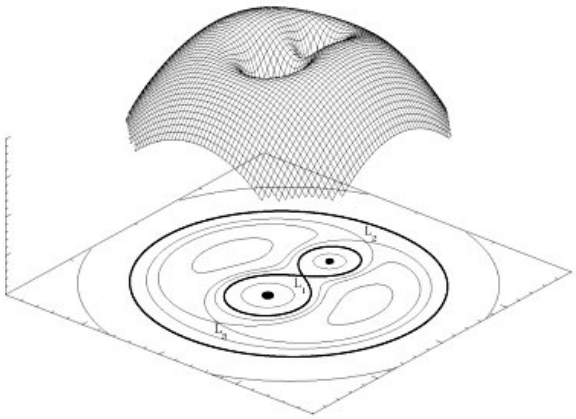

**Figure 1.3:** Three-dimensional representation of the potential field of a binary star system with a mass ratio of 2. The teardrop-shaped regions in the equipotential plot represent the Roche lobes of the two stars (thick lines). Points $L_1$, $L_2$, and $L_3$ denote the Lagrange points where the gravitational and centrifugal forces balance. Gas can flow from one star to the other through $L_1$ if the donor star fills its Roche lobe. Figure from https://hemel.waarnemen.com/Informatie/Sterren/hoofdstuk6.html#h6.2.

Mass transfer in a binary system can occur via Roche-lobe overflow through the inner Lagrangian point. In the Roche approximation (Hilditch, 2001), the gravitational field of

the system is modeled as that of two co-rotating point masses, $M_1$ and $M_2$, representing the stellar components and located at their respective centers of mass. The Roche potential is given by

$$\Phi = -\frac{GM_1}{r_1} - \frac{GM_2}{r_2} - \frac{\omega^2 r_3^2}{2}, \tag{1.2}$$

where $r_1$ and $r_2$ are the distances to the center of the stars, $\omega$ is the orbital angular velocity and $r_3$ is the orbital angular velocity. Within this approximation, a family of equipotential surfaces exists, some of which intersect at special locations known as Lagrangian points. At these points, the gravitational and centrifugal forces are in equilibrium, allowing matter to flow freely. In particular, the equipotential surface that passes through the inner Lagrangian point (commonly referred to as $L_1$) forms a characteristic two-lobed shape, with each lobe enclosing one of the stars. These lobes are known as the Roche lobes. When a star fills its Roche lobe, mass begins to transfer to its companion on a thermal timescale. This can alter the companion's structure and trigger nuclear burning. The orbit also shrinks, as the more massive star usually fills its lobe first. Continued mass transfer may eventually lead to the merger of the two stars. The rate of mass transfer through the inner Lagrangian point is determined by the stellar evolution of the companion and variations of the distance between companions in a system due to the mass exchange and energy losses due to gravitational waves.

### Wind accretion

Stellar wind accretion becomes the dominant mass transfer mechanism when the companion star does not fill its Roche lobe. This mode of accretion is particularly relevant for systems containing an early-type (O or B) star or a red giant as the donor, and a compact object in a relatively close orbit. Early-type stars are characterized by strong, radiatively driven stellar winds, with mass-loss rates reaching $\dot{M}_{\rm w} \sim 10^{-6}$–$10^{-5}\,M_\odot\,{\rm yr}^{-1}$ (i.e. $\sim 6\times10^{19}$–$6\times10^{20}\,{\rm g\,s}^{-1}$). The wind velocity is highly supersonic, typically on the order of $v_{\rm w} \sim 10^8\,{\rm cm\,s}^{-1}$ (Mushtukov & Tsygankov, 2023).

The accretion rate depends sensitively on the local wind density, relative velocity, and orbital separation, leading to pronounced variability in the observed X-ray luminosity. Wind-fed systems, such as Vela X-1 and GX 301-2, therefore exhibit strong short-term fluctuations and sporadic off-states, reflecting the inhomogeneous and clumpy nature of the stellar wind.

#### Mass transfer from the decretion disc in BeXRBs

Mass transfer from the decretion disc in BeXRBs is a complex accretion process that can only be properly investigated through detailed numerical simulations. These binaries usually have relatively wide and eccentric orbits, with typical orbital periods of several tens to hundreds of days and eccentricities around $e \sim 0.1$. The orbital angular momentum is often misaligned with the Be star's spin axis. When the compact object passes through or near the Be star's circumstellar decretion disc, part of the disc material can be captured by its gravitational field, leading to the formation of a transient accretion disc with highly variable and complex dynamics around the compact object (Martin et al., 2014).

Vast majority of known XRPs are transient sources and demonstrate dramatic variations of X-ray luminosity on time scales from weeks and months during the outbursts down to seconds. The interaction between the NS and the Be star's decretion disc gives rise to two distinct types of X-ray outbursts. Type I outbursts are relatively regular and moderate in intensity, typically occurring near periastron passage when the neutron star interacts with the outer edge of the decretion disc. In contrast, Type II outbursts are much brighter and longer, resulting from major structural changes or expansions of the decretion disc that allow enhanced mass transfer onto the NS independent of orbital phase (Reig, 2011).

### 1.2.3 Accretion onto highly magnetized Neutron Stars

When the accretion flow reaches the magnetosphere, it is highly ionized by the intense X-ray flux that is emitted from the immediate vicinity of the neutron star surface. It behaves as a plasma, and its dynamic is determined by the neutron star magnetic field, which channels the material all the way down to the magnetic poles. As the matter impacts the surface, it emits X-rays that constitute the main source of radiation from the system. The apparent luminosity of XRPs spans several orders of magnitude, from $\sim 10^{32}\,\mathrm{erg\,s^{-1}}$ up to $\sim 10^{41}\,\mathrm{erg\,s^{-1}}$.

Accretion onto a neutron star is an extremely efficient process in terms of energy release. When matter falls from the magnetospheric boundary down to the stellar surface, a significant fraction of its gravitational potential energy is converted into radiation. For a neutron star of mass $M$ and radius $R$, the accretion luminosity can be approximated as

$$L_{\mathrm{acc}} = \frac{GM\dot{M}}{R}, \tag{1.3}$$

An important reference point is the Eddington luminosity, which represents the maximum isotropic luminosity at which the outward radiation pressure acting on electrons balances

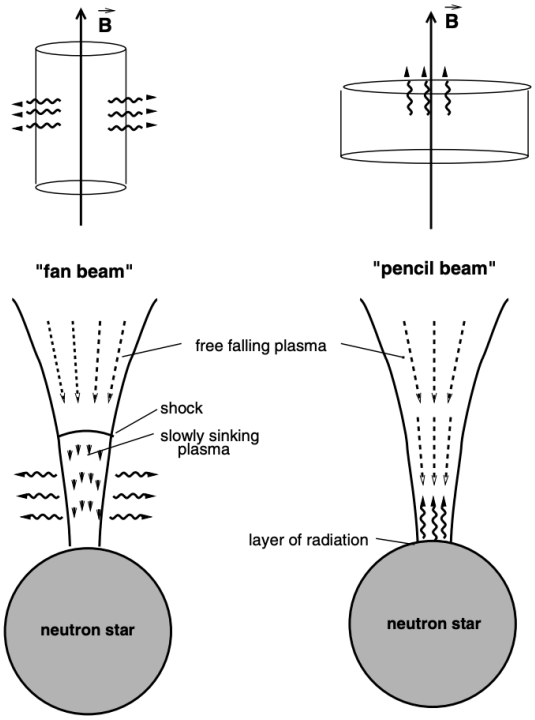


**Figure 1.4:** Accretion geometries and radiation patterns. Left: "fan beam"/cylinder geometry. Right: "pencil beam"/slab geometry (Schönherr et al., 2007).

the gravitational pull on protons in a fully ionized plasma. For a neutron star of mass $M$, this is given by

$$L_{\rm Edd} = \frac{4\pi G M m_{\rm p} c}{\sigma_{\rm T}} \approx 1.3 \times 10^{38} \left( \frac{M}{1.4\,M_{\odot}} \right) \ {\rm erg\,s^{-1}}. \tag{1.4}$$

where $m_{\rm p}$ is the proton mass and $\sigma_{\rm T} = 6.65 \times 10^{-25}\,{\rm cm}^2$ is the Thomson scattering cross section for electrons. Beyond this limit, and under the assumption of a steady and spherically symmetric accretion flow, the accretion rate cannot increase further, since a higher accretion rate would imply a radiation field strong enough to expel the inflowing plasma. However, because accretion is funneled onto a small area at the magnetic poles, the radiation escapes preferentially through the lateral walls of the accretion column rather than isotropically (Basko & Sunyaev, 1976). As a result, accreting pulsars may reach luminosities above the classical Eddington value, and the physically relevant transition is described by the critical luminosity $L_{\rm crit}$.

For typical neutron star parameters, Becker et al. (2012) derived the critical luminosity $L_{\rm crit}$ as (for typical neutron star parameters):

$$L_{\rm crit} \sim 1.5 \times 10^{37} B_{12}^{16/15} \ {\rm erg\,s^{-1}}, \tag{1.5}$$

where $B_{12}$ is the surface magnetic field strength in units of $10^{12}$ G. $L_{\rm crit}$ separates accretion column into two different patterns. When L $> L_{\rm crit}$, a radiation-dominated shock develops above the neutron star surface, giving rise to the formation of accretion columns at the magnetic poles (Inoue, 1975; Basko & Sunyaev, 1976; Becker et al., 2012; Mushtukov et al., 2015). In this regime, the deceleration of the infalling material below the shock is primarily governed by radiation pressure, causing the height of the column to increase with luminosity. These columns are confined by the strong magnetic field and supported by radiation pressure. Since the radiation can only escape through the lateral walls of the column, perpendicular to the magnetic field, a "fan-beam" emission pattern is produced, commonly associated with the appearance of double-peaked pulse profiles. When L $< L_{\rm crit}$, the height of the column decreases with luminosity, and flow might be decelerated either by Coulomb collisions in the NS atmosphere or by a collisionless shock above the surface (Basko & Sunyaev, 1976; Becker et al., 2012). In this subcritical regime, the top of the column is located nearer to the NS surface, where the plasma density is very high. At the same time, the photons can mainly escape from the top along the magnetic field as a "pencil-beam" pattern (Nelson et al., 1993). The beam pattern naturally determines the pulse profiles in accreting pulsars. Therefore, variations of their pulse profiles over a wide range of accretion luminosity can provide an evidence of changes in geometry of emitting region caused by changes of the mass accretion rate (see details in Section 1.2.4). Figure 1.4 illustrates the accretion geometry and radiation patterns on a neutron star.

Mushtukov et al. (2015) provided a numerical solution by calculating the luminosity for two scenarios: one with purely extraordinary polarization and another with an equal mix of ordinary and extraordinary polarization. The real critical luminosity value is expected to fall between the two cases.

### 1.2.4 Observational appearance

XRPs are among the brightest sources in the X-ray sky, enabling many observatories to collect extensive datasets spanning several decades. In this section, we focus on the key observational characteristics of XRPs that are directly relevant to the present study.

#### Pulse profile

Pulsations observed from XRPs are commonly attributed to a misalignment between the neutron star's rotation and magnetic axes. The resulting modulation in X-ray flux as a function of rotational phase is referred to as the pulse profile, typically obtained by folding the light curve over multiple spin periods to improve statistical significance. Pulse profiles

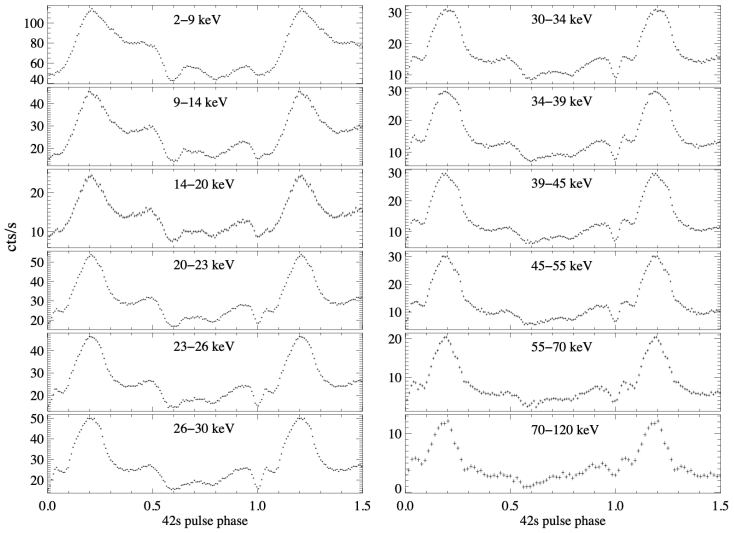


**Figure 1.5:** Energy resolved pulse profiles of EXO 2030+375 obtained with *JEM-X* (below 20 keV) and *IBIS/ISGRI* (above 20 keV) (Klochkov et al., 2008b).

in XRPs often exhibit complex morphologies, and their modeling remains challenging. The shape of the pulse profile can vary significantly with both photon energy and accretion luminosity.

Generally, accreting pulsars display more complex pulse profiles at lower energies, while higher-energy profiles tend to be simpler. Energy-dependent variations can be caused by the energy dependence of the emission beam pattern and/or local absorption effects due to the non-spherical distribution of matter in the binary system (see Fig. 1.5 as an example).

Changes in the pulse profile with luminosity (see Fig. 1.6 as an example) indicate the dependence of the geometry of the emission forming region and, therefore, of the beam pattern on the mass accretion rate.

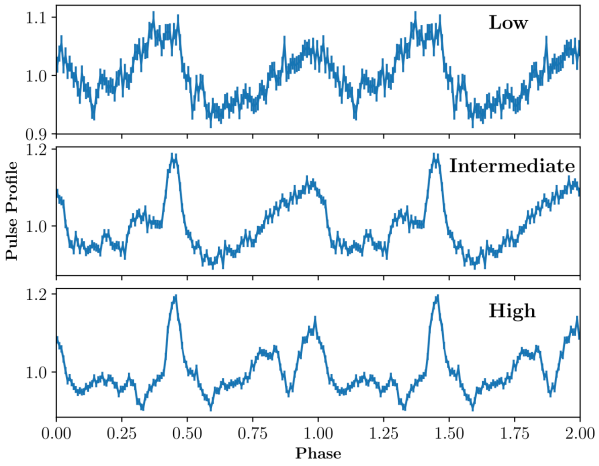


**Figure 1.6:** Pulse profiles of of 2S 1417−624 in the energy range of 25–100 keV observed with HXMT/HE in the low, intermediate, and high states, respectively (Ji et al., 2020).

Transitions from the subcritical to the supercritical accretion regime can lead to corresponding changes in beam geometry, and thus affect the observed pulse profiles. In several giant outbursts of accreting pulsars, changes in pulse shape have been suggested as indicators of transitions between the two regimes, and hence as potential signatures of the critical luminosity. Examples include 2S 1417-624 (Ji et al., 2020), 1A 0535+262 (Wang et al., 2022), and Swift J0243.6+6124 (Tsygankov et al., 2018), among others.

### Broadband energy spectra

A comprehensive model describing spectral formation in accreting pulsars over a wide range of accretion luminosities has not yet been established. In most studies, phenomenological models with simple parameterizations are used to reproduce the observed spectral shape and to infer the physical properties of the emission regions near the neutron star surface. Observationally, their broadband X-ray spectra are typically represented by an absorbed power law with an exponential high-energy cutoff.

The continuum emission is believed to originate from Compton scattering of thermal seed photons (Daugherty & Harding, 1986), bremsstrahlung (Meszaros, 1992), and cyclotron emission (see Staubert et al. (2019) for review), the latter discussed in detail in Section 1.2.4. Becker & Wolff (2007) developed a theoretical model describing both bulk and thermal Comptonization processes occurring in the accretion shock. In addition to the continuum components, many spectra also exhibit a soft excess at low energies, typically modeled with a blackbody component. A fluorescent iron K$\alpha$ line is often detected around 6.4 keV, originating from the reprocessing of hard X-rays in relatively cold material near the neutron star.

| Model | XSPEC notation | Description |
|---|---|---|
| Power law with high energy exponential cutoff | `CUTOFFPL` | Additive model for the continuum emission from XRPs. |
| A high energy cutoff | `HIGHECUT` | Multiplicative model for the continuum emission. Is used in combination with a power law component. |
| A blackbody spectrum | `BBODYRAD` | Additive blackbody component with normalization proportional to the surface area. Is used to account for the soft excess. |
| Gaussian absorption line | `GABS` | Another version of a multiplicative model for the cyclotron absorption line component. |
| Gaussian line profile | `GAU` | Additive model component in the form of gaussian line profile. Is used, e.g., to approximate iron fluorescent line emission. |
| A photoelectric absorption | `TBABS`, `PHABS` | Multiplicative model used to account for the photoelectric absorption. |

**Table 1.1:** XSPEC models commonly used for XRPs. Table from Mushtukov & Tsygankov (2023).

The list of the most commonly applied models available in the spectral fitting tool `XSPEC` Arnaud (1996) is presented in Table 1.1.

### Cyclotron Resonant Scattering Features (CRSF)

Cyclotron resonance scattering features (CRSFs) appear in the spectra of X-ray pulsars (XRPs) as a result of resonant Compton scattering in the presence of strong magnetic fields, typically occurring in the line-forming region near the neutron star surface. The existence of such features was theoretically predicted in the 1970s (Gnedin & Sunyaev, 1974) and soon confirmed observationally in Her X-1 through a balloon experiment (Trümper et al., 1977). They are produced in strong magnetic fields, where electrons are quantized onto Landau-levels. Photons with energies close to the Landau-levels are removed from the observed X-ray spectrum by scattering off these electrons. The centroid energy of a CRSF ($E_{\rm cyc}$) can be expressed as

$$E_{\rm cyc} \approx \frac{n}{(1+z)} 11.6\ [\text{keV}] \times B_{12}, \tag{1.6}$$

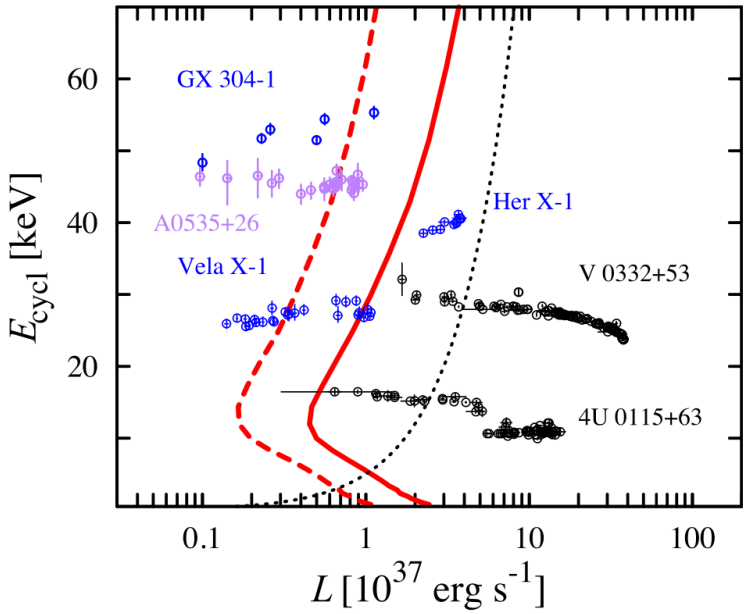


**Figure 1.7:** Cyclotron energy variations with the accretion luminosity observed in a set of variable XRPs (Mushtukov et al., 2015).

where $n$ is the number of Landau levels, $B_{12}$ is the magnetic field strength in units of $10^{12}$ Gauss, and $z$ is the gravitational redshift of the line formation region (Staubert et al., 2019). Among different models, its origin is attributed to a variation in the condition of the accretion structure (Becker et al., 2012), or to the Doppler effect in the accretion channel (Mushtukov et al., 2015). According to the theoretical framework proposed by Becker et al. (2012), the height of the accretion column can reach several kilometers, allowing high-energy photons produced near the shock region through bulk Comptonization to escape more efficiently and be observed directly, rather than being obscured or reflected by the neutron star surface. This geometry may facilitate the detection of higher harmonic lines during the supercritical accretion regime.

Observations have shown that $E_{\rm cyc}$ could vary with the accretion luminosity and time.

The correlation between the $E_{\rm cyc}$ and luminosity has long been a key focus in the study of accreting X-ray pulsars, as it provides direct insight into the strength and configuration of the local magnetic field. Previous observations suggest that cyclotron lines exhibit two distinct evolutionary trends depending on luminosity. A positive dependence of $E_{\rm cyc}$ on $L_{\rm X}$ was observed in low to moderate luminosity sources, such as in Her X-1 (Staubert et al., 2007, 2014, 2016, 2017, 2020), in Vela X-1 (Fürst et al., 2014; La Parola et al., 2016; Diez et al., 2022), in Cep X-4 (Vybornov et al., 2017). A negative dependence of $E_{\rm cyc}$ on $L_{\rm X}$ was observed in relatively high luminosity sources, such as in V 0332+53 (Tsygankov et al., 2006; Cusumano et al., 2016; Doroshenko et al., 2017; Vybornov et al.,

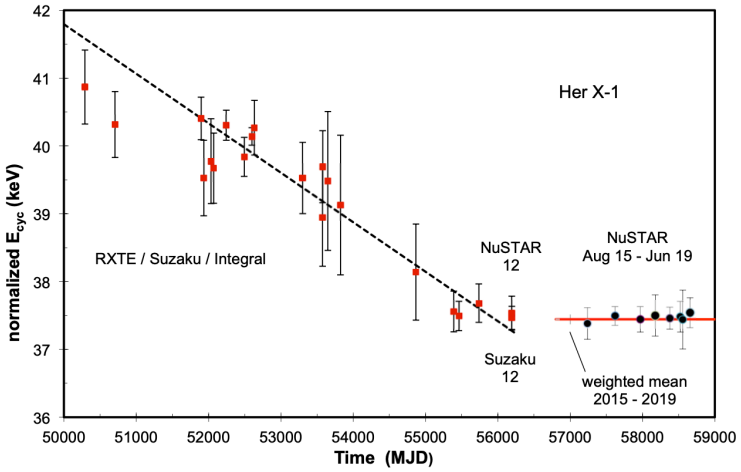


**Figure 1.8:** Evolution of the cyclotron line energy in Her X-1 (Staubert et al., 2020).

2018) and in 1A 0535+262 (Kong et al., 2021). In the cases of V 0332+53 (Vybornov et al., 2017) and A 0535+26 (Kong et al., 2021), both positive and negative correlations between $E_{\rm cyc}$ and luminosity have been observed, with the critical luminosity marking the transition between these regimes robustly determined. It has also been demonstrated that the same source can exhibit different values of $E_{\rm cyc}$ at the same luminosity (Cusumano et al., 2016; Kong et al., 2021). Figure 1.7 shows the variation of the cyclotron line energy with accretion luminosity observed in a sample of variable XRPs.

So far, only two sources, Her X-1 and Vela X-1, have shown clear long-term variability in $E_{\rm cyc}$ over timescales of tens of years (Staubert et al., 2020; La Parola et al., 2016; Ji et al., 2019). In Her X-1, the long-term decay of $E_{\rm cyc}$ ended around 2012, stabilizing at approximately 37 keV, with a decline rate of $\sim$0.26 keV yr$^{-1}$ between 1996 and 2012 (Staubert et al., 2020) (see Figure 1.8).

The long-term behavior of $E_{\rm cyc}$ in Vela X-1 is discussed in detail in Section 3.2.4.

## 1.3 X-ray Observatories

In this chapter, the observatories whose data have been used in the present work will be discussed: *Insight*-HXMT, *NuSTAR* and *Swift*/BAT. The descriptions are primarily based on Zhang et al. (2020) for *Insight*-HXMT, Harrison et al. (2013) for *NuSTAR*, and Barthelmy et al. (2005) for *Swift*/BAT. In our study, *Insight*-HXMT data has been used for the analysis of EXO 2030+375, while data from *NuSTAR* and *Swift*/BAT have been used for the analysis of Vela X-1.

### 1.3.1 Hard X-ray Modulation Telescope (*Insight*-HXMT)

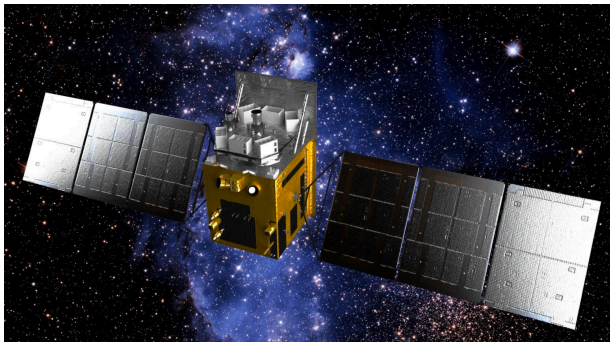

**Figure 1.9:** An artist's illustration of *Insight*-HXMT. Figure from Zhang et al. (2020).

#### Technical Description

The Hard X-ray Modulation Telescope (Insight-HXMT, also known as HXMT; Zhang et al. 2020), launched on 15th June 2017, is the first Chinese X-ray astronomical satellite. Figure 1.9 gives an artist's view of the satellite in space. The telescope has a large effective area in hard X-rays, and covers a broad energy band 1–250 keV. The three slat-collimated instruments onboard are the low-energy X-ray telescope (LE), the medium-energy X-ray telescope (ME), and the high-energy X-ray telescope (HE), as shown in Figure 1.10. HE uses 18 NaI/CsI detectors, covering the energy range of 20–250 keV for pointing and scanning observations, and 0.2–3 MeV for all-sky gamma-ray monitoring. It has a total geometrical area of approximately 5100 $cm^2$. ME uses 1728 Si-PIN detectors, operating in the 5–30 keV energy range with a total geometrical area of 952 $cm^2$. LE telescope uses swept charge devices (SCDs) as detectors, sensitive to 1–15 keV X-rays, with a total geometrical area of 384 $cm^2$. The instrument parameters of the LE, ME, and HE are listed in Table 1.2.

HXMT operates in three observational modes: pointing, scanning, and Gamma-Ray Burst (GRB). Pointing observations last from one orbit (96 minutes) to 20 days and are

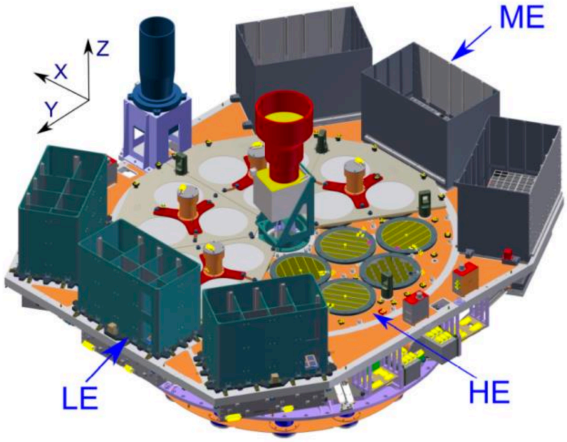


**Figure 1.10:** FOVs and their orientations for all telescopes. Figure from Zhang et al. (2020).

| | **LE** | **ME** | **HE** |
|---|---|---|---|
| Detectors | SCD | Si-PIN | NaI/CsI |
| Geometrical area | 384 $cm^2$ | 952 $cm^2$ | 5000 $cm^2$ |
| Energy range (keV) | 1–15 | 5–30 | 20–250 |
| Time resolution | 1 ms | 180 $\mu$s | 25 $\mu$s |
| Energy resolution | 2.5% at 6 keV | 14% at 20 keV | 19% at 60 keV |
| Data handling capability | $\leq$ 3 Mbp/s | $\leq$ 3 Mbp/s | $\leq$ 300 kbp/s |

**Table 1.2:** Instrument parameters of the LE, ME, and HE detectors onboard *Insight*-HXMT.

used for spectral and timing studies. The Galactic plane can be mapped with the scan mode, which divides it into 22 patches of $20° \times 20°$, each scanned over 2 hours to 5 days depending on parameters. In GRB mode, the PMT voltage is lowered to extend the CsI energy range to 0.2–3 MeV, enabling HE to serve as an all-sky gamma-ray monitor with a large effective area ($> 1000$ $cm^2$) and microsecond time resolution. HXMT is a non-imaging telescope, the background is generated using a background model constructed through training and calibration on multiple calibration sources of the blind detectors (Chen et al. 2020; Cao et al. 2020; Liu et al. 2020).

### Science Goals

HXMT enables high-cadence surveys of the Galactic plane and is expected to build a catalog of sources exhibiting short-timescale variability in hard X-rays. Its large effective area supports detailed studies of XRBs in the low/hard state. HXMT can provide broadband observations with good statistics for both persistent and transient sources. The core sciences of HXMT are: (1) to scan HXMT enables high-cadence surveys of the Galactic plane and is expected to build a catalog of sources exhibiting short-timescale variability

in hard X-rays. Its large effective area supports detailed studies of XRBs in the low/hard state. HXMT also provides broadband observations with good statistics for both persistent and outbursting sources. the Galactic plane and find new transient sources and to monitor the known variable sources; (2) to observe X-ray binaries in broad energy band and study the dynamics and emission mechanism in strong gravitational or magnetic fields; (3) to observe GRBs in a relatively rarely explored band from a few hundred keV to a few MeV.

### 1.3.2 Nuclear Spectroscopic Telescope Array (*NuSTAR*)

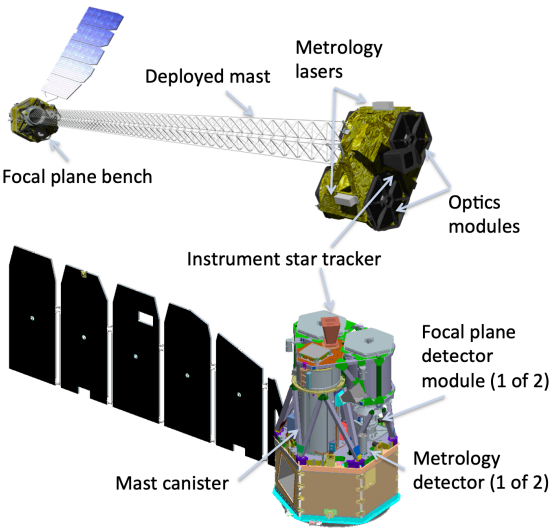


**Figure 1.11:** Diagram of the *NuSTAR* observatory in the stowed (bottom) and deployed (top) configurations. Figure from Harrison et al. (2013).

#### Technical Description

The Nuclear Spectroscopic Telescope Array (*NuSTAR*), launched on 13 June 2012, is the first focusing hard X-ray observatory(Harrison et al., 2013). *NuSTAR* is equipped with two detector units, each positioned at the focus of the two co-aligned X-ray optics. Each detector unit, also referred to as a focal plane module, comprises four Cadmium-Zinc-Telluride (CdZnTe or CZT) detectors developed by eV Products. Each CZT crystal measures 20 mm $\times$ 20 mm with a thickness of 2 mm, and is divided into a 32 $\times$ 32 pixel grid. CZT detectors are advanced room-temperature semiconductors, highly efficient at converting incident high-energy photons into charge carriers. The resulting electrons are digitized via custom Application Specific Integrated Circuits (ASICs), which were developed by the *NuSTAR* Focal Plane Team at Caltech. To suppress background events, the focal planes are actively shielded by Cesium-Iodide (CsI) scintillator crystals surrounding

| Parameter | Value |
|---|---|
| Energy range | 3–78.4 keV |
| Angular resolution (HPD) | $58''$ |
| Angular resolution (FWHM) | $18''$ |
| FoV (50% resp.) at 10 keV | $10'$ |
| FoV (50% resp.) at 68 keV | $6'$ |
| Sensitivity (6–10 keV) [$10^6$ s, $3\sigma$, $\Delta$E/E = 0.5] | $2 \times 10^{-15}$ erg cm$^{-2}$ s$^{-1}$ |
| Sensitivity (10–30 keV) [$10^6$ s, $3\sigma$, $\Delta$E/E = 0.5] | $1 \times 10^{-14}$ erg cm$^{-2}$ s$^{-1}$ |
| Background in HPD (10–30 keV) | $1.1 \times 10^{-3}$ cts s$^{-1}$ |
| Background in HPD (30–60 keV) | $8.4 \times 10^{-4}$ cts s$^{-1}$ |
| Spectral resolution (FWHM) | 400 eV at 10 keV, 900 eV at 68 keV |
| Strong source ($>10\sigma$) positioning | $1.5''$ ($1\sigma$) |
| Temporal resolution | 2 $\mu$s |
| Target of opportunity response | $<$24 hr |
| Slew rate | $0.06^\circ$ s$^{-1}$ |
| Settling time | 200 s (typ) |

**Table 1.3:** *NuSTAR* instrument parameters.

the detector housing. These CsI shields, manufactured by Saint-Gobain, detect cosmic rays and high-energy photons arriving from directions outside the *NuSTAR* optical axis—sources that dominate the instrumental background. The shielding system ensures that any event in the CZT detectors occurring simultaneously with a CsI signal is identified as background and rejected, thereby enhancing the sensitivity to genuine cosmic sources.

The angular resolution of *NuSTAR* is primarily determined by its focusing optics, yielding a full width at half maximum (FWHM) of $18''$ and a half power diameter (HPD) of $58''$. The focal plane is optimized for excellent energy resolution in the hard X-ray band, achieving a FWHM of 400 eV at 10 keV and 0.9 keV at 60 keV. To further reduce instrumental background above 10 keV, an active anti-coincidence shield is implemented around the focal plane. Table 1.3 summarizes the key performance parameters.

### Science Goals

*NuSTAR* focused on several key science goals: surveying the sky for obscured AGNs up to redshift $\sim$2; mapping the Galactic Center to study compact hard X-ray sources; investigating non-thermal emission and radioactive decay lines in young supernova remnants; conducting multiwavelength observations of blazars to probe AGN jet structures; and observing nearby supernovae to constrain explosion models.

### 1.3.3 Swift's Burst Alert Telescope (BAT)

#### Technical Description

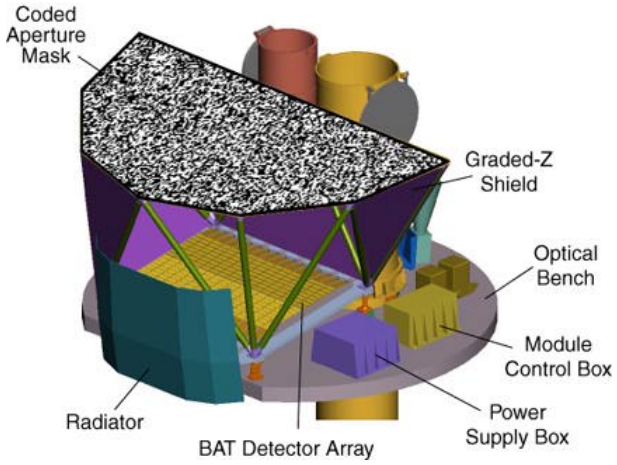


**Figure 1.12:** A cut-away drawing of the BAT. Figure from https://swift.gsfc.nasa.gov/about_swift/bat_desc.html.

The Burst Alert Telescope (BAT; Barthelmy et al. 2005) is a hard X-ray detector onboard the Neil Gehrels *Swift* observatory (Gehrels et al., 2004). The BAT is a highly sensitive, large FOV (1.4 sr half-coded & 2.3 sr partially-coded), coded-aperture telescope designed to monitor a large fraction of the sky for the occurrences of GRBs. The BAT provides the burst trigger and the 1–4 arcmin accurate position, that is then used to slew the spacecraft to point the two narrow-FOV instruments (the X-ray telescope – XRT, and the ultraviolet and optical telescope – UVOT) for follow-up observations. While observing bursts, BAT simultaneously and automatically accumulates an all-sky hard X-ray survey. The basic numbers describing the BAT instrument are listed in Table 1.4.

The BAT instrument comprises a detector plane with 32,768 CZT elements and associated front-end electronics, a coded aperture mask positioned 1 m above the detector, and a graded-Z fringe shield designed to reduce instrumental and cosmic diffuse background. A thermal radiator and control system maintain the detector at a stable temperature. The instrument is managed by the onboard Image Processor, which also performs real-time event processing, including burst detection, localization, and figure-of-merit evaluation. In parallel with burst searches, BAT continuously conducts a hard X-ray survey of the entire sky throughout the mission.

BAT operates in two modes: burst mode, which provides burst localization, and survey mode, which generates hard X-ray survey data. In survey mode, the instrument collects count-rate data in five-minute time bins across 80 energy channels. Upon detecting a burst,

| Parameter | Value |
|---|---|
| Energy range | 15–150 keV |
| Energy resolution | $\sim$7 keV |
| Aperture | Coded mask, random pattern, 50% open |
| Detecting area | 5240 $cm^2$ |
| Detector material | CdZnTe (CZT) |
| Detector operation | Photon counting |
| Field of view | 1.4 sr (half-coded) |
| Detector elements | 256 Modules of 128 elements/module |
| Detector element size | $4.00 \times 4.00 \times 2.00$ $mm^3$ |
| Coded mask cell size | $5.00 \times 5.00 \times 1.00$ $mm^3$ Pb tiles |
| Instrument dimensions | 2.4 m $\times$ 1.2 m $\times$ 1.2 m |
| Telescope PSF | 17 arcmin |
| Source position accuracy | 1–4 arcmin |
| Sensitivity | $\sim 10^{-8}$ erg $s^{-1}$ $cm^{-2}$ |
| Number of bursts detected | $>$100 $year^{-1}$ |

**Table 1.4:** *Swift*-BAT instrument parameters.

BAT switches to a photon-by-photon mode, utilizing a ring buffer to preserve pre-burst information. In our study of Vela X-1, we utilized BAT data acquired in survey mode.

### Science Goals

A major scientific goal of the *Swift* mission is to uncover the nature and origin of GRBs – including their progenitors, classifications, and environments – and to use them as probes of the early universe. Its autonomous slewing capability enables repositioning within 20 – 70 seconds of a burst trigger, allowing X-ray and UV/optical telescopes to observe the afterglow in near real-time, sometimes even while the burst is still active. The *Swift* compliment of instruments also provides a powerful observatory for the follow-up of other hard X-ray transients detected by BAT.

# 2

# DATA AND METHODS

## 2.1 Data

### 2.1.1 *Insight*-HXMT

*Insight*-HXMT data can be downloaded from hxmt website,[1] where you can find additional information about the software, CALDB, and data. The structure of the data and the sequence of processing tasks are summarized in the "HXMT Data Reduction Guide".[2]

The data were processed using the standard procedures provided by the HXMT Data Analysis Software (HXMTDAS).[3] HXMTDAS is designed to produce scientific data products from *Insight*-HXMT observations, including energy spectra, light curves, ancillary response files (ARFs), redistribution matrix files (RMFs), and background files. The processing workflow within HXMTDAS consists of three main stages:

- **Calibration**: the Pulse Invariant (PI) values are computed from the raw Pulse Height Amplitude (PHA), accounting for temporal variations in gain and energy offset. There is a simple correlation between PI and energy $E$ (in keV) for each detector:
  - HE: $\mathrm{PI} = 256 \times (E - 15)/370$
  - ME: $\mathrm{PI} = 1024 \times (E - 3)/60$
  - LE: $\mathrm{PI} = 1536 \times (E - 0.1)/13$
- **Screening**: a FITS good time interval (GTI) file is generated and used, together with other criteria, to filter the data;
- **Extraction of high-level scientific products**: energy spectra, response files (RSP), light curves, and background files are produced from the screened event files.

The data-reduction pipeline was developed by Prof. Ji Long's team. It is available at https://code.ihep.ac.cn/jldirac/insight-hxmt-code-collection, with regular updates to meet the requirements of the collaboration.

[1] http://hxmten.ihep.ac.cn/

[2] https://integral.esac.esa.int/bexrbmonitor/Plots/sim_plot_EXO2030+375.html

[3] http://hxmtweb.ihep.ac.cn/software.jhtml

### 2.1.2 *NuSTAR*

*NuSTAR* data can be downloaded from the NuSTAR archive at HEASARC.[4] The data are automatically processed at the Science Operations Center (SOC) at Caltech using the NuSTAR Data Analysis Software (NuSTARDAS), which is integrated in HEASoft[5]. In addition, users should have some experience using the SAOImage DS9 astronomical imaging and data visualization application that can display FITS format images.

The data processing using NuSTARDAS is organized into three stages:

- **Calibration**: the raw detector signals are processed with `nupipeline`, which applies metrology and attitude corrections, screens bad and hot pixels, and performs energy calibration;
- **Screening**: event-selection criteria such as energy range, event grade, and time intervals are applied using `nupipeline` to filter the data and retain only high-quality events;
- **Product extraction**: after defining the source and background regions in DS9, scientific products, including light curves, spectra, and response files (RMF and ARF), are generated using `nuproducts`.

*NuSTAR* consists of two telescopes with separate focal plane modules (FPMA and FPMB). The data from each module are processed independently, and combined only in the final stage during joint spectral fitting. The detailed usage instructions for the data analysis is available at `https://heasarc.gsfc.nasa.gov/docs/nustar/analysis`.

### 2.1.3 *Swift*/BAT

The BAT survey data are publicly available at `https://heasarc.gsfc.nasa.gov/FTP/swift/data/` . The Swift software is distributed as part of HEASoft, and the pipeline processing is performed at the Swift Data Center (SDC) at NASA/GSFC. Most processing steps are already carried out by the SDC. [6] These individual scripts allow users to perform the data analysis "by hand". A detailed description of the procedure can be found in the BAT software guide.[7] Here, I briefly summarize the main steps:

- **Rebinning and filtering**: survey data are provided as detector plane histograms (DPHs) integrated over at least 300 s. The `batsurvey-erebin` task places all

[4] `https://heasarc.gsfc.nasa.gov/cgi-bin/W3Browse/w3browse.pl`
[5] `https://heasarc.gsfc.nasa.gov/docs/software/lheasoft/`
[6] `https://www.swift.ac.uk/analysis/bat/`
[7] `https://swift.gsfc.nasa.gov/analysis/bat_swguide_v6_3.pdf`

detectors on a common energy scale and rebins the DPHs into user-defined energy intervals. Data are then filtered to retain only GTIs and detectors producing valid data.

- **DPI creation and cleaning**: after temporal and spatial filtering, the DPHs are converted into detector plane images (DPIs).
- **Sky image construction**: the `batfftimage` task is then used to convert the cleaned DPIs into sky images.
- **Spectrum extraction**: for spectral extraction, the source count rates in each energy bin are taken from the `batsurvey` catalog and stored in a pulse height amplitude (PHA) file. A detector response matrix (DRM) is generated for each snapshot using `batdrmgen`. The PHA file and DRM can then be loaded into `Xspec` for spectral fitting.

Once the workflow and the individual tasks are familiar, users can create their own scripts to automate the analysis. A comprehensive Python pipeline for Swift/BAT survey analysis is provided by Parsotan et al. (2023).

## 2.2 Methods

### 2.2.1 Spectral analysis

After completing the data-reduction pipelines and obtaining the scientific products (event files, spectra, and response files), we now describe how these products are used to construct the energy spectrum of the source.

The spectrum characterizes the energy distribution of photons emitted by the source. However, X-ray detectors record only the number of counts in instrumental channels rather than the intrinsic photon flux. Therefore, the spectrum extracted from the data (the PHA file) contains only the observed count distribution as a function of channel, and must be interpreted together with the corresponding response files RMF and the ARF. The RMF specifies the probability that a photon of true energy $E$ will be detected in channel $I$, while the ARF provides the effective area as a function of energy. Combined with the background contribution $B(I)$, the relation between the intrinsic photon spectrum $S(E)$ and the observed count spectrum $C(I)$ is:

$$C(I) = \int S(E)\, R(I, E)\, A(E)\, dE + B(I), \tag{2.1}$$

where $R(I, E)$ and $A(E)$ are taken from the RMF and ARF, respectively.

To recover the intrinsic photon spectrum $S(E)$, a spectral model must be included. In practice, phenomenological models such as `cutoffpl`, `comptt`, or a blackbody component are commonly adopted (the models used in this work are listed in Table 1.1 in Section 1.2.4). The model spectrum is folded through the response to predict the expected spectrum. In `Xspec`, this folded spectrum is compared with the observed counts by minimizing the fit statistic (e.g., $\chi^2$). Parameter uncertainties are estimated using the Markov Chain Monte Carlo (MCMC) method implemented in `Xspec`. We generate long chains (typically $10^5$–$10^6$ steps) and discard an initial burn–in interval to ensure convergence.

### 2.2.2 Timing analysis

After the calibrated and screened event files are obtained, the light curve can be constructed from the sequence of photon arrival times. Each detected photon carries an accurate timestamp, forming an event list. By binning these events into consecutive time intervals with a chosen temporal resolution and counting the number of photons in each bin, we obtain the count rate as a function of time, i.e., the light curve. Background photons are estimated from an independent background region or a background model and subtracted from the source light curve to produce a net light curve. The timing analysis is based on the light curves extracted from each observation.

To determine the pulse period of the NS, we search for periodic modulation in the light curve by maximizing the coherence of the signal. In practice, a trial period is applied to the time series and the data are folded using this period. If the trial period is close to the true spin period, photons from different cycles align in phase and form a stable pulse profile, while an incorrect period leads to phase mixing and the disappearance of the pulsed signal. The optimal period is therefore obtained by maximizing a statistical measure of periodicity (e.g., $\chi^2$ maximization, epoch folding, or Fourier-based techniques). These methods are implemented in the Python timing analysis package `Stingray`, which provides tools for Fourier analysis, epoch folding, and standard period searches. Then for each observation, the photon arrival times were folded with the measured spin frequency, and the counts were binned into a chosen number of phase intervals to obtain the pulse profile. By studying the pulse profiles as a function of energy and luminosity, we are able to probe how the emission geometry evolves under different accretion conditions.

# 3

# SUMMARY OF THE PUBLICATIONS

## 3.1 Timing and spectral studies of the Be/X-ray binary EXO 2030+375 using *Insight*-HXMT observations (Du et al., 2025)

### 3.1.1 Background and Motivation

EXO 2030+375 is a transient BeXRB discovered by the *EXOSAT* observatory during a type-II outburst in 1985. It hosts a $\sim 42$ s pulsar orbiting around the companion star in a rather eccentric orbit ($P_{\rm orb} \approx 46$ d, $e \sim 0.41$; Parmar et al. 1989). Its distance has been estimated as $2.4^{+0.5}_{-0.4}$ kpc by the *Gaia* Data Release 3 (Bailer-Jones et al., 2021).

Various interesting features have been observed in the spectrum of EXO 2030+375. During a type-I outburst in 1996 observed by RXTE, Reig & Coe (1999) reported a possible detection of a CRSF with a centroid energy of $\sim 36$ keV. In 2006, EXO 2030+375 underwent its second type-II outburst. Phase-resolved spectroscopy during the peak of this outburst revealed a potential CRSF at $\sim 63$ keV (Klochkov et al., 2008a).

Further insights into the accretion behavior of EXO 2030+375 were provided by the hardness-intensity diagram (HID) analysis of the 2006 outburst, as presented by Reig & Nespoli (2013). In their study (Fig. 3 in Reig & Nespoli 2013), the HID revealed a clear transition at a luminosity of $\sim 4 \times 10^{36}$ erg s$^{-1}$ (assuming a distance of 2.4 kpc). This behavior, observed in EXO 2030+375 and several other X-ray pulsars, was interpreted as a spectral state transition between two accretion regimes when the source reached the critical luminosity. The continuum spectrum also showed a corresponding transition (Fig. 6 in Reig & Nespoli 2013), reinforcing the idea of a regime change governed by the dominant deceleration mechanism: Coulomb interactions in the subcritical regime and radiation pressure in the supercritical regime (Becker et al., 2012).

Similar transitions have been inferred from pulse profile evolution in other Be/X-ray binaries during giant outbursts, including 2S 1417-624 (Ji et al., 2020), 1A 0535+262 (Wang et al., 2022), and Swift J0243.6+6124 (Tsygankov et al., 2018). These studies suggest that changes in pulse profile shape can serve as an evidence for identifying the critical luminosity.

The aim of this work is to perform a comprehensive timing and spectral analysis of EXO 2030+375 using *Insight*-HXMT observations during its 2021 giant outburst. We seek to investigate whether the source exhibited a transition in pulse profile morphology

or spectral properties as a function of luminosity, which would provide evidence for determining the critical luminosity and improve our understanding of the accretion geometry. Additionally, we aim to search for the presence of CRSFs.

### 3.1.2 Method

In this work, we present a spectral and timing analysis of EXO 2030+375, based on 1–150 keV data obtained by the *Insight*-HXMT during the 2021 giant outburst. A total of 80 observations were used, corresponding to a cumulative exposure time of approximately 2460 ks.

For the timing analysis, we used data in the 1–150 keV energy range. The spin period was measured by applying epoch folding (Leahy, 1987) to the extracted light curves. Pulse profiles were generated from light curves with a bin size of 0.5s in three energy bands: LE (1–10keV), ME (10–30keV), and HE (25–100 keV). The profiles were aligned by defining phase zero at the minimum of the pulse profile. We investigated the temporal evolution of the pulse profiles throughout the 2021 outburst, as well as energy-resolved pulse profiles at the outburst peak.

For the spectral analysis, the energy range was restricted to 2–50 keV due to the increasing background above 50 keV. We first constructed a HID to investigate how the spectral hardness, defined as the count rate ratio between 7–10 keV and 4–7 keV, varies with the total intensity, in order to explore possible spectral state transitions during the outburst. We then determined the best-fitting model for the averaged spectrum, and applied this model to the full dataset to obtain flux-resolved spectral parameters. Finally, phase-resolved spectral analyses were carried out during the rising, peak, and decay phases of the outburst to investigate the variation of spectral parameters with pulse phase and luminosity.

### 3.1.3 Results

#### Timing analysis

Figure 3.1 shows the temporal evolution of the pulse profiles of EXO 2030+375. A two-peak structure at lower flux can be clearly identified for the 1–10 keV and 10–30 keV energy bands. The pulse profiles exhibit a luminosity-dependent evolution: the secondary peak at phase 0.35 dominates at lower luminosities, while the main peak at phase 0.60 becomes more prominent at higher luminosities. This trend is more pronounced in the LE and ME energy bands, whereas the HE band consistently shows a dominant main peak.

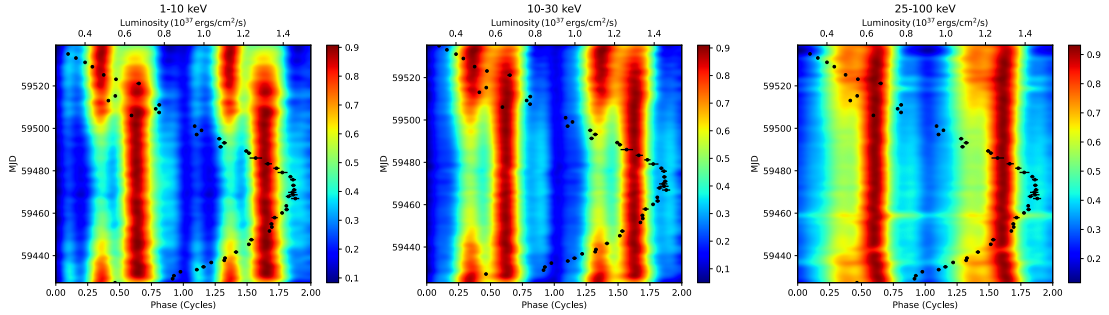


**Figure 3.1:** 2D maps showing the evolution of the pulse profile with time observed by *Insight*-HXMT during the 2021 outburst. From top to bottom: 1–10 keV, 10–30 keV, and 25–100 keV. The black points in each panel represent the luminosity (0.01–150 keV).

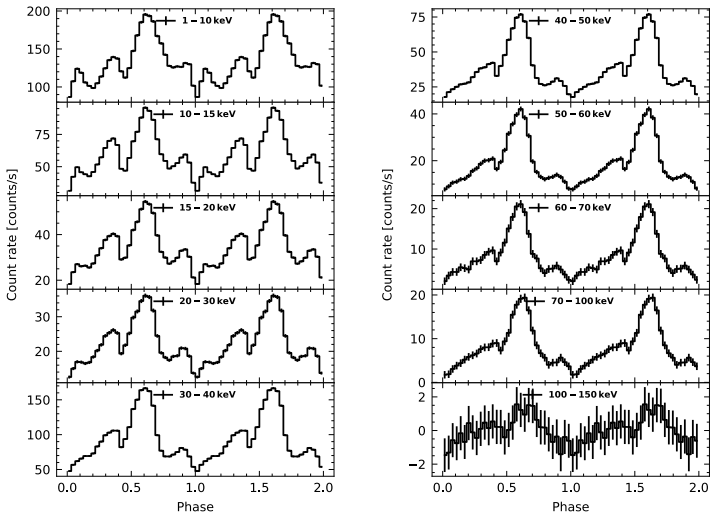


**Figure 3.2:** Energy-resolved pulse profiles of EXO 2030+375 near the maximum of the outburst.

Figure 3.2 highlights the strong energy dependence of the pulse profile near the outburst peak. The initial four-peak structure gradually simplifies into a single dominant peak at phase 0.60 as energy increases. Minor peaks at phases 0.1 and 0.9 fade above 30 keV. The secondary peak at 0.35 disappears above 70 keV. Pulsations remain detectable up to 150 keV.

## Spectral analysis

Figure 3.3 shows the 4–7 and 7–10keV light curves and the corresponding hardness ratio, color-coded to illustrate its time evolution. The HID is shown in Fig.3.4.

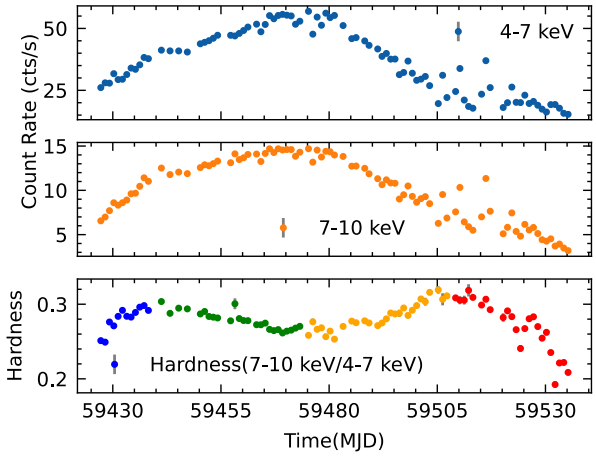


**Figure 3.3:** Net light curves and hardness of EXO 2030+375 of all observations from MJD 59427 to MID 59535. The hardness is defined as the ratio 7–10 keV / 4–7 keV. Each point corresponds to the data of one day. The evolution of hardness over time is represented by dividing it into four distinct periods, each indicated by a different color: blue (MJD 59427 to 59438), green (MJD 59438 to 59473), orange (MJD 59473 to 59508), and red (MJD 59508 to 59535).

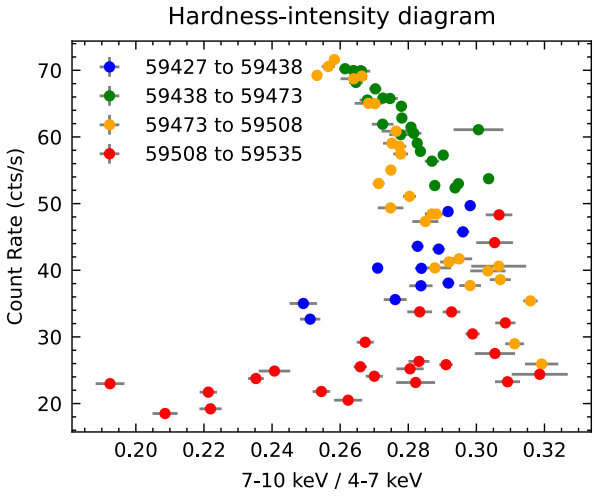


**Figure 3.4:** HID extracted from Insight-HXMT/LE data. Hardness is defined as the ratio 7–10 keV / 4–7 keV. The colors are described in the same way as in Figure 3.3.

Spectral analysis used the 2–10, 10–30, and 28–50 keV bands for LE, ME, and HE, respectively. The continuum model includes an absorbed cutoff power-law and a blackbody component to model the soft excess below $\sim$ 5 keV (Klochkov et al., 2007). A cross-calibration constant was applied across instruments, and `tbabs` with `wilm` abundances modeled absorption. A Gaussian at $\sim$6.6 keV accounts for Fe emission, while another at $\sim$5.7 keV corrects LE detector discrepancies. The 21–23 keV data were excluded due to the presence of a silver instrumental feature (Li et al., 2020). Figure 3.5 shows the broad

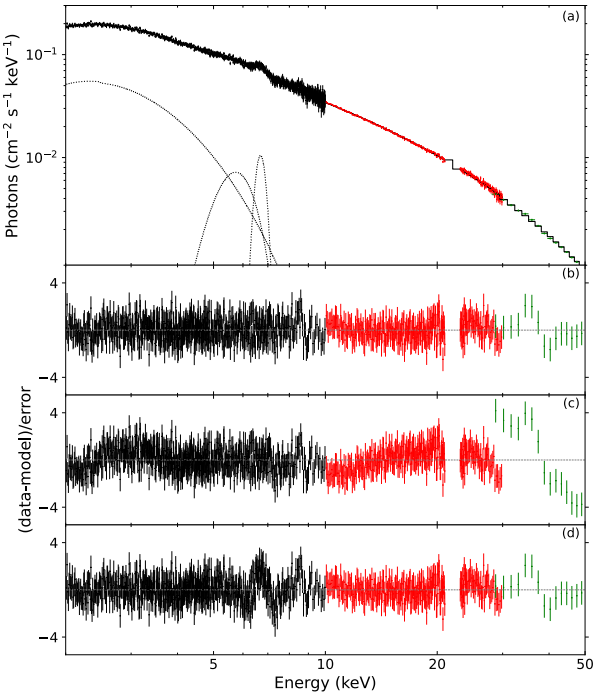


**Figure 3.5:** Broadband spectrum of EXO 2030+375 at the peak of the 2021 giant outburst in energy range 2–50 keV using the model `const×tbabs(gauss+bbodyrad+gauss+cutoffpl)`. (a) unfolded spectrum; (b) residuals for the best-fit model; (c) residuals after fitting without the blackbody component; and (d) residuals after fitting without the feature around 5.7 keV.

band spectrum at the peak of the 2021 giant outburst (MJD 59460–59461). The same model was applied to all observations. Figure 3.6 presents the evolution of spectral parameters as a function of flux. No significant correlations between the spectral parameters and luminosity are observed.

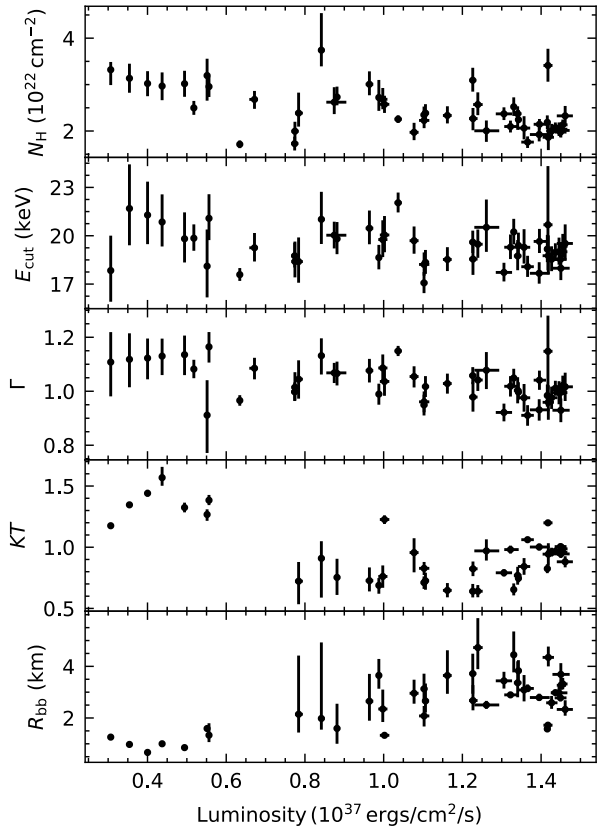


**Figure 3.6:** Flux-resolved parameters using all the observations of the 2021 giant outburst in energy range 2–50 keV.

To explore pulse-phase and luminosity-dependent spectral variability, we performed phase-resolved analysis during the rise (MJD 59436–59438), peak (59460–59461), and decay (59529–59533) of the outburst. Eleven phase bins were selected per interval. While initial fits extended to 100 keV to search for CRSFs, no significant features were found, so we limited the range to 2–50 keV for consistency. Each spectrum was fitted using the same continuum model as in the phase-averaged analysis. Figure 3.7 shows the evolution of spectral parameters with pulse phase. The LE (1–10 keV) pulse profiles used here highlight changes in peak morphology with flux. Both the photon index and cutoff energy peak near the main pulse.

### 3.1.4 Discussion

#### HID

Reig & Nespoli (2013) presented the HID of the 2006 outburst of EXO 2030+375 (Fig. 3 in their study), where hardness is defined as the ratio of 7–10 keV to 4–7 keV. The diagram shows a significant transition at a luminosity of $\sim 4 \times 10^{36}$ erg s$^{-1}$ (d=2.4 kpc). The study

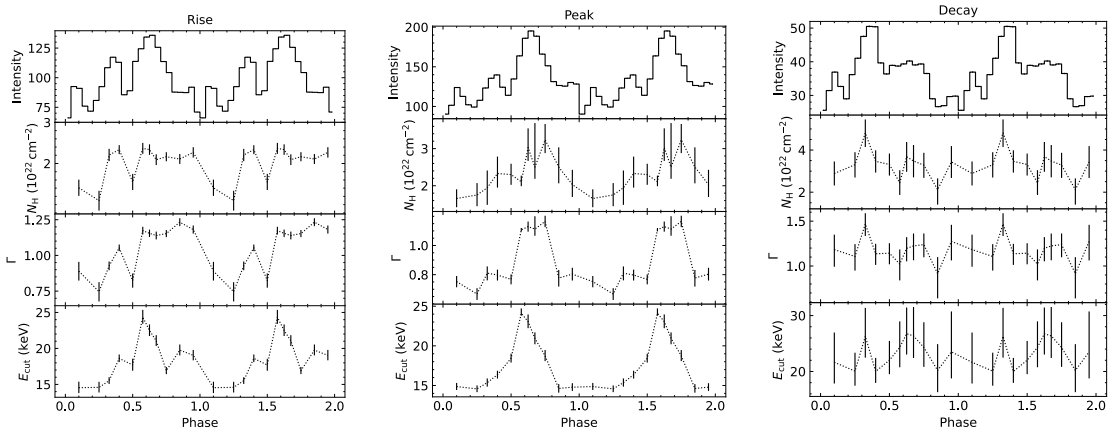


**Figure 3.7:** Modulation of phase-resolved parameters observed by *Insight*-HXMT. Rise: MJD 59436-59438, L $\sim 1.0 \times 10^{37}$ erg s$^{-1}$; peak: 59460-59461 MJD, L $\sim 1.45 \times 10^{37}$ erg s$^{-1}$; decay: 59529-59533 MJD, L $\sim 0.4 \times 10^{37}$ erg s$^{-1}$. For each of the three subfigures, the panels (from top to bottom) show the pulse profile (1–10 keV), the column density ($N_{\rm H}$), the power-law photon index ($\Gamma$), and the cutoff energy ($E_{\rm cut}$).

shows that in several X-ray pulsars, including EXO 2030+375, state transitions occur in the HID during the rise and decay phases when a critical luminosity is reached. In the 2021 outburst, the HID revealed spectral transitions at $L_{\rm x} \sim 10^{37}$ erg s$^{-1}$ during both the rise and decay. These transitions likely reflect changes in accretion regimes and indicate the presence of a critical luminosity.

## Pulse profiles

The pulse profile showed luminosity-dependent evolution (Figure. 3.1): the main peak stayed constant, while the secondary varied significantly. Around $\sim 10^{37}$,erg,s$^{-1}$, both HID and pulse shape changed, suggesting the source has reached the critical luminosity. In several giant outbursts of accreting pulsars, it has been noted that the transition of the pulse shapes could serve as a hint of critical luminosities; for instance, 2S 1417-624 (Ji et al., 2020), 1A 0535+262 (Wang et al., 2022), and Swift J0243.6+6124 (Tsygankov et al., 2018). Since pulse profiles reflect the emission geometry, which depends on the accretion rate, a shift from pencil beam (sub-critical regime) to fan beam (super-critical regime) is expected (Mushtukov & Tsygankov, 2023).

If the pulse profile shape transitions are indeed due to EXO 2030+375 reaching a critical luminosity, we can infer that the geometries of the emitting region has always been a mixture of pencil beam and fan beam. The main peak is dominated by the fan beam, while the secondary peak is dominated by the pencil beam, with the pencil beam contributing more at lower luminosities compared to higher luminosities.

The energy-dependent pulse profiles near peak luminosity (Figure 3.2) exhibit complex multi-peaked structures at low energies that merge into single peaks at higher energies. These variations may arise from energy-dependent changes in the beam pattern and/or local absorption caused by the asymmetric distribution of matter in the system. The single-peaked profiles at high energies are likely due to a fan beam emission geometry (Hou et al., 2022).

#### Phase-averaged and phase-resolved spectra

In our analysis, the broadband spectrum is well described by a cutoff power law with a blackbody and a 6.6 keV iron line. Throughout the outburst, no clear $\Gamma$–luminosity correlation was seen, possibly due to narrower luminosity coverage or large uncertainties at low luminosities.

Phase-resolved analysis confirms strong spectral variations across pulse phase. In 2006, a possible CRSF at 63.6 keV was seen between main and secondary peaks (Klochkov et al., 2008a), but no such feature appears in 2021. During the 2021 outburst, the power-law photon index and cutoff energy peaked with the main pulse (Figure3.7), consistent with *Insight*-HXMT results from the outburst in 2022 (Malacaria et al., 2023). In contrast, the 2006 outburst showed a minimum in the photon index around the main peak. The peak luminosity of the 2006 outburst was $\sim 1.3 \times 10^{37}\,\mathrm{erg\,s^{-1}}$ if d=2.4 kpc, from Klochkov et al. (2008a), as observed with INTEGRAL JEM-X in the $2-9$ keV energy range. Our peak luminosity for the 2021 outburst is $\sim 1.45 \times 10^{37}\,\mathrm{erg\,s^{-1}}$, measured across the $0.01-150$ keV range. As observed by *Swift*/BAT[1], the flux of the 2006 reached 1.2 Crab, compared to 0.6 Crab in 2021, suggesting it was about twice as bright. This luminosity difference may explain the contrasting phase-resolved results between 2006 and 2021.

### 3.1.5 Summary

- **Aim:** to investigate the timing and broadband spectral evolution of EXO 2030+375 during the 2021 giant outburst, covering a wide luminosity range with *Insight*-HXMT observations.
- **Novelty and Main results:**
  - We present the complete broadband (1–150 keV) timing and spectral study of the 2021 giant outburst of EXO 2030+375 using Insight-HXMT, covering the full evolution of the event.

[1] https://integral.esac.esa.int/bexrbmonitor/Plots/sim_plot_EXO2030+375.html

– We find significant luminosity- and energy-dependent changes in the pulse profile morphology, with two transitions that coincide with the state changes in the HID, providing a constraint on the critical luminosity.
– Phase-resolved spectroscopy reveals strong pulse-phase variability but no evidence for cyclotron lines across the entire energy range.

## 3.2 Long-term evolution of cyclotron resonant scattering features in the accreting pulsar Vela X-1: A pulse-to-pulse approach (Du et al., accepted by *Astronomy & Astrophysics*)

### 3.2.1 Background and Motivation

Vela X-1 is an eclipsing high-mass X-ray binary (HMXB) and one of the earliest X-ray sources discovered in the history of X-ray astronomy (Chodil et al., 1967). It consists of the BO.5 Ib supergiant HD 77581 (Hiltner et al., 1972), and a wind-accreting neutron star (NS) with a spin period of ∼283 s, rotating in an 8.9 d orbit around the companion. The distance to the system is about 2 kpc (Kretschmar et al., 2021). The mean luminosity is 4–5 $\times$ $10^{36}$ erg $s^{-1}$ in the 20 – 60 keV energy band (Fürst et al., 2010).

The first evidence for CRSFs in Vela X-1– a fundamental line is at approximately 25 keV and a first harmonic line near 50 keV – was reported by Kendziorra et al. (1992) based on observations with the High Energy X-ray Experiment (HEXE). Significant variability has been observed with the CRSF in Vela X-1, regarding its centroid energy $E_{\rm cyc}$ and other characteritic parameters like its width and its optical depth. These parameters vary with luminosity and with time. Fürst et al. (2014) detected both CRSFs based on *NuSTAR* observations, and for the first time reported a positive correlation between the energy of the harmonic line ($E_{\rm cyc,H}$) and luminosity, consistent with theoretical predictions in the subcritical accretion regime (Becker et al., 2012). In contrast, the energy of the fundamental line ($E_{\rm cyc,F}$) exhibits a more complex, non-monotonic dependence on luminosity. This positive $E_{\rm cyc,H}$–luminosity correlation was further confirmed by La Parola et al. (2016) through an analysis of long-term *Swift*/BAT data. In addition, they discovered a secular decline in $E_{\rm cyc,H}$ at a rate of ∼0.36 keV $yr^{-1}$ between 2004 and 2010. This establishes Vela X-1 as the second known source, after Her X-1 (see the summary by Staubert et al. 2020), to exhibit a long-term $E_{\rm cyc}$ decay. Ji et al. (2019) confirmed the decrease stopped with a stable $E_{\rm cyc,H}$ thereafter based on continued *Swift*/BAT monitoring.

A key question concerns whether the long-term decay of $E_{\rm cyc,H}$ in Vela X-1 has truly ended and whether there is any indication of a subsequent increase. However, since observations were obtained at different luminosity levels, the $E_{\rm cyc}$–luminosity correlation

presents a major challenge for disentangling intrinsic long-term evolution of $E_{\rm cyc}$ from its luminosity dependence. Previous studies have addressed this issue by using normalization techniques in Her X-1 (Staubert et al., 2014), and by comparing evolutionary trends across different epochs in Vela X-1 (La Parola et al., 2016). In this work, we aim to address this issue by applying a pulse-to-pulse analysis technique.

### 3.2.2 Method

In this paper, we analyze *Swift*/BAT monitoring data of Vela X-1 spanning from January 2005 to December 2024, employing the methodology and software developed by Klochkov et al. (2015) and validated by Ji et al. (2019). We also present a detailed spectral analysis using nine *NuSTAR* observations conducted between 2012 and 2024.

The aim of the BAT spectral analysis is to investigate the evolution of the energy of the harmonic cyclotron line with time. Due to the regular monitoring of the source by BAT, the dataset is nearly uniformly sampled, with minimal time gaps. The instrument is sensitive in the energy range of 15–150 keV and is suited for the study of the ∼55 keV harmonic cyclotron line in Vela X-1. The data are publicly available via HEASARC.[2] All selected observations were taken in survey mode, where events are recorded as detector plane histograms (DPHs) accumulated over five-minute intervals. To enhance the statistics in the spectral analysis, we jointly fitted hundreds of spectra within three-month intervals, for which the spectral shapes were assumed to be the same while normalizations were variable. The validity of this method has been previously verified by Klochkov et al. (2015) and Ji et al. (2019).

The *NuSTAR* data span the 3–79 keV energy band and are sufficiently sensitive to detect both CRSFs. We aimed to investigate the energy dependence on luminosity across different time intervals to explore the long-term evolution of spectral variability. However, the available data were insufficient to establish a definitive correlation. To address this limitation, we applied a pulse-to-pulse analysis to the *NuSTAR* data, in which individual pulses are identified, assigned a pulse amplitude, and grouped into amplitude-selected bins to extract spectra. This technique, originally introduced by Klochkov et al. (2011), effectively expands the observed luminosity range and provides more detailed insights into spectral evolution. It relies on the fact that, most accreting pulsars exhibit strong pulse-to-pulse variations in amplitude, driven by short-term fluctuations in the accretion rate. By selecting individual pulses with similar amplitudes and grouping them to generate spectra, this method extends the accessible luminosity range and improves statistics. Therefore, it enables a more detailed investigation of the luminosity dependence of the

[2] https://heasarc.gsfc.nasa.gov/docs/archive.html

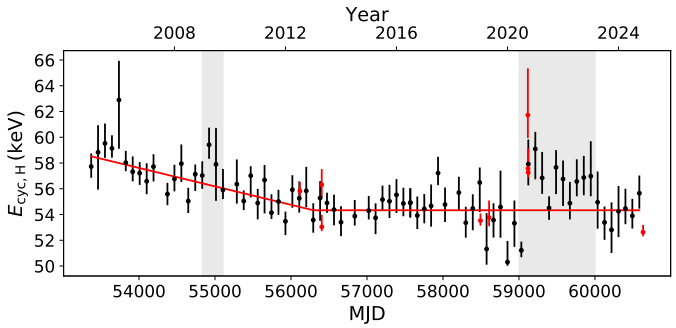


**Figure 3.8:** Long-term evolution of the centroid energy of the harmonic cyclotron line in Vela X-1 as observed with *Swift*/BAT. The gray shaded regions indicate epochs of apparent $E_{\mathrm{cyc,H}}$ humps, and red points represent time-averaged results from *NuSTAR* observations in the next section.

CRSF energy. The pulse amplitude is defined as the total number of counts summed over a single pulse. Pulses with similar amplitudes were grouped together. We explored the distribution of pulse amplitudes and divided the entire range of amplitudes into several bins, ensuring approximately equal statistics within each bin. The number of bins was primarily determined by the available counting statistics for the energy spectra, which needed to be sufficient to constrain the cyclotron line energy during spectral fitting. For each bin, a list of Good Time Intervals (GTIs) was generated to select pulses within the corresponding amplitude range. Using these GTIs, we extracted the broadband spectra for each amplitude bin.

### 3.2.3 Results

#### *Swift*/BAT result

For the BAT analysis, we adopted the `comptt` model, consistent with previous studies of BAT observations (La Parola et al., 2016; Ji et al., 2019). The fundamental cyclotron line at ∼25 keV is not detectable in BAT. The combined model, `comptt × gabs`, yields a good fit across all spectra. The temperature of the seed photons was fixed at 1 keV during the fitting. In Figure 3.8, the black data represent the *Swift*/BAT results, while the red data represent the time-averaged results from the *NuSTAR* observations discussed in the following section. Initially, the line energy exhibited a significant decrease and remained nearly constant thereafter. A pronounced fluctuation occurred between MJD 59000 and MJD 60000 (corresponding to the years 2020 to 2023), After this period, the energy returned to its pre-fluctuation level. We adopted a broken linear function to model

the evolution of $E_{\mathrm{cyc,H}}$, following the approach of Ji et al. (2019):

$$E_{\mathrm{cyc,H}}(t) = \begin{cases} E_0 + a\,(t - t_0), & t \leq t_{\mathrm{crit}}, \\ E_0 + a\,(t_{\mathrm{crit}} - t_0), & t > t_{\mathrm{crit}}. \end{cases}$$

Here, $E_0$ is the reference energy at fixed epoch $t_0$=53371 (MJD), $a$ is the linear slope describing the decreasing trend, and $t_0$ is the break time after which the $E_{\mathrm{cyc,H}}$ remains constant. The resulting $t_{\mathrm{crit}}$ is MJD $56293 \pm 264$. The decrease rate of $E_{\mathrm{cyc,H}}$ is $-0.584 \pm 0.073$ keV yr$^{-1}$. After the break, the $E_{\mathrm{cyc,H}}$ remains constant at $54.60 \pm 0.83$ keV. Over the evolution, two abrupt humps are apparent, occurring around MJD 55000, and between MJD 59000 and MJD 60000.

### *NuSTAR* result

For the nine *NuSTAR* observations, the Fermi–Dirac cut-off model (`FDcut`) provides a good fit to the continuum and has also been adopted in previous studies (Fürst et al., 2014; La Parola et al., 2016; Diez et al., 2022). The two CRSFs were modeled with `gabs` components. Following Fürst et al. (2014) and Diez et al. (2022), we fixed $\sigma_{\mathrm{cyc,F}} = 0.5 \times \sigma_{\mathrm{cyc,H}}$, motivated by the Landau-level interpretation (see equation 1.6). The continuum was modeled with `tbabs` (with `wilm` abundances) and a partial covering absorber (`pcfabs`) to account for the stellar wind. A Gaussian at $\sim 6.4$ keV models Fe fluorescence, and a broad feature at $\sim 10$ keV was required for an adequate fit, as reported for Vela X-1 and other sources. A cross-normalization constant was applied for joint fitting, and unabsorbed fluxes were obtained with `cflux`. This model was subsequently applied to fit the average spectra of nine *NuSTAR* observations. Figure 3.9 shows the best-fit spectral parameters. The luminosity range derived from the time-averaged spectral analysis is approximately $(0.2\text{–}0.8) \times 10^{37}$ erg s$^{-1}$. No clear trend is observed in the evolution of $E_{\mathrm{cyc,F}}$ with luminosity. Similarly, no obvious correlation between $E_{\mathrm{cyc,H}}$ and luminosity can be established based on the nine averaged measurements. Notably, the $E_{\mathrm{cyc,H}}$ in the three 2020 observations are significantly higher than those at similar luminosity levels, consistent with the *Swift*/BAT result showing an increase in the line energy from 2020.

Using the pulse-to-pulse method, we divided each observation into several amplitude bins and extracted spectra accordingly for the pulse-count distributions. For data sets with insufficient exposure, only time-averaged spectra were retained. Distributions of counts per individual pulse is shown in Figure 3.10. We employed the same model as used in the time-averaged analysis. Given the shorter exposure time per pulse-to-pulse spectrum, we had to fix some parameters to their respective time-averaged values to achieve a good fit, including $\sigma_{\mathrm{K}\alpha}$, $E_{10,\mathrm{keV}}$, $\sigma_{10,\mathrm{keV}}$, $\sigma_{\mathrm{cyc,F}}$, and $\sigma_{\mathrm{cyc,H}}$. The continuum cutoff energy $E_{\mathrm{cut}}$ was

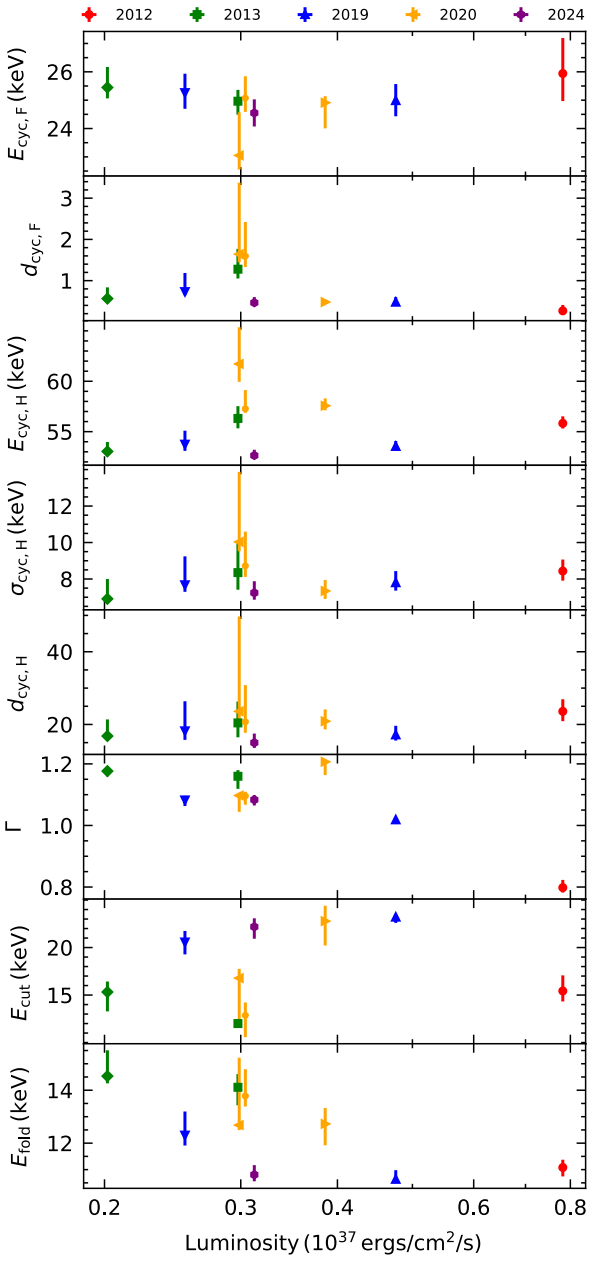


**Figure 3.9:** Flux-resolved spectral parameters derived from nine *NuSTAR* observations in the 3–70 keV energy range, shown as a function of intrinsic source luminosity. From top to bottom: energy of the fundamental line, energy of the harmonic line, width of the harmonic line, strength of the harmonic line, photon index, cutoff energy, and folding energy.

also fixed because of its degeneracy with $E_{\mathrm{cyc,F}}$. With this strategy, all spectra were well fitted.

Figure 3.11 presents the spectral results obtained from the pulse-to-pulse analysis. Different colors indicate different observation years, while variations in marker style within the same color represent different observation IDs. The fundamental line energy, $E_{\mathrm{cyc,F}}$,

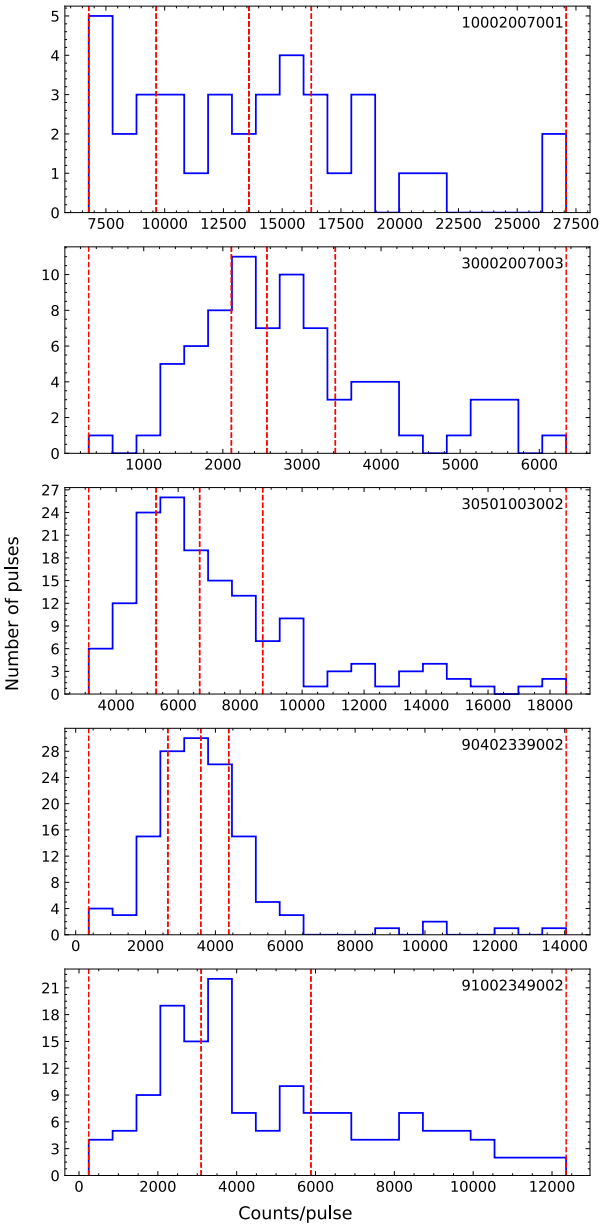


**Figure 3.10:** Distributions of counts per individual pulse (i.e. of pulse amplitudes). The red dashed lines indicate the boundaries of the amplitude bins used for extracting pulse-to-pulse spectra. In each distribution, the total number of counts is evenly distributed among the bins.

exhibits no significant variation with time or luminosity, remaining stable at approximately 25 keV. For the energy of harmonic line, $E_{\mathrm{cyc,H}}$, excluding the 2020 observations, the data appear fairly stable, with slightly lower values at lower luminosities. Moreover, at comparable luminosity levels, there is no time dependence of the $E_{\mathrm{cyc,H}}$ across different epochs, suggesting that the long-term decay of $E_{\mathrm{cyc,H}}$ has likely ceased after 2012.

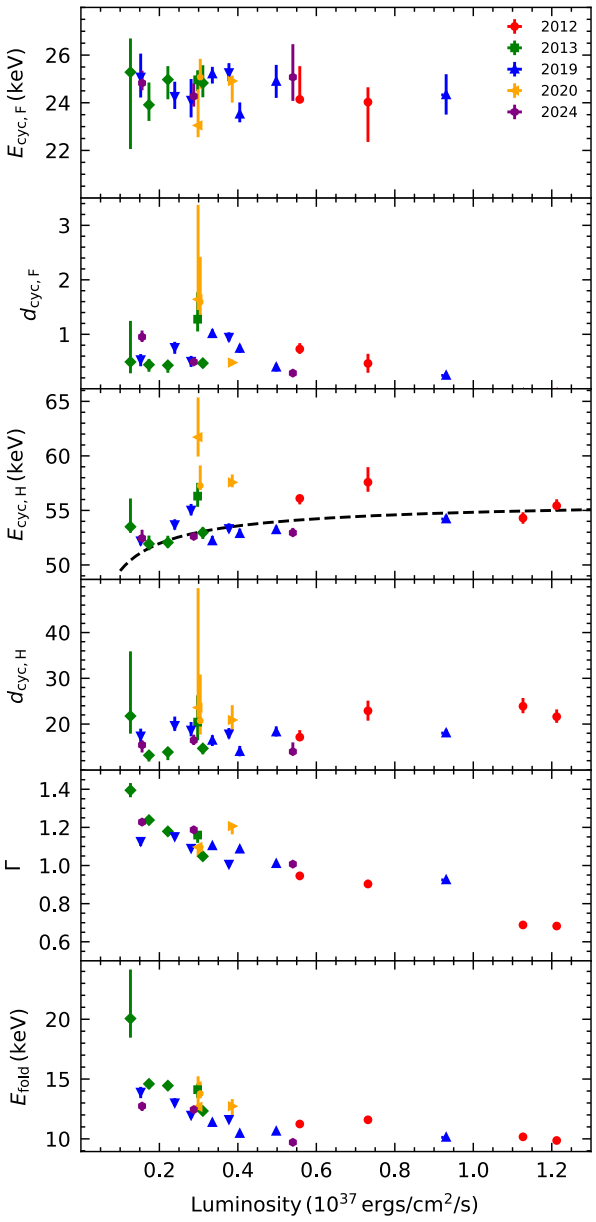


**Figure 3.11:** Flux-resolved spectral parameters derived from the pulse-to-pulse analysis in the 3–70 keV energy range. Different colors represent different observation years, while distinct marker styles within the same color correspond to different observation IDs. The dashed line in the second panel is the theoretical prediction for $E_* = 28.097 \pm 0.052$ keV (see equation 3.1).

### 3.2.4 Discussion

#### Changes of $E_{\rm cyc}$ with time

So far, only two sources, Her X-1 and Vela X-1, have shown clear long-term variability in $E_{\rm cyc}$ on timescales of decades (Staubert et al., 2020; La Parola et al., 2016; Ji et al., 2019). Our analysis confirms the previously reported decrease in the first harmonic energy in Vela X-1, which now appears to have stabilized. The long-term decay of $E_{\rm cyc,H}$ in Vela X-1 is likely a local effect at the magnetic polar cap, rather than a change in the global dipole field. Similar scenarios have been proposed for Her X-1 (Staubert et al., 2014, 2016, 2020). The decay could be connected to either a geometric displacement of the emission region in the dipole field or could be related to the accreted matter that accumulates into a magnetically supported mound and causes a change in the magnetic field configuration at the polar cap.

In addition, we observed a sudden increase in the harmonic cyclotron line energy during the years 2020 to 2023. Such dramatic evolution in the cyclotron line energy is unusual. Here is a possible explanation for the sudden increase. Matter accumulation at the magnetic poles increases the overpressure until a critical threshold is reached. This triggers interchange instabilities (e.g., ballooning instabilities (Litwin et al., 2001)) near the column boundary, causing localized magnetic field deformation and mass leakage. As a result, $E_{\rm cyc,H}$ increases because of partial column collapse, and a reduction in height. The fact that only $E_{\rm cyc,H}$ exhibits this strong variability, while the $E_{\rm cyc,F}$ remains nearly constant, may suggest that the harmonic line is more sensitive to changes in the height of the emission region.

#### Changes of $E_{\rm cyc}$ with luminosity

In our study, we first focused on the harmonic cyclotron line energy, $E_{\rm cyc,H}$. Using two *NuSTAR* observations from 2012 and 2013, Fürst et al. (2014) reported a positive correlation between $E_{\rm cyc,H}$ and luminosity. However, Diez et al. (2022), based on two *NuSTAR* observations from 2019, were unable to confirm this correlation. According to our results, the data remain relatively stable, exhibiting modestly reduced values at lower luminosities. Theoretical predictions for the $E_{\rm cyc}$–$L_{\rm X}$ relationship can be derived from Equations (51) and (58) of Becker et al. (2012):

$$E_{\rm theo} = \left[1 + 0.6 \left(\frac{R_*}{10\,\mathrm{km}}\right)^{-\frac{13}{14}} \left(\frac{\Lambda}{0.1}\right)^{-1} \left(\frac{\tau_*}{20}\right) \times \left(\frac{M_*}{1.4\,M_\odot}\right)^{\frac{19}{14}} \left(\frac{E_*}{1\,\mathrm{keV}}\right)^{-\frac{4}{7}} \left(\frac{L_x}{10^{37}\,\mathrm{erg\,s^{-1}}}\right)^{-\frac{5}{7}}\right]^{-3} \times E_*, \tag{3.1}$$

where $\tau_*$ is the Thomson optical depth, around 20 for typical HMXB parameters (Becker et al., 2012), $E_*$ is the energy of the fundamental cyclotron line at the NS surface. We adopt the values $\Lambda$=1, $R_*$=10 km and $M_*$=1.8$M_\odot$. Fitting the data using Equation 3.1, and excluding the anomalously high values from 2020, yields $E_* = 28.097 \pm 0.052$ keV, assuming a harmonic ratio of 2. The Pearson correlation coefficient is 0.462, with a p-value of 0.0405.

The fundamental CRSF energy shows a flat evolutionary trend with luminosity. The lack of a clear luminosity dependence can be explained by the photon spawning effect (Schönherr et al., 2007). In this scenario, resonant scattering events produce additional low-energy photons that preferentially populate the energy range of the fundamental line, effectively filling in the absorption feature and diminishing its depth. As a result, the fundamental line becomes less sensitive to luminosity.

### 3.2.5 Summary

- **Aim:** to study the long-term evolution and luminosity dependence of the cyclotron resonant scattering features (CRSFs) in Vela X-1 using *Swift*/BAT monitoring (2005–2024) and nine *NuSTAR* observations (2012–2024), and to disentangle intrinsic temporal evolution from luminosity effects through pulse-to-pulse spectroscopy.
- **Novelty:**
  - first detection of a renewed increase in $E_{\rm cyc,H}$ between 2020 and 2023;
  - the pulse-to-pulse method extends the accessible luminosity range to $(0.13\text{–}1.21)\times 10^{37}$ erg s$^{-1}$ and enables reliable tracking of the CRSF–luminosity relation.
- **Main results:**
  - $E_{\rm cyc,H}$ is stable after 2012 but shows a sudden and temporary increase around 2020–2023;
  - $E_{\rm cyc,H}$ is slightly lower at low luminosities and flattens at high luminosities;
  - $E_{\rm cyc,F}$ remains constant at $\sim 25$ keV, independent of time and luminosity.

## 3.3 A polarimetrically oriented X-ray stare at the accreting pulsar EXO 2030+375 (Malacaria et al., 2023)

### 3.3.1 Abstract

This study reports on the first X-ray polarimetric observation of the accreting pulsar EXO 2030+375, obtained with the Imaging X-ray Polarimetry Explorer (*IXPE*) and complemented by simultaneous monitoring from *Insight*-HXMT and SRG/ART-XC. The analysis reveals a very low phase-averaged polarization degree (about 0–3%) and a phase-resolved variation between approximately 2% and 7%. By applying a rotating vector model (RVM) to the polarization angle variation, the study constrains the system geometry, finding a magnetic obliquity of about 60°. Combined with the known orbital inclination of roughly 130°, the results imply that the magnetic axis approaches the observer's line of sight during certain pulse phases. The joint polarimetric, spectral, and timing analyses indicate a complex accretion geometry, possibly involving multipolar magnetic field components and asymmetric topologies.

### 3.3.2 Author Contributions

#### Motivation

*IXPE* provides direct measurements of the X-ray polarization of accreting pulsars, but its narrow energy range (2–8 keV) and limited photon statistics make the interpretation of polarization results strongly dependent on the assumed spectral model. An inaccurate or insufficiently constrained spectral model can bias the recovered polarization degree and angle, particularly in phase-resolved analysis. Therefore, reliable polarimetric results require simultaneous broadband spectroscopy.

HXMT offers a complementary advantage: its large effective area and wide energy coverage allow us to establish a reliable broadband continuum model and to perform phase-resolved spectroscopy with higher statistical precision. By combining *IXPE* polarimetry with HXMT spectroscopy, we can extend the energy range and stabilize the spectral model. We perform phase-resolved analysis to investigate how the emission components evolve with rotational phase, and obtain physically meaningful constraints on the geometry and radiative processes in the accretion column.

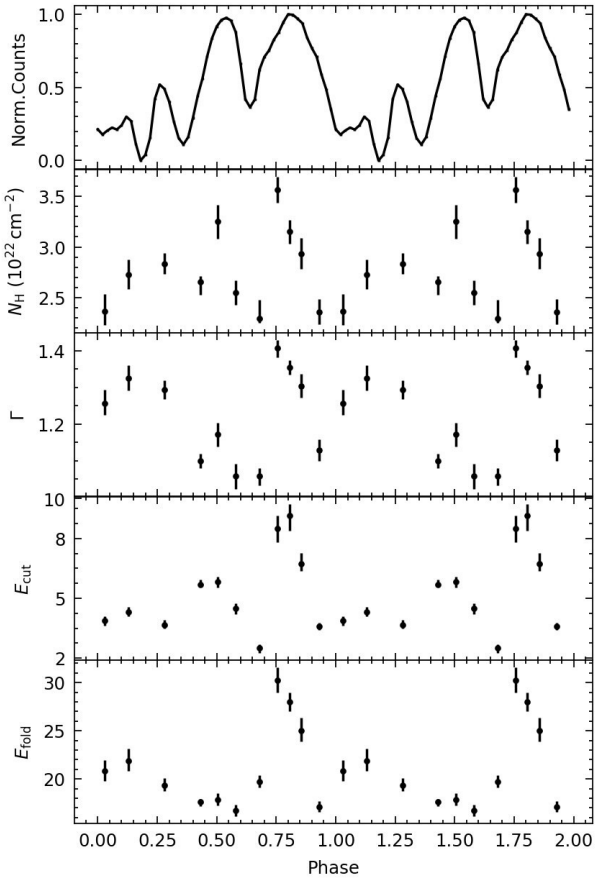


**Figure 3.12:** Best-fit parameters for the broadband (2–50 keV) phase-resolved spectra of EXO 2030+375 as observed by *HXMT*. Panels from top to bottom show the pulse profile as observed by *Insight*-HXMT/LE in the 2–10 keV energy band; the column density, $N_{\rm H}$; the power-law photon index Γ; the cutoff energy; and the folding energy (both in keV).

## Result

In this work, we performed the complete reduction and analysis of the quasi-simultaneous *Insight*-HXMT observations taken during the *IXPE* pointing in November 2022. We extracted LE, ME, and HE spectra and light curves, applied barycentric and binary corrections, constructed good time intervals, and generated background-subtracted data products following the HXMT calibration recommendations. The resulting total exposure times are 42 ks, 71 ks and 67 ks for LE, ME, and HE detectors. We restricted the energy band for spectral analysis to 1–10, 10–30, and 30–70 keV for LE, ME, and HE, respectively, as these ranges suffer smaller calibration uncertainties given the available observational background.

We conducted the pulse phase-resolved spectral analysis using 11 phase bins and modeled the spectra in the 1–50 keV range (limited to 50 keV for HE due to statistics). We obtained the best-fitting spectral parameters and demonstrated significant pulse-phase vari-

ability of the continuum properties. The best-fit results are reported in Figure 3.12. We observe a maximum value of the photon index around the main pulse profile peak, consistent with the phase-resolved results in 2021 (see Figure 3.7).

Observations carried out by Klochkov et al. (2008b) of the source show that the power-law photon index reaches a minimum around the main pulse profile peak (corresponding to the broad main peak at $\phi \sim 0.8$ in Fig. 3.12). The contrast results can be due to the luminosity difference. The beaming pattern of the accretion structure changes drastically between regimes: pulse profiles in the high-luminosity state (e.g., 2–9 keV panel in Fig. 2 of Klochkov et al. 2008b) are different from those observed in our data (top panel in Fig. 3.12). This can lead to opposite observational signatures if the observer looks through the optically deep walls of the accretion column or through the optically thin hot-spots (Mushtukov et al., 2015).

### Summary

In this work, HXMT contributes in three main ways. First, it provides the broadband, high-quality spectra required to anchor the *IXPE* spectral model, reducing uncertainties that would otherwise arise from the limited *IXPE* band. Second, it enables phase-resolved spectroscopy, revealing that the continuum parameters vary strongly with pulse phase; this information is essential for interpreting the phase-dependent polarization. Finally, the combined analysis demonstrates that the low average polarization degree and its phase evolution are consistent with a complex, non-dipolar magnetic topology and a multi-component emission geometry, rather than a simple, single-column dipole configuration.

# 4

# CONCLUSION & OUTLOOK

## 4.1 Conclusion

In this thesis, we have conducted a comprehensive investigation of accretion physics and magnetic field diagnostics in X-ray pulsars through two representative systems: the Be/X-ray binary EXO 2030+375 and the wind-fed high-mass X-ray binary Vela X-1.

During the 2021 giant outburst of EXO 2030+375, we performed a comprehensive timing and spectral study using HXMT observations. The pulse profiles exhibit strong energy and luminosity dependence, implying that changes are taking place in the geometry of emitting region. The hardness-intensity diagrams ($7-10$ keV/$4-7$ keV) indicate transitions in state during the early and late phases of the outburst. These state transitions were aligned with the luminosity levels, where changes in the pulse profile shape occurred, indicating a critical luminosity of $1.1 \times 10^{37}\,\mathrm{erg\,s^{-1}}$; Additionally, no clear evidence of CRSFs was found in the phase-averaged and phase-resolved spectra during the outburst.

In the study of Vela X-1, we exploited nearly two decades of *Swift*/BAT monitoring and nine *NuSTAR* observations spanning 2012–2024, and applied a pulse-to-pulse analysis to disentangle intrinsic long-term trends from luminosity-dependent variability. We demonstrated that the long-term decay of the harmonic cyclotron line energy has ended. The detection of a transient increase of $E_{\mathrm{cyc,H}}$ between 2020 and 2023 suggests a sudden reconfiguration of the magnetic field or accretion geometry. The fundamental line energy ($E_{\mathrm{cyc,F}}$) remained remarkably stable at $\sim 25$ keV across more than a decade, implying that the underlying dipole magnetic field is globally constant while the local field topology may evolve on shorter timescales.

Together, the two works offer a coherent picture of accreting pulsars observed under very different physical conditions and over widely separated epochs. They demonstrate that broadband spectroscopy combined with detailed timing analysis can track the evolution of the accretion geometry, and in systems with detectable CRSFs such as Vela X-1, also the magnetic field, from rapid pulse-to-pulse variability to long-term changes spanning years.

## 4.2 Outlook

Despite more than fifty years of X-ray pulsar research, no fully self-consistent model that incorporates radiation transfer, magnetohydrodynamics, and plasma microphysics has yet

been achieved. The extreme conditions close to the magnetic poles, including highly magnetized plasma, relativistic bulk motion, strong radiation pressure and complex geometries, make a complete physical treatment very challenging. As a result, the observed spectra are still generally fitted with models such as `cutoffpl`, `highecut`, or `comptt`, together with phenomenological CRSF profiles, rather than models derived from first principles. A physical framework capable of simultaneously describing the continuum, line production, and their dependence on the accretion geometry is still lacking. In the future, more comprehensive models that link the observed spectral and timing behavior with the physical conditions in the emission region will be essential to advance our understanding of accretion X-ray pulsars.

The physics of CRSFs also remains far from fully understood. Although the centroid energies are routinely used to estimate the surface magnetic field, this approach relies on simplified assumptions about line-formation height, geometry, and plasma dynamics. Variations in accretion regime, local geometry, or relativistic effects can shift CRSF energies by several keV, independent of any true magnetic evolution. In future work, I will carry out phase-resolved spectroscopy of Vela X-1 to investigate the pulse-phase behaviour of the cyclotron features. Combining such spectroscopy with polarimetric observations from missions like *IXPE* and, in the future, *eXTP*, will offer a more complete picture.

Looking ahead, major progress will come from combining refined theoretical models with observations from next-generation missions such as *eXTP*, POLAR-2, Athena, and THESEUS. These instruments will provide unprecedented broadband timing, spectroscopy, and polarimetry, enabling a shift from phenomenological interpretations toward quantitative, predictive models of compact objects in extreme environments.

# A

# PUBLICATIONS

A&A, 694, A156 (2025)
https://doi.org/10.1051/0004-6361/202451634


Astronomy & Astrophysics

# Timing and spectral studies of the Be/X-ray binary EXO 2030+375 using Insight-HXMT observations

Yu-Jia Du[1,⋆], Lorenzo Ducci[1,2], Long Ji[3], Qing-Cui Bu[4], Ling-Da Kong[1], Peng-Ju Wang[1], Youli Tuo[1], and Andrea Santangelo[1]

[1] Institut für Astronomie und Astrophysik, Universität Tübingen, Sand 1, D-72076 Tübingen, Germany
[2] ISDC Data Center for Astrophysics, Université de Genève, 16 Chemin d'Écogia, 1290 Versoix, Switzerland
[3] School of Physics and Astronomy, Sun Yat-Sen University, Zhuhai 519082, PR China
[4] Institute of Astrophysics, Central China Normal University, Wuhan 430079, PR China

Received 23 July 2024 / Accepted 13 December 2024

**ABSTRACT**

We report the results of a X-ray spectral and timing analysis of the high mass X-ray binary EXO 2030+375 during the 2021 type-II outburst based on Insight-HXMT observations. We confirm that pulsations can be detected in the energy band of 1−150 keV. The pulse profile shows both energy and luminosity dependence and variability. We observed transitions in the pulse profile shape during the rising and the decaying phase of the outburst. The pulse fraction (PF) exhibits an anti-correlation with the luminosity and a non-monotonic energy dependence, with a possible dip near 30 keV during the outburst peak. The hardness-intensity diagrams (7−10 keV/4−7 keV) suggests transitions in state during the early and late phases of the outburst. These transitions are consistent with the luminosity at which the pulse profile shape changes occur, revealing the source reached a critical luminosity and transitioned between super-critical and sub-critical accretion regimes. We performed an average and phase-resolved spectral analysis, where the flux-resolved average spectra show a stable spectral evolution with luminosity. The phase-resolved spectral analysis reveals that the dependence of spectral parameters on the pulse phase varies with changing luminosities.

**Key words.** accretion, accretion disks – binaries: general – pulsars: general – pulsars: individual: EXO 2030+375

## 1. Introduction

Be/X-ray binary (BeXRB) systems consist of an accreting neutron star (NS) characterized by $B \sim 10^{12}$ G and a O/B spectral main sequence or giant donor star (Maraschi et al. 1976; Reig 2011). In these systems, the NS can accrete matter supplied by the companion star primarily via the stellar wind or the circumstellar disc, thereby producing emission in the X-ray domain. The apparent luminosity covers many orders of magnitude from $\sim 10^{32}$ erg s$^{-1}$ up to $\sim 10^{41}$ erg s$^{-1}$ (see a recent review by Mushtukov & Tsygankov 2023). Besides the periodic (type-I) X-ray outbursts characterized by lower luminosity of roughly $L_X < 10^{37}$ erg s$^{-1}$ often observed at the periastron passage of the NS, giant outbursts (type-II) are also observed in BeXRBs with peak luminosity of $L_X \geq 10^{37}$ erg s$^{-1}$ (Reig 2011).

In these binary systems, the plasma is channeled along the magnetic field of the neutron star and accretes onto the polar cap, where the gravitational energy of the flow is released. It is believed that at luminosities greater than the critical luminosity ($L_{crit} \approx 10^{36-37}$ erg s$^{-1}$), the plasma flow is decelerated above the NS surface by the radiative pressure, leading to the formation of a radiatively dominated shock above the polar cap and the creation of an extended emission region, known as the accretion column (Basko & Sunyaev 1976; Becker et al. 2012). The pulse profiles and X-ray spectra of accreting pulsars show different properties below and above $L_{crit}$. For example, the shapes of the pulse profile of many pulsars show a significant variability around $L_{crit}$ (Tsygankov et al. 2018; Ji et al. 2020; Wang et al. 2022). Another observational tool typically used to infer properties about the different accretion regimes around $L_{crit}$ is provided by cyclotron resonant scattering features (CRSFs), which are absorption-like lines in the continuum spectrum, produced by the quantized motion of electrons in strong magnetic fields. CRSFs provide a direct measurement of the magnetic field, $E_{cyc} \approx 11.6 \times B_{12} \times (1+z)^{-1}$ keV (Staubert et al. 2019), where $B_{12}$ is the surface magnetic field strength in units of $10^{12}$ G, $z$ is the gravitational redshift due to the NS mass and radius. The energy of the fundamental CRSF shows a correlation with luminosity below $L_{crit}$ and an anti-correlation above it (Mushtukov & Tsygankov 2023, and references therein). Studies on the transition occurring around $L_{crit}$ between different accretion regimes are crucial to improving our understanding of the dynamic of accretion flow geometry and radiation mechanisms in pulsars with high magnetic fields. In this work, we present a spectral and timing analysis of one of these pulsars, EXO 2030+375, using 1−150 keV data from the Insight-HXMT satellite obtained during the 2021 giant outburst. EXO 2030+375 is a transient BeXRB discovered by the *EXOSAT* observatory during a type-II outburst in 1985. It hosts a ∼42 s pulsar orbiting around the companion star in a rather eccentric orbit ($P_{orb} \approx 46$ d, $e \sim 0.41$; Parmar et al. 1985, 1989). Its distance has been estimated as $2.4^{+0.5}_{-0.4}$ kpc by the *Gaia* Data Release 3 (Bailer-Jones et al. 2021).

Various interesting features have been observed in the broad band spectrum of EXO 2030+375. During a type-I outburst in 1996 observed by *RXTE*, Reig & Coe (1999) reported the possible detection of CRSF with a centroid energy of ∼36 keV. EXO 2030+375 was observed to undergo a second type-II

⋆ Corresponding author; du@astro.uni-tuebingen.de

outburst in 2006. A broad Gaussian emission feature around 15 keV has been observed (Klochkov et al. 2007). A possible CRSF was reported at ~63 keV in phase-resolved spectra extracted during the peak of the 2006 outburst (Klochkov et al. 2008a). *Suzaku* observations of EXO 2030+375 during type-I outbursts in 2007 and 2012 did not reveal the presence of CRSFs in the X-ray spectrum (Ferrigno et al. 2016). The third giant outburst was detected in 2021. Fu et al. (2023) reported the evolution of the pulse profile with luminosity and provided an updated set of orbital and temporal parameters of EXO 2030+375 with Insight-HXMT. During a 2022 type-I outburst, Malacaria et al. (2023) used *IXPE* to find that the polarization degree ranged from 0% to 3% in phase-averaged analysis and from 2% to 7% in phase-resolved analysis. Their combined polarimetric, spectral, and timing analyses revealed a complex accretion geometry for EXO 2030+375, significantly influenced by asymmetric magnetic multipoles and gravitational light bending.

In this work, we present the spectral and timing analysis of EXO 2030+375, using the data of Insight-HXMT during the 2021 giant outburst. The observations and data processing are given in Sect. 2. We present the dependence of the pulse profile with time and energy. We analyzed phase-averaged, phase-resolved spectra of the 2021 outburst to explore spectral variations. The results are given in Sect. 3. In Sects. 4 and 5, we discuss and summarize our results. Additionally, we provide supplementary results that support our main findings in the appendix.

## 2. Observations and data reduction

The Hard X-ray Modulation Telescope (Insight-HXMT, also known as HXMT; Zhang et al. 2020), launched on 15th June 2017, is the first Chinese X-ray astronomical satellite. HXMT excels in its broad energy band (1−250 keV) and a large effective area in the hard X-rays energy band (Zhang et al. 2020). EXO 2030+375 was observed by Insight-HXMT from 2021 July 28 (MJD 59423) to November 21 (MJD 59539). Figure 1 presents the light curves of EXO 2030+375 during the 2021 giant outburst. The top panel displays the 2−20 keV light curve observed by MAXI[1] (Matsuoka et al. 2009), while the bottom panel shows the light curve derived from the Insight-HXMT observations through spectral fitting. There are 65 observations of the proposal P0304030 and 15 observations of the proposal P0404147, with a total exposure time of ~2460 ks. Especially, observations of the proposal P0404147 were at the peak of the outburst. The observations utilized for the timing and spectral analysis of the source can be found in Appendix A (Table A.1) The exposures were combined by date to enhance the statistics using `addspec` in `heasoft` (version 6.31.1). The detectors of three payloads (LE: 1−15 keV, 384 $cm^2$; ME: 5−30 keV, 952 $cm^2$; HE: 20−250 keV, 2100 $cm^2$) on board Insight-HXMT were used to generate the events in good time intervals (GTIs). The time resolution of the HE, ME, and LE instruments are ~25 μs, ~280 μs, and ~1 ms, respectively. Data from Insight-HXMT were considered in the range 2−150 keV, with the exclusion of 21−23 keV data due to the presence of an Ag feature (Li et al. 2020). Insight-HXMT Data Analysis software[2] (HXMTDAS) v2.04 and HXMTCALDB v2.04 were used to analyze the data. We screened events for three payloads in HXMTDAS using `legtigen`, `megtigen`, `hegtigen` tasks according to the following criteria for the selection of GTIs: (1) pointing offset angle <0.1°; (2) the elevation angle >10°; (3) the geomagnetic cut-off rigidity >8 GeV; (4) the time before and after the South Atlantic Anomaly passage >300 s; and (5) for LE observations, pointing direction above bright Earth >30°. We selected events from the small field of views (FoVs) for LE and ME observations, as well as from both small and large FoVs for HE observations due to the limitation of the background calibration. HXMT is a non-imaging telescope, the background is generated using a background model constructed through training and calibration on multiple calibration sources of the blind detectors, which are covered by tantalum lid. The software for background realization is incorporated in `lebkgmap` (Cao et al. 2020), `mebkgmap` (Cao et al. 2020), and `hebkgmap` (Liu et al. 2020) implemented in HXMTDAS, respectively. The arrival times of photons at HXMT are corrected to the Solar system barycentre by `hxbary` in HXMTDAS. The correction of the arrival times to account for the orbital modulation was performed using the orbital ephemeris reported by Fu et al. (2023). The XSPEC v12.13.0c software package (Arnaud 1996) was used to perform the spectral fitting. We included renormalisation constant factors in all the spectral fittings to account for inter-calibration uncertainties between the three Insight-HXMT instruments. The uncertainty estimated for each spectral parameter is for 90% confidence, and a systematic error of 1% is added to LE, ME, and HE spectrum.

[1] The MAXI data were retrieved from http://maxi.riken.jp/star_data/J2032+376/J2032+376.html

[2] http://hxmtweb.ihep.ac.cn/

## 3. Results

### 3.1. Timing analysis

The 0.01−150 keV light curve of the 2021 outburst is presented in the second panel of Fig. 1. Luminosities were derived from the spectral analysis detailed in Sect. 3.2. The outburst reaches its maximum luminosity at MJD 59466. The duration of the rising phase of the outburst is approximately 40 days, spanning from MJD 59427 to MJD 59466, and covering a luminosity range of $0.55 \times 10^{37}$ erg $s^{-1}$ to $1.45 \times 10^{37}$ erg $s^{-1}$. The duration of the decay phase is approximately 69 days, spanning from MJD 59466 to MJD 59535, and covering a luminosity range of $1.45 \times 10^{37}$ erg $s^{-1}$ to $0.31 \times 10^{37}$ erg $s^{-1}$.

Figure 2 shows the temporal evolution of the pulse profiles of EXO 2030+375. To enhance the statistics, data within one day was combined. To accurately measure the spin period for timing analysis, we performed epoch folding (Leahy 1987) on the extracted light curves. The profiles were obtained from light curves with a bin size of 0.5 s extracted in three energy bands (LE: 1−10 keV, ME: 10−30 keV, HE: 25−100 keV). The pulse profiles were aligned, with phase zero defined as the minimum value of the pulse profile.

A two-peak structure at lower flux can be clearly identified for the 1−10 keV and 10−30 keV energy bands. The main peak at ~0.60 phase remains stable throughout the outburst, with its intensity decreasing near the end. Conversely, as the outburst rises, the intensity of the secondary peak at ~0.35 phase decreases. When the luminosity exceeds $\sim 1.0 \times 10^{37}$ erg $s^{-1}$, the intensity of the secondary peak remains relatively low until the luminosity decreases back to $\sim 1.0 \times 10^{37}$ erg $s^{-1}$. At this point, the intensity of the secondary peak increases again, gradually becoming higher than that of the main peak, with the secondary peak eventually becoming dominant as the main peak's amplitude decreases. For HE, the secondary peak is not as prominent as it is for LE and ME; the main peak remains more dominant. However, higher intensity can still be observed at phase 0.3−0.5

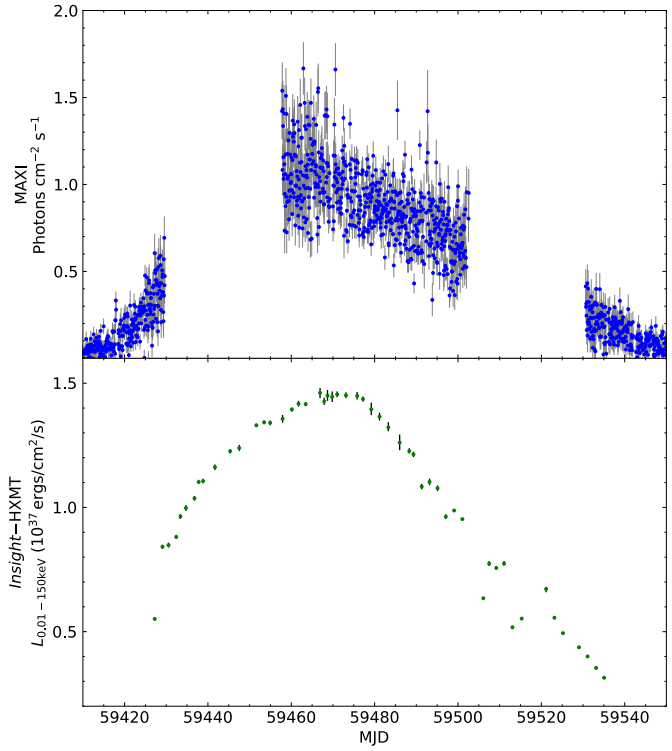


**Fig. 1.** Light curve of EXO 2030+375 as measured by MAXI (2−20 keV), with data binned over one orbital revolution of the International Space Station, where MAXI is mounted (∼1.5 hours), shown in the first panel. The second panel shows the light curve from the Insight-HXMT observations during the 2021 giant outburst. Each point represents the daily-averaged luminosity (0.01−150 keV), derived through spectral fitting of the Insight-HXMT data.

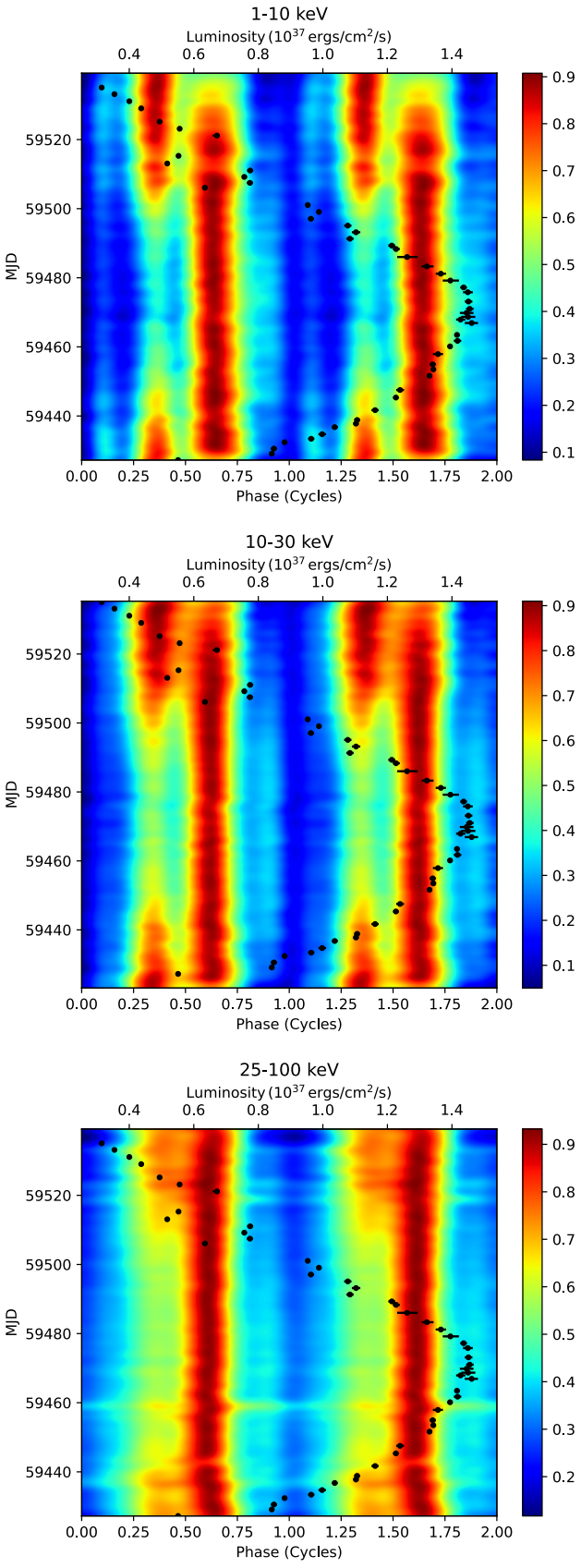


**Fig. 2.** 2D maps describe the evolution of the pulse profile with time observed by Insight-HXMT during the 2021 outburst (proposal P0304030 and P0404147, MJD 59427−59535). Top: 1−10 keV; middle: 10−30 keV; and bottom: 25−100 keV. The black points in the figure represent the luminosity (0.01−150 keV).

at lower luminosities. In general, the secondary peak at ∼0.35 phase dominates at lower luminosities, while the main peak at ∼0.60 phase dominates at higher luminosities.

Figure 3 presents the energy-resolved (1−10, 10−15, 15−20, 20−30, 30−40, 40−50, 50−60, 60−70, 70−100, 25−100, and 100−150 keV) background-subtracted pulse profiles of the source obtained near the maximum of the 2021 outburst (ObsID P0404147, MJD 59460−59461). The four-peak pulse profile evolves to a single peak as the energy increases. The small peak at ∼0.1 phase gradually decreases with increasing energy and is no longer detectable above 30 keV. Another small peak at ∼0.9 phase gradually decreases when the energy exceeds 40 keV. The main peak at ∼0.60 phase was dominant at all energy bands while the secondary peak at ∼0.35 phase can only be detected below 70 keV. Pulsations can still be detected above 100 keV.

We defined the pulse fraction (PF) parameter as the ratio of the difference to the sum of the maximum, $P_{\rm max}$, and minimum, $P_{\rm min}$, intensities of pulse profile, PF $= \frac{P_{\rm max}-P_{\rm min}}{P_{\rm max}+P_{\rm min}}$. The variations in the PL with the energy at different luminosities during the rise ($L \sim 1.16\times10^{37}$ erg s$^{-1}$), near the peak ($L \sim 1.40\times10^{37}$ erg s$^{-1}$), and during the decay ($L \sim 5.56\times10^{36}$ erg s$^{-1}$) are shown in Fig. 4. The horizontal errors represent the energy ranges for which the PF is calculated, and the vertical errors indicate the corresponding error in PF measurements. In general, the pulse fraction increases with energy, while a bump around 10 keV was observed near the peak of the outburst. Figure 5 shows the variation in the pulse fraction (25−100 keV) with the luminosity throughout the outburst, revealing an anti-correlation between

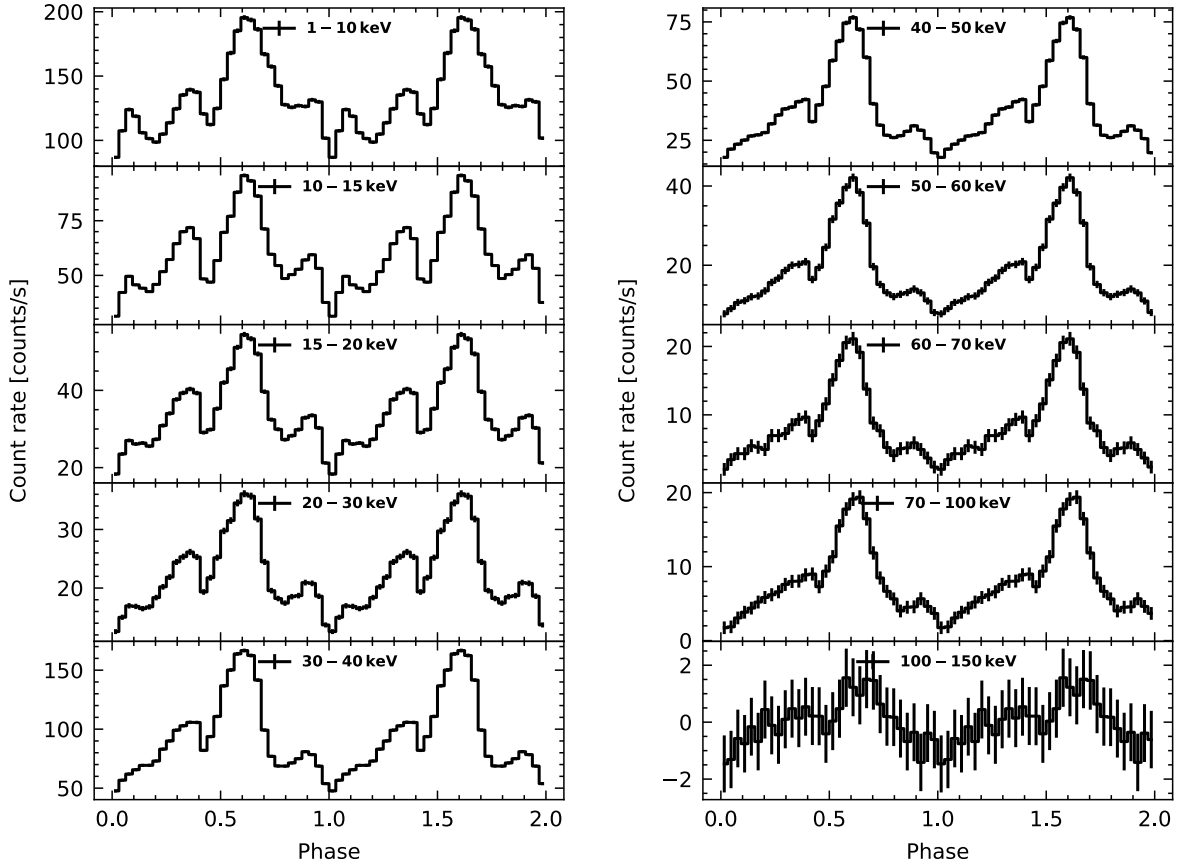


**Fig. 3.** Energy-resolved pulse profiles of EXO 2030+375 near the maximum of the outburst.

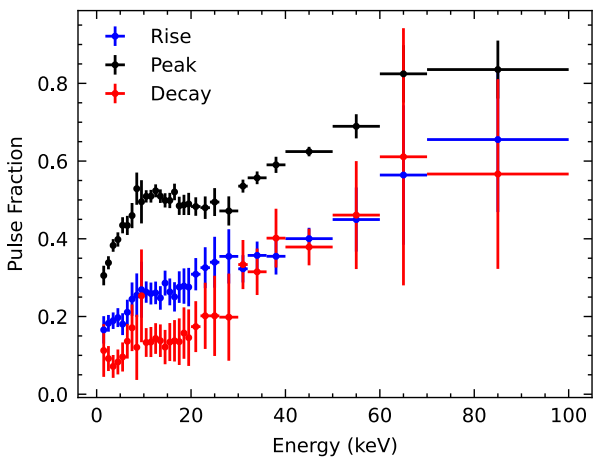


**Fig. 4.** Variation in the PF with energy (keV). Rise: P0304030016, $L \sim 1.16 \times 10^{37}$ erg s$^{-1}$. Peak: P0404147, and $L \sim 1.40 \times 10^{37}$ erg s$^{-1}$. Decay: P0304030060, $L \sim 5.56 \times 10^{36}$ erg s$^{-1}$.

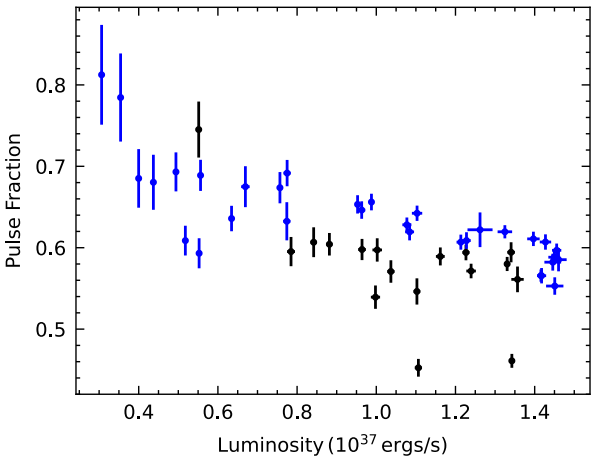


**Fig. 5.** Variation in pulse fraction with luminosity in 25−100 keV energy range during the 2021 outburst. Black crosses represent the rise of the outburst, blue the decay.

the pulse fraction and luminosity during both the rise and decay phases.

### 3.2. Phase-averaged analysis

The outbursts of accreting pulsars typically go through different spectral states, which can be diagnosed using a hardness-intensity diagram (HID) (Reig & Nespoli 2013). HID shows how a source spectral hardness – defined as the ratio of count per second (or flux) between two distinct X-ray energy bands – varies with its total intensity. Figure 6 displays the net light curves in the energy ranges of 4−7 keV and 7−10 keV for all observations, as well as the hardness ratio of 7−10 keV/4−7 keV versus time. The light curves are rebinned to one–day intervals. The hardness ratio is divided into four parts, represented by different colors, to illustrate its evolution over time. Figure 7 displays the HID.

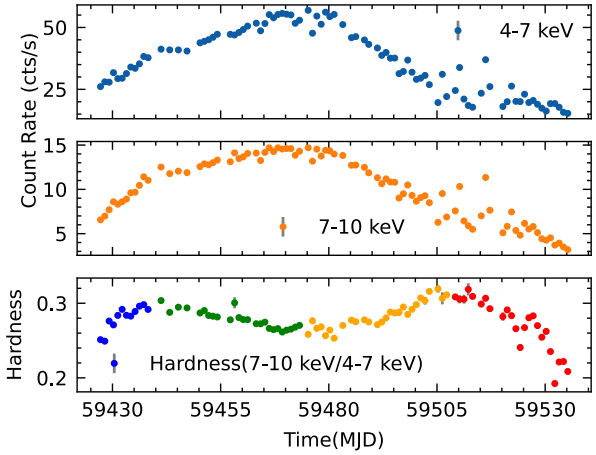


**Fig. 6.** Net light curves and hardness of EXO 2030+375 of all observations from MJD 59427 to MID 59535. The hardness is defined as the ratio 7−10 keV/4−7 keV. Each point corresponds to the data of one day. The evolution of hardness over time is represented by dividing it into four distinct periods, each indicated by a different color: blue (MJD 59427 to 59438), green (MJD 59438 to 59473), orange (MJD 59473 to 59508), and red (MJD 59508 to 59535).

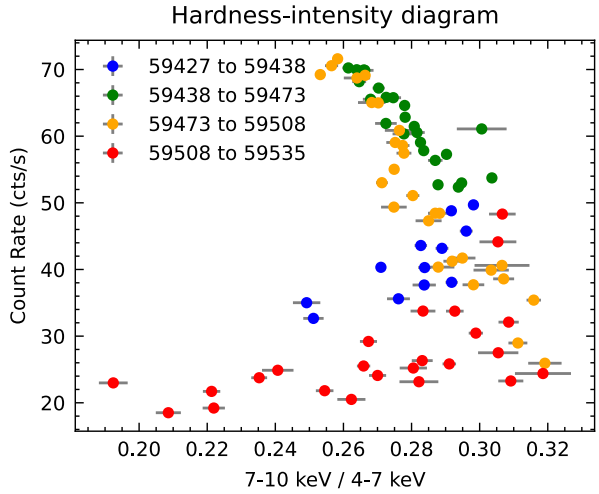


**Fig. 7.** HID extracted from Insight- HXMT/LE data. Hardness is defined as the ratio 7−10 keV/4−7 keV. The colors are described in the same way as in Figure 6.

Table A.1 lists all the observations. We first focused on the observations near the peak of the 2021 outburst (MJD 59460−59461). To enhance the counting statistics of the energy spectra, we combined seven exposures within a single day (see Table A.1: obs. IDs: 107[a], 108[a], 109[a], 110[a], 111[a], 112[a], and 113[a]) using the `addspec` and `addrmf` tasks. We restricted the energy bands for spectral analysis to 2−10 keV, 10−30 keV, and 28−50 keV for LE, ME, and HE, respectively, due to the relatively higher background above 50 keV.

Our choice of continuum model is based on earlier analyses of EXO 2030+375 (e.g., Klochkov et al. 2007). The model consists of an absorbed cutoff power-law and a blackbody component, the latter included to account for the soft excess observed below ∼5 keV.

In `xspec`, we employed a cross-normalization constant to fit all instruments jointly and adopted the `tbabs` absorption model, setting the abundances to `wilm` (Wilms et al. 2000). We added a Gaussian function centered around ∼6.6 keV, which likely corresponds to higher ionization states of iron, observed in higher luminosity observations (Klochkov et al. 2007; Ferrigno et al. 2016).

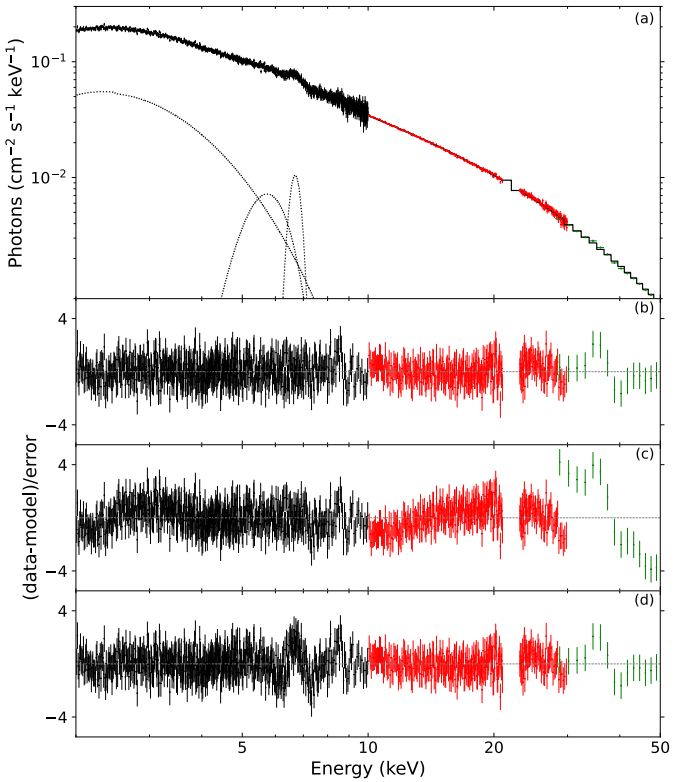


**Fig. 8.** Broadband spectrum of EXO 2030+375 at the peak of the 2021 giant outburst in energy range 2−50 keV using the model `const×tbabs(gauss+bbodyrad+gauss+cutoffpl)`. (a) unfolded spectrum; (b) residuals for the best-fit model; (c) residuals after fitting without the blackbody component; and (d) residuals after fitting without the feature around 5.7 keV.

Additionally, we included a second Gaussian component at ∼5.7 keV. This feature arises from discrepancies in single-split event count rates across the three LE detector boxes (private communication with the HXMT calibration team). Importantly, this feature does not impact the rest of the analysis or the main results. Panel d in Fig. 8 shows the residuals when the ∼5.7 keV component is excluded from the spectrum: a residual feature appears at ∼6.16 keV. This artifact occurs because the Gaussian component initially included to model the iron line attempts to fit the ∼5.7 keV feature as well.

The best-fit model, consisting of an absorbed cutoff power-law with a blackbody and two Gaussian components, resulted in a $\chi^2$ value of 938.85 for 1250 degrees of freedom. The blackbody temperature was determined to be $kT = 0.74 \pm 0.03$ keV, with the radius of the emitting region estimated at $4.4^{+0.4}_{-0.5}$ km, assuming a distance of 2.4 kpc. The best-fit photon index was $0.942 \pm 0.025$, and the cutoff energy was $18.3 \pm 0.5$ keV. The interstellar absorption ($N_{\rm H}$) was found to be $(2.32 \pm 0.13) \times 10^{22}$ atoms cm$^{-2}$. Table 1 provides a comprehensive summary of the spectral parameters derived from the best-fit model.

When the spectrum was fitted without the blackbody component, the $\chi^2$/d.o.f. increased to 1217.04/1252, and the residuals (Fig. 8, panel c) worsened significantly. In this case, the best-fit required the constant parameter for the HE data (green points in Fig. 8) to shift to a much lower value compared to that listed in Table 1. If this constant is frozen at its previous value, the

**Table 1.** Best-fit parameters of the phase-averaged broadband spectrum of EXO 2030+375 as observed by Insight-HXMT at the maximum of the outburst using the model `const×tbabs(gauss+bbodyrad+gauss+cutoffpl)` in the 2–50 keV energy band.

| Parameter | Value |
|---|---|
| $C_{\rm LE}$ (fixed) | 1 |
| $C_{\rm ME}$ | $0.929 \pm 0.006$ |
| $C_{\rm HE}$ | $0.882 \pm 0.011$ |
| $N_{\rm H}$ [$10^{22}$ cm$^{-2}$] | $2.32 \pm 0.13$ |
| $\Gamma$ | $0.942 \pm 0.025$ |
| Norm$_\Gamma$ | $0.565 \pm 0.002$ |
| $kT_{\rm bb}$ [keV] | $0.74 \pm 0.03$ |
| Norm$_{\rm bb}$ | $335.4 \pm 64.4$ |
| $E_{\rm cut}$ [keV] | $18.3 \pm 0.5$ |
| $E_{\rm K\alpha}$ [keV] | $6.69 \pm 0.02$ |
| $\sigma_{\rm K\alpha}$ [keV] | $0.20 \pm 0.04$ |
| Norm$_{\rm K\alpha}$ | $0.005 \pm 0.001$ |
| $E_{\rm line}$ [keV] | $5.71 \pm 0.09$ |
| $\sigma_{\rm line}$ [keV] | $0.62 \pm 0.12$ |
| Norm$_{\rm line}$ | $0.012 \pm 0.002$ |
| Flux$_{0.01-150\,\rm keV}$ | $2.239 \pm 0.024$ |
| $\chi^2$/d.o.f. | 938.85/1250 |

**Notes.** Normalization of the power law in units of photon cm$^{-2}$ s$^{-1}$ keV$^{-1}$ at 1 keV. Unabsorbed flux (in units of $10^{-8}$ erg cm$^{-2}$ s$^{-1}$) calculated for the entire model, obtained using the `cflux` command from XSPEC as resulting from the *HXMT* data. Uncertainties are given for a 68% confidence level.

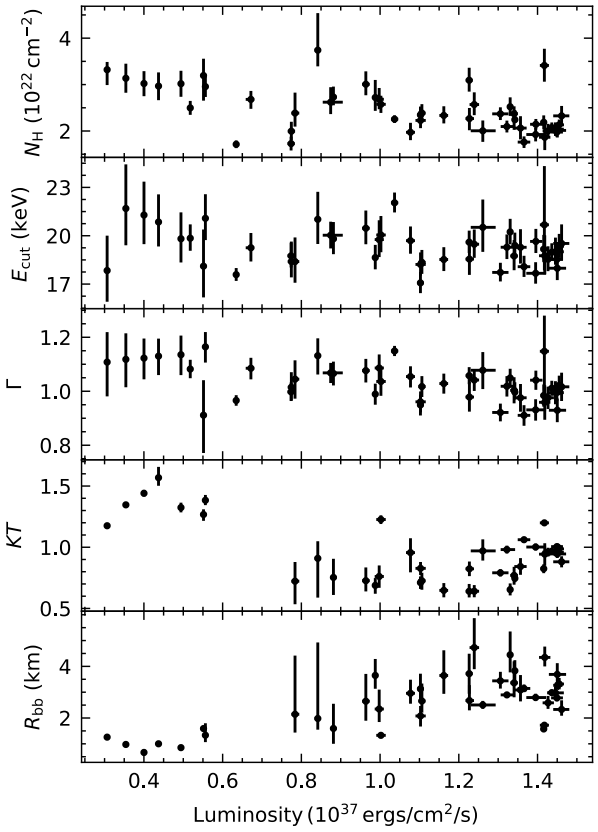


**Fig. 9.** Flux-resolved parameters using all the observations of the 2021 giant outburst in energy range 2–50 keV.

residuals exhibit a more pronounced wavy structure. To assess the statistical significance of the blackbody component, we performed an F-test, which yielded a probability of $10^{-70}$, strongly supporting the inclusion of the blackbody component in the model. Throughout the analysis, the `cflux` convolution model was used to compute all unabsorbed flux values.

The cutoff power-law with blackbody model discussed above was applied to fit the average spectrum for all the observations. For ObsID P0304030051, P0304030052, P0304030054, P0304030055, and P0304030059, the inclusion of the blackbody component was unnecessary to achieve a good fit. We also investigated spectral variability as a function of accretion luminosity. Given the smooth variation in the spectral parameters throughout the outburst, exploring correlations with X-ray flux is meaningful. The flux-resolved parameters are shown in Fig. 9. The parameters involved are the equivalent hydrogen column density ($N_{\rm H}$), the photon index ($\Gamma$), the folding energy ($E_{\rm cut}$), the blackbody temperature ($kT_{\rm bb}$), and the size of the emitting region ($R_{\rm bb}$). The photon index ranges from 0.8 to 1.3, while the cutoff energy varies between 16 keV and 24 keV. Overall, the spectral continuum demonstrates stable evolution with luminosity. Initially, the blackbody temperature rises with luminosity until reaching $0.5\times10^{37}$ erg s$^{-1}$, beyond which it decreases. The blackbody radius evolves inversely with the temperature.

### 3.3. Phase-resolved analysis

The phase-resolved spectral analysis of the outburst rise, peak, and decay were performed to explore variations of spectral parameters with pulse phase and different luminosities. Eleven phase bins were selected to sample different intensity levels shown by the pulse profile. To detect the presence of a possible CRSF, we initially extracted spectra across a broader energy range, namely, from 2–100 keV. However, no definitive evidence of CRSF was observed. To minimize the impact of high background and maintain consistency in our spectral analysis, we ultimately narrowed the energy range to 2–50 keV when presenting our results (see Appendix B for more details). To enhance the statistics, observations in the similar flux levels were combined: rise: 59436–59438 MJD, $L \sim 1.0 \times 10^{37}$ erg s$^{-1}$; peak: 59460–59461 MJD, $L \sim 1.40 \times 10^{37}$ erg s$^{-1}$; decay: 59529–59533 MJD, $L \sim 0.4 \times 10^{37}$ erg s$^{-1}$. The spectra obtained for eleven phase bins were fitted again with the same continuum model with the corresponding phase-averaged spectra. During the rise and decay phases of the outburst, when the flux was relatively low, the spectral feature at approximately ~5.7 keV, identified in the average spectrum near the peak of the outburst (Sect. 3.2), was not required to fit the data in individual phase bins. Consequently, the Gaussian component representing this feature was excluded from the best fit model, which for these parts of the outburst was: const×tbabs×(bbodyrad+gauss+cutoffpl). At the peak of the outburst (59460–59461 MJD), the Gaussian component at ~5.7 keV was included to account for the observed feature, as in the average spectrum model. The resulting `xspec` model for this interval was: const×tbabs×(gauss+bbodyrad+gauss+cutoffpl). The best-fit phase-resolved continuum parameters as a function of the pulse phase are reported in Fig. 10. To investigate the variation in the phase-resolved parameters with pulse profile morphology, we generated average pulse profiles for the LE (1–10 keV) energy band across the three time intervals. The LE band was chosen because the evolution of the main peak and the secondary peak with varying luminosities is most evident in

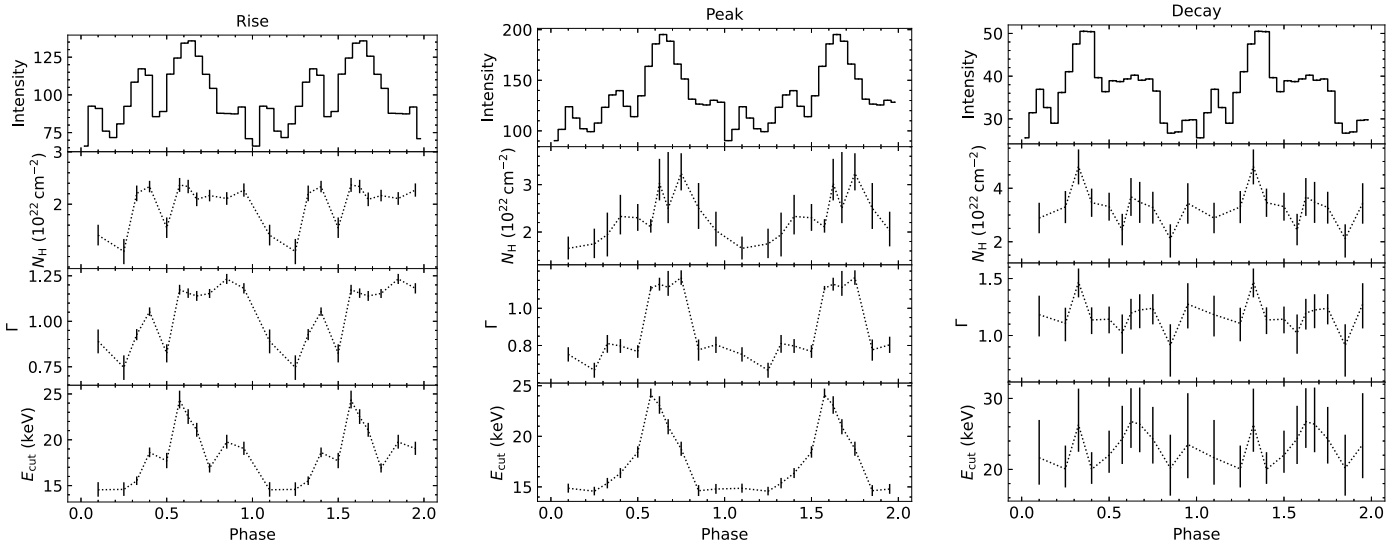


**Fig. 10.** Modulation of phase-resolved parameters observed by Insight-HXMT. Rise: MJD 59436−59438, $L \sim 1.0 \times 10^{37}$ erg s$^{-1}$; peak: 59460−59461 MJD, $L \sim 1.45 \times 10^{37}$ erg s$^{-1}$; decay: 59529−59533 MJD, $L \sim 0.4 \times 10^{37}$ erg s$^{-1}$. For each of the three subfigures, the panels (from top to bottom) show the pulse profile (1−10 keV), the column density ($N_H$), the power-law photon index (Γ), and the cutoff energy ($E_{cut}$).

this energy range. The disparity in the amplitude of the peaks is clearly observable.

For all the three time intervals, the power-law photon index shows a strong dependence on the pulse profile. Near the peak of the outburst, it reaches the highest at the main peak at phase ∼0.6. During the rise of the outburst, the photon index remains consistently high on the right flank of the main peak (phase 0.70−0.95). During the decay of the outburst, the amplitude of the main peak is lower and broader than that of the secondary peak at 0.35 phase. The photon index reaches its maximum value at the peak of the secondary peak. For the three time intervals, the cutoff energy varies with pulse phase, reaching its highest value at the peak of the main pulse.

## 4. Discussion

We have studied spectral and timing characteristics of accreting pulsar EXO 2030+375 in the 2021 outburst with Insight-HXMT. During the observation, the X-ray luminosity (0.01−150 keV) was between $0.31 \times 10^{37}$ erg s$^{-1}$ and $1.45 \times 10^{37}$ erg s$^{-1}$ assuming the distance of 2.4 kpc.

Reig & Nespoli (2013) presented the hardness-intensity diagram (HID) of the 2006 outburst of EXO 2030+375 (Fig. 3 in Reig & Nespoli 2013), where hardness is defined as the ratio of 7−10 keV to 4−7 keV. The diagram shows a significant transition at a luminosity of $\sim 4 \times 10^{36}$ erg s$^{-1}$ ($d = 2.4$ kpc). The study indicates that for several X-ray pulsars, including EXO 2030+375, the evolution through the HID suggests state transitions during the early and late phases of the outburst. They demonstrate that these state transitions occur when a critical luminosity is reached. Additionally, the spectral continuum also shows a transition at this luminosity (Fig. 6 in Reig & Nespoli 2013). This indicates that in 2006, EXO 2030+375 likely underwent two different accretion regimes. These regimes are probably associated with the mechanisms by which the accretion flow is decelerated in the accretion column: radiation pressure in the supercritical regime and Coulomb interactions in the subcritical regime (Becker et al. 2012). Using Insight-HXMT data from the 2021 outburst, the HID diagram (7−10 keV/4−7 keV) shows transitions during both the rise and decay phases, indicating changes in the spectral composition. The transitions occur around MJD 59438 (rise phase) and MJD 59507 (decay phase) at $L_X \sim 10^{37}$ erg s$^{-1}$.

In the present study, the pulse profile has been observed to evolve with luminosity (Fig. 2). The double-peak structure remains present throughout, with the intensity of the main peak showing minimal variation with luminosity, while the intensity of the secondary peak exhibits significant changes. As shown in Fig. 2, the intensity of the secondary peak decreases during the rising phase, remains constant at a low value and then increases during the falling phase as the flux gradually increases. If we consider the luminosity at which the state transition in HID occurs during the rising phase as the critical luminosity, $L \sim 1.1 \times 10^{37}$ erg s$^{-1}$, we observe that the pulse profile shape transition also occurs at this luminosity. In several giant outbursts of accreting pulsars, it has been noted that the transition of the pulse shapes could serve as a hint of critical luminosities; for instance, 2S 1417−624 (Ji et al. 2020), 1A 0535+262 (Wang et al. 2022), and Swift J0243.6+6124 (Tsygankov et al. 2018). This is because the observed pulse profile shape is largely determined by the configuration of the emission region, which depends on the accretion rate. The process of pulse profile formation is complicated and hard to describe using only simple models. However, it is natural to expect a pencil beam pattern from accretion with hot spots on the neutron star surface at sub-critical mass accretion rates. At supercritical mass accretion rates, collisionless shocks and radiation-dominated accretion columns would produce a fan beam pattern (Mushtukov & Tsygankov 2023). If the pulse profile shape transitions are indeed due to EXO 2030+375 reaching a critical luminosity, we can infer that the geometries of the emitting region has always been a mixture of pencil beam and fan beam. The main peak is dominated by the fan beam, while the secondary peak is dominated by the pencil beam, with the pencil beam contributing more at lower luminosities compared to higher luminosities.

For typical neutron star parameters, Becker et al. (2012) derived the critical luminosity as $L_{crit} \sim 1.5 \times 10^{37} B_{12}^{16/15}$ erg s$^{-1}$, where $B_{12}$ is the surface magnetic field strength in units of $10^{12}$ G. The value of $L_{crit} \sim 1.1 \times 10^{37}$ erg s$^{-1}$ corresponds to a

magnetic field of $0.7 \times 10^{12}$ G. Mushtukov et al. (2015) provided a numerical solution by calculating the luminosity for two scenarios: one with purely extraordinary polarization and another with an equal mix of ordinary and extraordinary polarization. The $L_{\rm crit}$ value can only be achieved in the purely extraordinary polarization case. Since the real critical luminosity value is likely to lie between the two cases (as shown in Fig. 7 of that study), the expected cyclotron energy ($E_{\rm cycl}$) would be approximately smaller than 5 keV and larger than 30 keV. This corresponds to a magnetic field strength lower than $0.6 \times 10^{12}$ G and higher than $3.4 \times 10^{12}$ G. Using NICER data, Thalhammer et al. (2024) used relativistic raytracing to model pulse profiles, showing how complex accretion column geometries affect changes in pulse profiles across a range of luminosities. They suggested a critical bolometric luminosity of $2.3 \times 10^{36}$ erg s$^{-1}$ for the spectral transition and $7.9 \times 10^{36}$ erg s$^{-1}$ for the transition seen in the pulse profiles, deriving a surface magnetic field of $0.17-0.55 \times 10^{12}$ G. These values are slightly lower than the critical luminosity determined similarly from the Insight-HXMT data. This is probably due to the different energy range used.

The pulse profile also evolved with energy. Observations of the source close to the maximum of the outburst allowed us to perform a detailed study of this dependence (Fig. 3). The low- and high-energy profiles have a very complex structure of up to four peaks at lower energies that eventually merges to become a one-peaked profile at higher energies. The strong energy dependence of the pulse profiles has also been observed from the 2006 outburst by Klochkov et al. (2008a), using INTEGRAL observations in the 2−120 keV energy range. In general, it is a common property for accreting pulsars that they show pulse profiles with a more complex shape at lower energies, while a simple one-peak or two-peak profile at higher energies (see, e.g., Maitra & Paul 2013; Ji et al. 2020; Wang et al. 2022). Variations of pulse profiles with the energy can be caused by changes in the beam pattern on photon energy and/or local absorption due to the non-spherically symmetric distribution of matter within the system. The presence of one-peaked pulses at high energies can be attributed to a fan beam pattern in the emission geometry (Hou et al. 2022). Conversely, interpreting complex pulse profiles at low energies is more challenging due to their susceptibility to scattering and absorption within the neutron star's local environment.

The energy dependence of the PF has been extensively studied in a large sample of transient Be/X-ray binary pulsars by Lutovinov & Tsygankov (2009), including EXO 2030+375. Lutovinov & Tsygankov (2009) observed that EXO 2030+375 exhibited a consistent increase in PF with energy during its low state, a behavior similarly reported for several other pulsars. Additionally, Klochkov et al. (2008a) observed a bump-like structure around 10−20 keV at peak luminosity that is probably related to the continuum feature they found in this energy range. In our study, we observed a similar bump around 10 keV near peak luminosity, which was not present in lower luminosity states. This suggests that the bump may be luminosity-dependent, warranting further observations of EXO 2030+375 for confirmation. Additionally, the PF shows an anti-correlation with luminosity during both the rise and decay phases (see Fig. 5).

Prior spectral studies of EXO 2030+375 show some complex absorption features in its spectrum and cannot be modeled using a simple cutoff power-law model. Reig & Coe (1999) detected an additional blackbody component with $kT_{\rm bb} = 1-1.4$ keV. and a possible CRSF at ∼36 keV. The radius of the X-ray emission surface is found to be ∼1 km. By using the updated distance of 2.4 kpc, the peak luminosity of their observation is of the order of $\sim 10^{36}$ erg s$^{-1}$. The best-fit solution of the spectrum of the 2006 giant outburst ($L \sim 10^{37}$ erg s$^{-1}$, $d = 2.4$ kpc) obtained by Klochkov et al. (2007) required an additional broad emission "bump" at 15 keV or the addition of two Gaussian absorption lines at ∼10 and ∼20 keV. Reig & Nespoli (2013) observed a spectral transition from a negative to positive correlation in the $L-\Gamma$ diagram at $4 \times 10^{36}$ erg s$^{-1}$, suggesting a potential indication of the critical luminosity. Ballhausen et al. (2024) confirms the presence of a narrow absorption feature around 10 keV, its interpretation as CRSF remains uncertain due to the absence of harmonics. They also observed a spectral hardening at lower luminosities during the 2021 outburst. In our study, the broad band spectrum can be modeled by an absorbed cutoff power law associated with a blackbody component and an iron line at ∼6.6 keV. The photon index exhibited no clear evolution with luminosity, contrasting with the results from the 2006 outburst. Typically, spectral transitions are expected to be observed at critical luminosities in X-ray pulsars, reflecting changes between sub-critical and super-critical regimes (Reig & Nespoli 2013; Kong et al. 2020). One possible explanation is that the large error bars at lower luminosities make the spectral variability less evident. Additionally, the luminosity observed during the 2006 outburst by Reig & Nespoli (2013) ranges from $2 \times 10^{35}$ erg s$^{-1}$ to $2 \times 10^{37}$ erg s$^{-1}$, which is broader than that observed during the 2021 outburst by Insight-HXMT. It might also contribute to the absence of the spectral transition.

We see the strong energy dependence of the pulse profile shape in Fig. 10. The spectral variation with pulse phase is a common feature in X-ray pulsars (see e.g. Klochkov et al. 2008b; Lutovinov et al. 2015). Phase-resolved spectroscopy of EXO 2030+375 was also performed in earlier works. Klochkov et al. (2008a) detected a Gaussian absorption line at ∼63.6 keV between the main and secondary peaks, corresponding to a phase bin of 0.4−0.5 in our study. This could indicate the presence of a CRSF, which are sometimes detected at higher significance in correspondence of some specific pulse phases. However, no similar feature was detected in the 2021 outburst. During the 2006 giant outburst, a minimum value of the power-law photon index was observed around the main peak. The cutoff energy exhibited a slight shift with respect to the peak towards earlier pulse phases. In the 2021 outburst, the maximum of the power law photon index and the cutoff energy coincide with the main pulse (Fig. 10). During the 2022 outburst, the source was observed by IXPE, Insight-HXMT, and ART-XC across the 2−70 keV energy range, at a distance of 2.4 kpc. The observed source luminosity was $\sim 3 \times 10^{36}$ erg s$^{-1}$ (Malacaria et al. 2023, Table 2). Additionally, they reported a maximum value of the photon index around the same peak in the phase-resolved results (Malacaria et al. 2023, Fig. 7). We emphasize that the peak luminosity of the 2006 outburst was reported as $\sim 1.1 \times 10^{38}$ erg s$^{-1}$ assuming $d = 7.1$ kpc (corresponding to $\sim 1.3 \times 10^{37}$ erg s$^{-1}$ if $d = 2.4$ kpc) from Klochkov et al. (2008a), as observed with INTEGRAL JEM-X in the 2−9 keV energy range. In contrast, our peak luminosity for the 2021 outburst is $\sim 1.45 \times 10^{37}$ erg s$^{-1}$, measured across the 0.01−150 keV range. The 2006 outburst's luminosity would likely appear greater if observed across a broader energy range. As observed by *Swift*/BAT[3], the flux of the 2006 outburst was 1.2 Crab, while the 2021 outburst flux was 0.6 Crab, indicating it was half as bright as the 2006 outburst. The contrasting phase-resolved results could be attributed to differences in luminosities.

[3] https://integral.esac.esa.int/bexrbmonitor/Plots/sim_plot_EXO2030+375.html

## 5. Conclusions

We performed a comprehensive timing and spectral study of Be/X-ray binary EXO 2030+375. The pulse profiles exhibit strong energy and luminosity dependence, implying that changes are taking place in the geometry of emitting region. The hardness-intensity diagrams (7−10 keV/4−7 keV) indicate transitions in state during the early and late phases of the outburst. These state transitions were aligned with the luminosity levels, where changes in the pulse profile shape occurred, indicating a critical luminosity of $1.1 \times 10^{37}$ erg s$^{-1}$; however, the spectral properties did not exhibit a clear transition throughout the outburst. Additionally, no clear evidence of CRSFs was found in the phase-averaged and phase-resolved spectra during the outburst. Future detection of CRSFs in EXO 2030+375 could significantly enhance our understanding of the pulsar's magnetic field structure and its evolution during outbursts, as well as provide crucial insights for determining its critical luminosity.

*Acknowledgements.* This work made use of data from the Insight-HXMT mission, a project funded by China National Space Administration (CNSA) and the Chinese Academy of Sciences (CAS). Y.J. Du would like to thank the support from China Scholarship Council (CSC 202108080247). P.J. Wang is grateful for the financial support provided by the Sino-German (CSC-DAAD) Postdoc Scholarship Program (57678375). L.D. Kong is grateful for the financial support provided by the Sino-German (CSC-DAAD) Postdoc Scholarship Program (57607866). L. Ji is supported by the National Natural Science Foundation of China under grant No. 12173103. LD acknowledges funding from the Deutsche Forschungsgemeinschaft (DFG, German Research Foundation) – Projektnummer 549824807.

## References

Arnaud, K. A. 1996, ASP Conf. Ser., 101, 17
Bailer-Jones, C. A. L., Rybizki, J., Fouesneau, M., et al. 2021, AJ, 161, 147
Ballhausen, R., Thalhammer, P., Pradhan, P., et al. 2024, A&A, 688, A214
Basko, M. M., & Sunyaev, R. A. 1976, MNRAS, 175, 395
Becker, P. A., Klochkov, D., Schönherr, G., et al. 2012, A&A, 544, A123
Cao, X., Jiang, W., Meng, B., et al. 2020, Sci. China Phys. Mech. Astron., 63, 249504
Ferrigno, C., Pjanka, P., Bozzo, E., et al. 2016, XMM-Newton: The Next Decade, 44
Fu, Y.-C., Song, L. M., Ding, G. Q., et al. 2023, MNRAS, 521, 893
Hou, X., Ge, M. Y., Ji, L., et al. 2022, ApJ, 938, 149
Ji, L., Doroshenko, V., Santangelo, A., et al. 2020, MNRAS, 491, 1851
Klochkov, D., Horns, D., Santangelo, A., et al. 2007, A&A, 464, L45
Klochkov, D., Santangelo, A., Staubert, R., et al. 2008a, A&A, 491, 833
Klochkov, D., Staubert, R., Postnov, K., et al. 2008b, A&A, 482, 907
Kong, L. D., Zhang, S., Chen, Y. P., et al. 2020, ApJ, 902, 18
Leahy, D. A. 1987, A&A, 180, 275
Li, X., Li, X., Tan, Y., et al. 2020, J. High Energy Astrophys., 27, 64
Liao, J.-Y., Zhang, S., Lu, X.-F., et al. 2020, J. High Energy Astrophys., 27, 14
Liu, C., Zhang, Y., Li, X., et al. 2020, Sci. China Phys. Mech. Astron., 63, 249503
Lutovinov, A. A., & Tsygankov, S. S. 2009, Astron. Lett., 35, 433
Lutovinov, A. A., Tsygankov, S. S., Suleimanov, V. F., et al. 2015, MNRAS, 448, 2175
Malacaria, C., Heyl, J., Doroshenko, V., et al. 2023, A&A, 675, A29
Maraschi, L., Treves, A., & van den Heuvel, E. P. J. 1976, Nature, 259, 292
Maitra, C., & Paul, B. 2013, ApJ, 763, 79
Matsuoka, M., Kawasaki, K., Ueno, S., et al. 2009, PASJ, 61, 999
Mushtukov, A., & Tsygankov, S. 2023, Handbook of X-ray and Gamma-ray Astrophysics, 138
Mushtukov, A. A., Suleimanov, V. F., Tsygankov, S. S., et al. 2015, MNRAS, 447, 1847
Parmar, A. N., Stella, L., Ferri, P., et al. 1985, IAU Circ., 4066, 1
Parmar, A. N., White, N. E., Stella, L., et al. 1989, ApJ, 338, 359
Reig, P. 2011, Ap&SS, 332, 1
Reig, P., & Coe, M. J. 1999, MNRAS, 302, 700
Reig, P., & Nespoli, E. 2013, A&A, 551, A1
Staubert, R., Trümper, J., Kendziorra, E., et al. 2019, A&A, 622, A61
Thalhammer, P., Ballhausen, R., Sokolova-Lapa, E., et al. 2024, A&A, 688, A213
Tsygankov, S. S., Doroshenko, V., Mushtukov, A. A., et al. 2018, MNRAS, 479, L134
Wang, P. J., Kong, L. D., Zhang, S., et al. 2022, ApJ, 935, 125
Wilms, J., Allen, A., & McCray, R. 2000, ApJ, 542, 914
Zhang, S.-N., Li, T., Lu, F., et al. 2020, Sci. China Phys. Mech. Astron., 63, 249502

## Appendix A: Observations

**Table A.1.** Insight-HXMT observations of EXO 2030+375 during the 2021 outburst used for data analysis.

| Observation ID | Date (MJD) | Exposure (s) | | |
|---|---|---|---|---|
| | | LE | ME | HE |
| 03 | 59427.23 | 1725 | 2522 | 3579 |
| 04 | 59429.09 | 2274 | 4306 | 4118 |
| 05 | 59430.55 | 6022 | 6170 | 5537 |
| 07 | 59432.46 | 4847 | 5856 | 5169 |
| 08 | 59433.45 | 3950 | 6018 | 5166 |
| 09 | 59434.73 | 2785 | 3958 | 4886 |
| 11 | 59436.78 | 3691 | 6231 | 4137 |
| 12 | 59437.78 | 5053 | 6475 | 2986 |
| 13 | 59438.84 | 6357 | 6646 | 5468 |
| 16 | 59441.69 | 6394 | 7558 | 5320 |
| 18 | 59445.37 | 4999 | 7817 | 6148 |
| 19 | 59447.52 | 2439 | 4625 | 6430 |
| 21 | 59451.62 | 4842 | 7544 | 6233 |
| 23 | 59453.48 | 4949 | 7944 | 6268 |
| 24 | 59454.93 | 1705 | 2206 | 2825 |
| 25 | 59457.92 | 958 | 2575 | 1752 |
| 107[a] | 59460.11 | 299 | 1696 | 492 |
| 108[a] | 59460.24 | 946 | 3328 | 4236 |
| 109[a] | 59460.38 | 416 | 2800 | 1777 |
| 110[a] | 59460.51 | 1257 | 2384 | 1403 |
| 111[a] | 59460.64 | 2095 | 2165 | 2859 |
| 112[a] | 59460.77 | 1822 | 1963 | 2581 |
| 113[a] | 59460.91 | 599 | 656 | 874 |
| 26 | 59461.74 | 3742 | 3440 | 3974 |
| 27 | 59463.47 | 6791 | 7781 | 7543 |
| 28 | 59464.85 | 838 | 1643 | 1376 |
| 29 | 59465.74 | 1525 | 1521 | 2013 |
| 30 | 59466.98 | 1076 | 2241 | 1865 |
| 31 | 59467.84 | 2334 | 3785 | 4244 |
| 32 | 59468.69 | 2035 | 2495 | 2765 |
| 33 | 59469.82 | 2274 | 3406 | 3569 |
| 34 | 59471.01 | 5686 | 8356 | 6145 |
| 35 | 59473.13 | 5686 | 8084 | 5745 |
| 36 | 59475.81 | 6118 | 12074 | 8997 |
| 37 | 59477.18 | 4317 | 11427 | 10438 |
| 38 | 59479.17 | 3721 | 4417 | 4346 |
| 39 | 59481.16 | 6118 | 4465 | 5414 |
| 40 | 59483.29 | 3967 | 4993 | 6851 |
| 41 | 59486.01 | 1496 | 1786 | 1340 |
| 42 | 59488.32 | 1887 | 3548 | 4766 |
| 43 | 59489.31 | 4856 | 7150 | 6345 |
| 44 | 59491.30 | 1886 | 3851 | 4874 |
| 45 | 59493.18 | 3651 | 5752 | 6963 |
| 46 | 59495.09 | 3855 | 6016 | 7551 |
| 47 | 59497.08 | 1647 | 6496 | 6929 |
| 48 | 59499.06 | 3015 | 7020 | 7916 |
| 51 | 59506.08 | 1409 | 5484 | 5381 |
| 52 | 59507.48 | 958 | 3672 | 2787 |
| 54 | 59511.05 | 1197 | 7559 | 6635 |
| 55 | 59513.08 | 2769 | 8764 | 6949 |
| 56 | 59515.29 | 3032 | 5933 | 7083 |
| 59 | 59521.15 | 7401 | 10512 | 6292 |
| 60 | 59523.16 | 7336 | 11385 | 9217 |
| 61 | 59525.20 | 4144 | 8897 | 6228 |
| 62 | 59527.13 | 3084 | 5364 | 6263 |
| 63 | 59529.05 | 8411 | 8789 | 8060 |
| 64 | 59531.10 | 6026 | 7309 | 6141 |
| 65 | 59533.15 | 4992 | 6941 | 5169 |
| 66 | 59535.06 | 4927 | 7133 | 5558 |

**Notes.** For each observation ID, P03040300 should be prefixed. For observation IDs marked with (a) in the upper right corner, P040414700 should be prefixed, and 20210903-02-01 should be appended.

## Appendix B: Pulse-on and pulse-off spectral analysis

We wish to highlight our decision to restrict the energy range to 2−50 keV for the spectral analysis, aiming to focus on an energy range with reliable background calibration. Initially, we analyzed data ranging from 2−100 keV. As illustrated in Fig B.1, the asterisk marks denote the background values for ObsID P030403002703. The characteristic "U-shaped" background (see in (Liao et al. 2020) for the description of the background model) observed between 40 keV and 50 keV, may be responsible for the feature seen around 47 keV. For a more thorough investigation of the feature, we performed pulse-on and pulse-off spectrum analysis for ObsID P030403002703. This analysis involves comparing the X-ray spectra at different phases of the pulsar's rotation, specifically when the pulsar's emission is strongest (pulse-on) and weakest (pulse-off). By using the spectrum from the weakest phase as the background, this method helps avoid the influence of an excessively high background, which can otherwise obscure the true emission features. The phase bin extracted for the pulse-on spectrum covered phases 0.5-0.7 (mostly encompassing the main peak), while the phase bin for the pulse-off spectrum covered phases 0.97-1.03 (centered on the lowest flux). As seen in Fig B.2, we did not observe the 47 keV feature and the background is significant above 50 keV. Therefore, we restricted the energy range to 2−50 keV in this paper to minimize uncertainties associated with background.

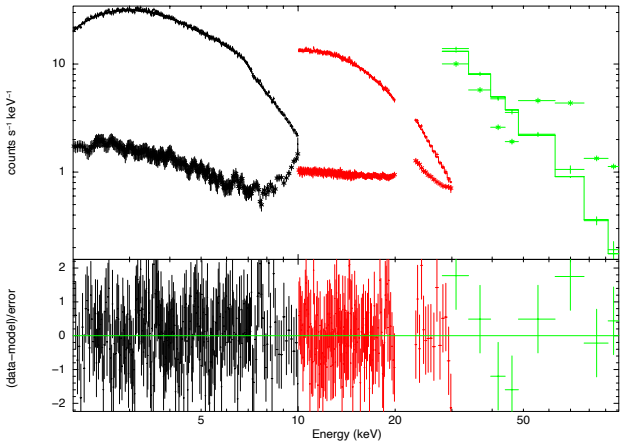


**Fig. B.1.** Broadband spectrum of EXO 2030+375 (ObsID: P030403002703) in energy range 2−100 keV using the model `const×tbabs(gauss+bbodyrad+gauss+cutoffpl)`. The asterisk marks represent background values, the solid crosses represent net spectral values, and the step line indicates the model.

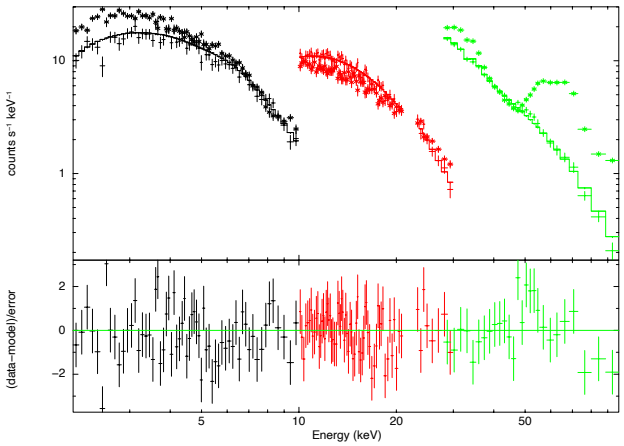


**Fig. B.2.** Pulse-on minus pulse-off spectrum of ObsID P03040300270 in the energy range 2−100 keV using the model `const×tbabs×cutoffpl`.

*Astronomy & Astrophysics* manuscript no. aa56470-25
January 5, 2026


# Long-term evolution of cyclotron resonant scattering features in the accreting pulsar Vela X-1: A pulse-to-pulse approach

Yu-Jia Du[1,⋆], Peng-Ju Wang[1], Lorenzo Ducci[1,2], Long Ji[3], Ling-Da Kong[1], Qing-Cui Bu[4], Chirag Mehrotra[1], and Andrea Santangelo[1]

[1] Institut für Astronomie und Astrophysik, Universität Tübingen, Sand 1, D-72076 Tübingen, Germany
[2] ISDC Data Center for Astrophysics, Université de Genève, 16 chemin d'Écogia, 1290 Versoix, Switzerland
[3] School of Physics and Astronomy, Sun Yat-Sen University, Zhuhai 519082, People's Republic of China
[4] Institute of Astrophysics, Central China Normal University, Wuhan 430079, P.R. China

Received 17 July 2025 / Accepted 30 November 2025

**ABSTRACT**

We investigated the long-term evolution of the cyclotron line energy, as well as the relationship between cyclotron line energy and luminosity in the high-mass X-ray binary Vela X-1, based on archival *Swift*/BAT monitoring from 2005 to 2024 and pulse-to-pulse analysis of nine *NuSTAR* observations from 2012 to 2024. Our results provide the first confirmation that the long-term decay of the harmonic line energy ($E_{\rm cyc,H}$) in Vela X-1 has ended. We further report the first detection of a transient increase in $E_{\rm cyc,H}$ between 2020 and 2023, which suggests a sudden and significant change in the magnetic field configuration or accretion geometry. In addition, $E_{\rm cyc,H}$ shows slightly lower values at low luminosities and tends to flatten at higher luminosities, in the range of $(0.13-1.21)\times10^{37}$ erg s$^{-1}$. The fundamental line energy ($E_{\rm cyc,F}$) exhibits no significant variation with time or luminosity, remaining stable at approximately 25 keV.

**Key words.** accretion, accretion disks – pulsars: general

## 1. Introduction

Vela X-1 is an eclipsing high-mass X-ray binary (HMXB) and one of the earliest X-ray sources discovered in the history of X-ray astronomy (Chodil et al. 1967). It consists of the B0.5 Ib supergiant HD 77581 (Hiltner et al. 1972), and a wind-accreting neutron star (NS) with a spin period of ∼283 s, rotating in an 8.9 d orbit around the companion. The distance to the system is $1.9\pm0.2$ kpc (Sadakane et al. 1985). The mean luminosity is $5\times10^{36}$ erg s$^{-1}$ (Fürst et al. 2010). A detailed description of the system can be found in the recent review by Kretschmar et al. (2021).

Some highly magnetized accreting NSs show absorption-like lines in their high-energy X-ray spectra, called cyclotron lines or cyclotron resonant scattering features (CRSFs). They are produced in strong magnetic fields, where electrons are quantized onto Landau levels. Photons with energies close to the Landau levels are removed from the observed X-ray spectrum by scattering off these electrons. CRSFs provide a direct measurement of the magnetic field. The centroid energy of the CRSFs can be expressed as

$$E_{\rm cyc} \approx \frac{n}{(1+z)} 11.6\,[\rm keV]\times B_{12}, \quad (1)$$

where $n$ is the number of Landau levels, $B_{12}$ is the magnetic field strength in units of $10^{12}$ gauss, and $z$ is the gravitational redshift of the line formation region (Staubert et al. 2019).

Based on observations with the High Energy X-ray Experiment (HEXE), Kendziorra et al. (1992) reported the first evidence of CRSFs in Vela X-1: a fundamental line at approximately 25 keV and a first harmonic line near 50 keV. Subsequent studies confirmed the presence of both features, with the fundamental line typically observed at ∼23–27 keV and the harmonic at ∼45–54 keV (Kretschmar et al. 1997; Kreykenbohm et al. 2002; Schanne et al. 2007; Maitra & Paul 2013; Odaka et al. 2013). Notably, the fundamental line is considerably weaker than the harmonic and is not always detectable. Significant variability has been observed with the CRSF in Vela X-1, regarding its centroid energy $E_{\rm cyc}$ and other characteristic parameters (e.g., width and optical depth). These parameters vary with luminosity and with time. Fuerst et al. (2014) detected both CRSFs based on *NuSTAR* observations, and for the first time reported a positive correlation between the energy of the harmonic line ($E_{\rm cyc,H}$) and luminosity, consistent with theoretical predictions in the subcritical accretion regime (Becker et al. 2012). In contrast, the energy of the fundamental line ($E_{\rm cyc,F}$) exhibits a more complex, nonmonotonic dependence on luminosity. This positive $E_{\rm cyc,H}$–luminosity correlation was further confirmed by La Parola et al. (2016) through an analysis of long-term *Swift*/BAT data. In addition, they discovered a secular decline in $E_{\rm cyc,H}$ at a rate of ∼0.36 keV yr$^{-1}$ between 2004 and 2010. This establishes Vela X-1 as the second known source, after Her X-1 (see the summary by Staubert et al. 2020), to exhibit a long-term $E_{\rm cyc}$ decay. Ji et al. (2019) confirmed that the decay persisted until 2012 and reported that $E_{\rm cyc,H}$ remained stable thereafter based on continued *Swift*/BAT monitoring.

Two key questions are whether the long-term decay of $E_{\rm cyc,H}$ in Vela X-1 has truly ended and whether there is any indication of a subsequent increase. However, since the observations were obtained at different luminosity levels, the $E_{\rm cyc}$–luminosity correlation presents a major challenge for disentangling

⋆ Corresponding author: du@astro.uni-tuebingen.de

**Table 1.** Details on *NuSTAR* observations of Vela X-1 between 2012 and 2024.

| ObsID | Obs. Time YYYY-MM-DD | Duration MJD | Exposure s | Period s |
|---|---|---|---|---|
| 10002007001 | 2012-07-09 | 56117.63–56117.94 | 10813 | 283.48 |
| 30002007002 | 2013-04-22 | 56404.53–56404.84 | 7137 | 283.41 |
| 30002007003 | 2013-04-22 | 56404.86–56405.78 | 24496 | 283.42 |
| 90402339002 | 2019-01-10 | 58493.18–58494.09 | 36036 | 283.45 |
| 30501003002 | 2019-05-03 | 58606.87–58608.25 | 40375 | 283.43 |
| 90602328002 | 2020-09-24 | 59116.98–59117.22 | 10728 | 283.53 |
| 90602328004 | 2020-09-26 | 59119.00–59119.22 | 9593 | 283.43 |
| 90602328006 | 2020-09-29 | 59121.68–59121.91 | 8977 | 283.46 |
| 91002349002 | 2024-11-19 | 60633.05–60633.96 | 36930 | 283.57 |

intrinsic long-term evolution of $E_{\rm cyc}$ from its luminosity dependence. Previous studies have addressed this issue by using normalization techniques in Her X-1 (Staubert et al. 2014), and by comparing evolutionary trends across different epochs in Vela X-1 (La Parola et al. 2016). For this work our aim was to address this issue by applying a pulse-to-pulse analysis technique.

For this paper we analyzed *Swift*/BAT monitoring data of Vela X-1 spanning from January 2005 to December 2024; we employed the methodology and software developed by Klochkov et al. (2015) and validated by Ji et al. (2019). Here we present a detailed spectral analysis using nine *NuSTAR* observations conducted between 2012 and 2024. The structure of the paper is as follows. In Section 2, we describe the observations and data reduction procedures. Section 3 presents the results of our analysis. In Sections 4 and 5, we discuss and summarize our results. Additional results are included in the Appendix.

## 2. Observations and data analysis

### 2.1. *Swift*/BAT

In this work, we include publicly available archival data obtained with the Burst Alert Telescope (BAT; Barthelmy et al. 2005), a hard X-ray detector on board the Neil Gehrels *Swift* observatory (Gehrels et al. 2004). The aim of the BAT spectral analysis is to investigate the evolution of the energy of the harmonic cyclotron line. Due to the regular monitoring of the source by BAT, the dataset is nearly uniformly sampled with minimal time gaps. The instrument is sensitive in the energy range of 15–150 keV and is suited for the study of the ∼55 keV harmonic cyclotron line in Vela X-1.

The analysis covers data collected from January 2005 through December 2024, all of which are accessible via HEASARC[1]. The selected data were obtained in survey mode, in which events were collected in the detector plane histograms (DPHs) accumulated over a five-minute exposure time. The data reduction follows the method described by Klochkov et al. (2015) and Ji et al. (2019). The spectra were generated using the `batbinevt` tool from the `HEASoft` v6.34. We extracted the spectra only if the source could be identified in the sky map. The recommended BAT systematic uncertainties were applied using the `batphasyserr` task. Corrections to the BAT energy scale for detector nonlinearities and detector-dependent offsets not accounted for by onboard calibration were performed using the `baterebin` tool.

To enhance the statistics in the spectral analysis, we jointly fitted hundreds of spectra within three-month intervals; the spectral shapes were assumed to be the same, while the normalizations were variable. The validity of this method was previously verified by Klochkov et al. (2015) and Ji et al. (2019).

### 2.2. *NuSTAR*

The Nuclear Spectroscopic Telescope Array (*NuSTAR*) is the first focusing hard X-ray observatory and is equipped with two identical co-aligned X-ray telescopes, Focal Plane Module A and B (FPMA and FPMB; Harrison et al. 2013). The instruments cover a wide energy range of 3–79 keV and provide an imaging resolution of 18″ at full width at half maximum (FWHM) and a spectral energy resolution of 400 eV (FWHM) at 10 keV. In Table 1 we list nine observations of Vela X-1 performed by *NuSTAR* over the time period 2012–2024. We used the NUSTARDAS pipeline v2.1.2 and `HEASoft` v6.33.2 with *NuSTAR* CALDB v20240520. As suggested by Diez et al. (2022), we used the old FPMA ARF[2] for observation 30501003002 to avoid differences between the two focal plane modules, due to an overly low-energy effective area correction. The event times are corrected for barycentric motion using the `barycorr` tool from NUSTARDAS and the binary orbit using the ephemeris from the Fermi GBM website[3]. For each observation, we extracted source spectra from a circular region with a 90 arcsec radius and background spectra from a circular region with a 60 arcsec radius. We performed epoch folding (Leahy 1987) on the extracted light curves to measure the spin period; the results are presented in Table 1.

We wanted to investigate the energy dependence on luminosity across different time intervals to explore the long-term evolution of spectral variability. However, the available data were insufficient to establish a definitive correlation. To address this limitation, we subsequently performed a pulse-to-pulse analysis of the *NuSTAR* observations. This technique, originally introduced by Klochkov et al. (2011), effectively expands the observed luminosity range and provides more detailed insights into spectral evolution. The analysis is described in detail in Section 3.2.2.

Both average and pulse-to-pulse spectra were grouped to ensure a minimum of 30 photons per energy bin. Spectral fitting was performed over the 3–70 keV energy range. All quoted

[1] https://heasarc.gsfc.nasa.gov/docs/archive.html

[2] https://nustarsoc.caltech.edu/NuSTAR_Public/NuSTAROperationSite/mli.php

[3] https://gammaray.nsstc.nasa.gov/gbm/science/pulsars/lightcurves/velax1.html

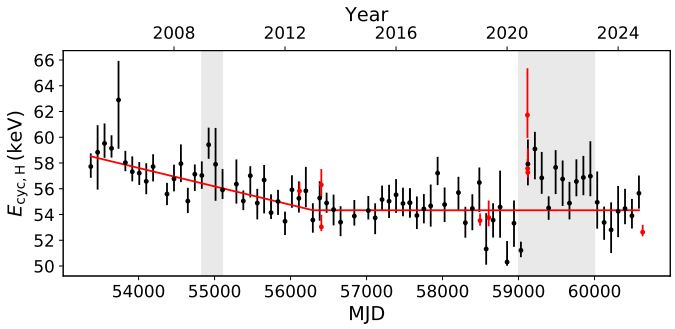


**Fig. 1.** Long-term evolution of the centroid energy of the harmonic cyclotron line in Vela X-1 as observed with *Swift*/BAT. The gray shaded regions indicate epochs of apparent $E_{\rm cyc,H}$ humps and the red points represent the time-averaged results from *NuSTAR* observations in Section 3.2.1.

uncertainties on spectral parameters correspond to the 68% confidence level.

## 3. Results

### 3.1. *Swift*/BAT result

This study includes *Swift*/BAT data spanning from January 2005 to December 2024. The data analysis procedures closely follow those described by Klochkov et al. (2015), La Parola et al. (2016), and Ji et al. (2019). To model the continuum of Vela X-1, we tested different spectral shapes. A simple power law modified with an exponential cutoff (`cutoffpl`) does not fit the data. A `highecut` model, another often-used model for the continuum in accreting neutron stars, is also not adequate to describe the data. We adopted the `comptt` model to describe the continuum, consistent with previous analyses of BAT data (La Parola et al. 2016; Ji et al. 2019). The fundamental line at approximately 25 keV is not detectable by BAT. The combined model, `comptt` × `gabs`, yields a good fit across all spectra. The temperature of the seed photons was fixed at 1 keV during the fitting. The resulting parameters are available in electronic form at the CDS, and the corresponding results are illustrated in Fig. 1. In Figure 1, the black data represents the centroid energy of the harmonic cyclotron line as derived by the BAT data, while the red data represent the time-averaged results from the *NuSTAR* observations discussed in Section 3.2.1. Initially, the line energy exhibited a significant decrease and remained nearly constant thereafter. A pronounced fluctuation occurred between MJD 59000 and MJD 60000 (corresponding to the years 2020–2023). After this period, the energy returned to its pre-fluctuation level. We adopted a broken linear function to model the evolution of $E_{\rm cyc,H}$, following the approach of Ji et al. (2019):

$$E_{\rm cyc,H}(t) = \begin{cases} E_0 + a \times (t - t_0) & t \le t_{\rm crit} \\ {\rm const} = E_0 + a \times (t_{\rm crit} - t_0) & t > t_{\rm crit} \end{cases} \quad (2)$$

Here $E_0$ is the reference energy at fixed epoch $t_0$ = 53371 (MJD), $a$ is the linear slope describing the decreasing trend, and $t_{\rm crit}$ is the break time after which $E_{\rm cyc,H}$ remains constant. The resulting $t_{\rm crit}$ is MJD 56293 ± 264. The decrease rate of $E_{\rm cyc,H}$ is $-0.584 \pm 0.073$ keV yr$^{-1}$. After the break, the $E_{\rm cyc,H}$ remains constant at 54.60 ± 0.83 keV. Over the evolution, two abrupt humps are apparent, occurring around MJD 55000, and between MJD 59000 and MJD 60000.

### 3.2. *NuSTAR* result

#### 3.2.1. The average spectra result

For the *NuSTAR* observations, the Fermi–Dirac cutoff model (FDcut; Tanaka 1986) provides a good fit to the continuum and was also adopted in previous studies (Fuerst et al. 2014; La Parola et al. 2016; Diez et al. 2022). The FDcut model, characterized by the photon index Γ, cutoff energy $E_{\rm cut}$, and folding energy $E_{\rm fold}$, takes the form:

$$F(E) \propto E^{-\Gamma} \left(1 + \exp\left(\frac{E - E_{\rm cut}}{E_{\rm fold}}\right)\right)^{-1} . \quad (3)$$

The two CRSFs are well described with two Gaussian absorption components (`gabs`). In all the spectra, we detect with high significance the fundamental at ∼25 keV and the second harmonic at ∼52–55 keV. We constrained the width of the fundamental line to be half that of the harmonic line, $\sigma_{\rm cyc,F} = 0.5 \times \sigma_{\rm cyc,H}$, following the approach adopted by Fuerst et al. (2014) and Diez et al. (2022). This assumption is motivated by the physical interpretation that harmonic lines originate from resonant scattering between the ground Landau level and higher excited levels (see Equation (1)). Consequently, the energies of the harmonic lines are expected to be twice that of the fundamental line, and their width scale accordingly. We adopted the `tbabs` absorption model, and set the abundances to `wilm` (Wilms et al. 2000). A single-absorption model cannot accurately describe the spectrum at lower energies because of the contribution of the absorption from the stellar wind. Therefore, we added a partial covering model `pcfabs` to take into account the wind structure (Fuerst et al. 2014; Diez et al. 2022). The interstellar absorption component ($N_{\rm H1}$) was fixed at $0.371 \times 10^{22}$ cm$^{-2}$, as determined from NASA's HEASARC $N_{\rm H}$ tool[4]. As *NuSTAR* does not provide coverage below 3 keV, it is not well suited to constraining low absorption values. In contrast, the absorption due to the stellar wind ($N_{\rm H2}$) was left as a free parameter. A Gaussian emission line centered around ∼6.4 keV was added to account for iron fluorescence. In addition, a broad Gaussian component around ∼10 keV was included, as this feature is essential for an adequate spectral fit. Similar features have been reported in previous studies of Vela X-1 (Fuerst et al. 2014; Diez et al. 2022), and in other sources, where they typically appear near the spectral cutoff energy (Nespoli et al. 2012; DeCesar et al. 2013; Nabizadeh et al. 2021). In the case of Vela X-1, this feature has not been interpreted as a CRSF, although its physical origin remains uncertain. To enable joint fitting of the two instruments, a cross-normalization constant was applied. Throughout the analysis, the `cflux` convolution model was used to derive all unabsorbed flux values.

We present the results of ObsID 91002349002 as a representative example; this dataset has not been analyzed in previous studies. Figure 2 shows the broadband spectrum. Panel (c) presents the residuals when the ∼10 keV component is excluded from the model, and Panel (d) presents the residuals when the two CRSFs are excluded. Table 2 summarizes the spectral parameters obtained from the best-fit model for this observation. The model yielded a $\chi^2$ value of 555.27 for 448 degrees of freedom. The best-fit cyclotron line energies were $E_{\rm cyc,F} = 24.55^{+0.48}_{-0.48}$ keV and $E_{\rm cyc,H} = 52.63^{+0.57}_{-0.32}$ keV. This model was subsequently applied to fit the average spectra of all *NuSTAR* observations. The resulting parameters are available in electronic

[4] https://heasarc.gsfc.nasa.gov/cgi-bin/Tools/w3nh/w3nh.pl

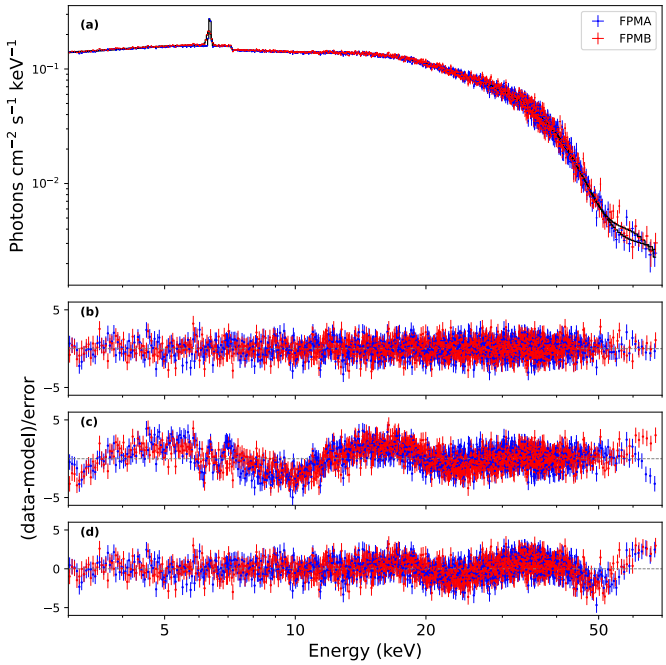


**Fig. 2.** (a) Spectrum and best-fit model for ObsID 91002349002 in energy range 3–70 keV using the model `const×tbabs×pcfabs(gauss+gauss+gabs×gabs×fdcut)`. The FPMA data is in red and the FPMB data in blue. The best-fit model is shown in black. (b) Residuals for the best-fit model. (c) Residuals after fitting without the feature around 10 keV. (d) Residuals after fitting without the CRSFs.

**Table 2.** Best-fit parameters of the phase-averaged spectrum for ObsID 91002349002 using the model `const×tbabs×pcfabs(gauss+gauss+gabs×gabs×fdcut)` in the 3–70 keV energy band.

| Parameter | Value |
|---|---|
| $C_{\rm FPMA}$ (fixed) | 1 |
| $C_{\rm FPMB}$ | $1.0100^{+0.0013}_{-0.0005}$ |
| $N_{\rm H1}$ [$10^{22}$ cm$^{-2}$] (fixed) | 0.371 |
| $N_{\rm H2}$ [$10^{22}$ cm$^{-2}$] | $20.8^{+1.1}_{-0.9}$ |
| CF | $0.30^{+0.01}_{-0.01}$ |
| $E_{10\,\rm keV}$ [keV] | $8.6^{+0.2}_{-0.2}$ |
| $\sigma_{10\,\rm keV}$ [keV] | $3.1^{+0.2}_{-0.2}$ |
| $\rm Norm_{10\,keV}$ | $-0.014^{+0.002}_{-0.003}$ |
| $E_{\rm K\alpha}$ [keV] | $6.341^{+0.005}_{-0.005}$ |
| $\sigma_{\rm K\alpha}$ [keV] | $0.051^{+0.014}_{-0.036}$ |
| $\rm Norm_{K\alpha}$ | $0.00175^{+0.00005}_{-0.00008}$ |
| $E_{\rm cyc,F}$ [keV] | $24.55^{+0.48}_{-0.48}$ |
| $\sigma_{\rm cyc,F}$ [keV] | $0.5 \times \sigma_{\rm cyc,H}$ |
| $d_{\rm cyc,F}$ | $0.46^{+0.14}_{-0.07}$ |
| $E_{\rm cyc,H}$ [keV] | $52.63^{+0.57}_{-0.32}$ |
| $\sigma_{\rm cyc,H}$ [keV] | $7.24^{+0.64}_{-0.38}$ |
| $d_{\rm cyc,H}$ | $14.98^{+2.52}_{-1.44}$ |
| $E_{\rm cut}$ [keV] | $22.2^{+0.9}_{-1.3}$ |
| $E_{\rm fold}$ [keV] | $10.8^{+0.4}_{-0.2}$ |
| $\Gamma$ | $1.08^{+0.01}_{-0.02}$ |
| $\rm Norm_{\Gamma}$ | $0.267^{+0.008}_{-0.005}$ |
| $\rm Flux_{3-79\,keV}$ | $6.592^{+0.014}_{-0.014}$ |
| $\chi^2$/d.o.f. | 555.27/448 |

**Notes.** All reported errors are at the 68% confidence level and based on the MCMC chain values. Normalization of the power law in units of photon cm$^{-2}$ s$^{-1}$ keV$^{-1}$ at 1 keV. Unabsorbed flux (in units of $10^{-9}$ erg cm$^{-2}$ s$^{-1}$) calculated for the entire model, obtained using the `cflux` command from XSPEC. Uncertainties are given for a 68% confidence level.

form at the CDS. Figure 3 shows the best-fit spectral parameters, including the energy and strength of the fundamental line; the energy, width, and strength of the harmonic line; and the continuum parameters, as functions of the intrinsic source luminosity (3–70 keV) assuming a distance of 1.9 kpc. Since the measured cyclotron line energies can be affected by the continuum shape and the line widths, we also constructed corner plot of the distribution for all the parameters (see Figure A.1 in the Appendix).

The luminosity range derived from the time-averaged spectral analysis is approximately (0.2–0.8) $\times$ $10^{37}$ erg s$^{-1}$. We observed a sudden drop in $E_{\rm cut}$ at around $0.3 \times 10^{37}$ erg s$^{-1}$. For the three corresponding observations, we fixed $E_{\rm cut}$ at 20 keV. This adjustment has no significant impact on the parameters of either the harmonic or the fundamental cyclotron lines. The observed drop is likely due to relatively low statistics in these spectra. No clear trend is observed in the evolution of $E_{\rm cyc,F}$ with luminosity; the values range from a minimum of $23.41^{+0.86}_{-0.14}$ keV to a maximum of $25.94^{+1.25}_{-0.97}$ keV. Similarly, no obvious correlation between $E_{\rm cyc,H}$ and luminosity can be established based on the nine averaged measurements. The three 2020 observations show relatively high values of $E_{\rm cyc,H}$, reaching $61.72^{+3.64}_{-1.78}$ keV (ObsID 90602328002), $57.57^{+0.73}_{-0.45}$ keV (ObsID 90602328004), and $57.27^{+1.86}_{-0.40}$ keV (ObsID 90602328006), consistent with the increase in the line energy observed with the *Swift*/BAT monitoring since 2020. To more accurately trace the evolution of the line energy, we employed a pulse-to-pulse analysis technique.

### 3.2.2. The pulse-to-pulse analysis

Following the method introduced by Klochkov et al. (2011), we generated pulse amplitude-resolved spectra based on the pulse-to-pulse technique. This approach was applied to explore the luminosity dependence of the CRSF energy in Cep X–4 and V 0332+53 using *NuSTAR* data (Vybornov et al. 2017, 2018), and in 1A 0535+262 with *Insight*-HXMT data (Shui et al. 2024). The pulse-to-pulse technique is based on the fact that most accreting pulsars exhibit strong pulse-to-pulse variations in amplitude that are driven by short-term fluctuations in the accretion rate. By selecting individual pulses with similar amplitudes and grouping them to generate spectra, this method extends the accessible luminosity range and improves statistics. Therefore, it enables a more detailed investigation of the luminosity dependence of the CRSF energy.

The pulse amplitude is defined as the total number of counts summed over a single pulse. Due to limited photon statistics, extracting meaningful spectra from individual pulses is not feasible. Therefore, pulses with similar amplitudes were grouped together. We explored the distribution of pulse amplitudes and divided the entire range of amplitudes into several bins, thus ensuring approximately equal statistics within each bin. The number of bins was primarily determined by the available counting statistics for the energy spectra, which needed to be sufficient to constrain the cyclotron line energy during spectral fitting. For each bin a list of good time intervals (GTIs) was generated to select pulses within the corresponding amplitude range. Using

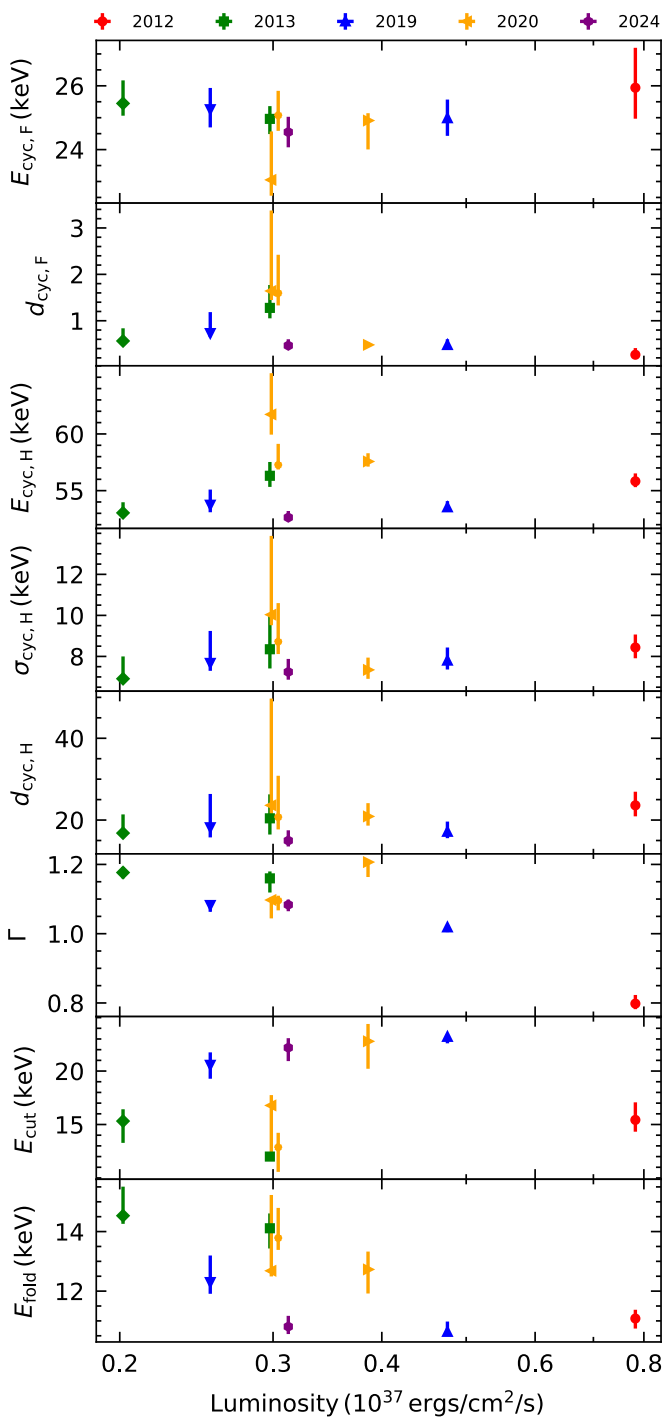


**Fig. 3.** Flux-resolved spectral parameters derived from nine *NuSTAR* observations in the 3–70 keV energy range, shown as a function of intrinsic source luminosity. From top to bottom: Energy of the fundamental line, energy of the harmonic line, width of the harmonic line, strength of the harmonic line, photon index, cutoff energy, and folding energy.

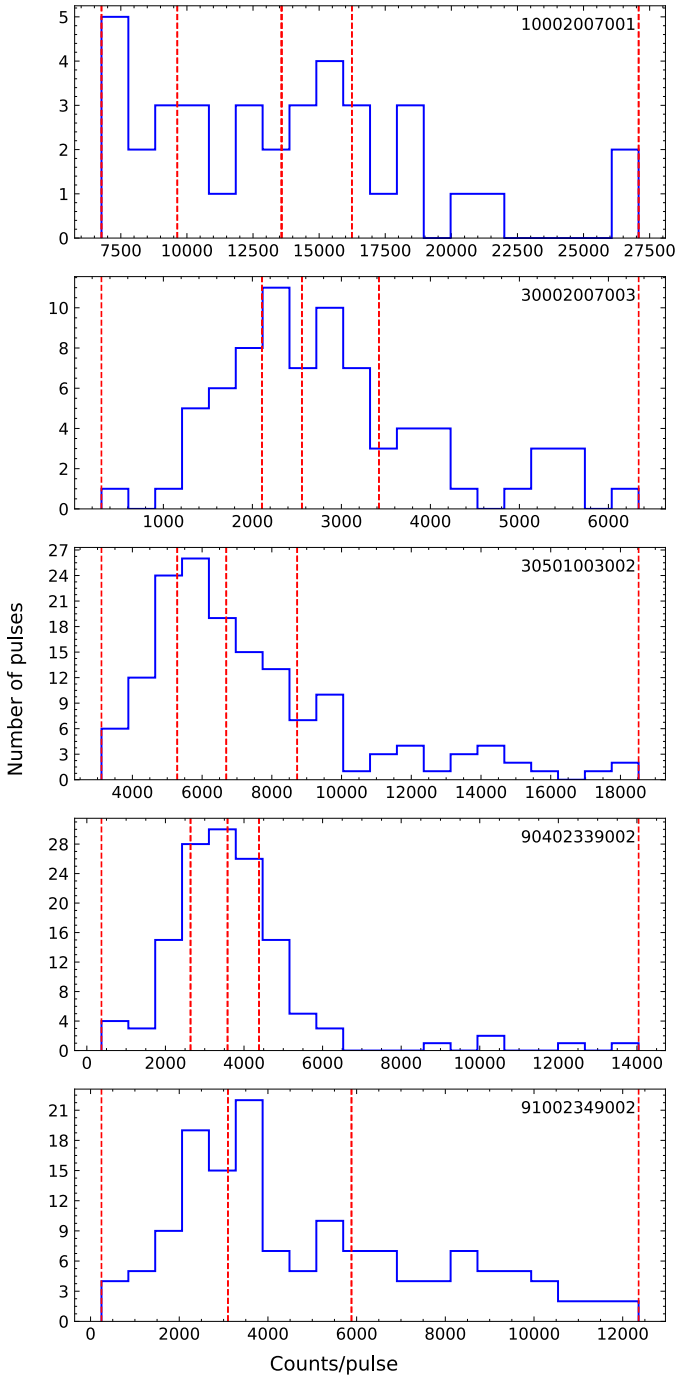


**Fig. 4.** Distributions of counts per individual pulse (i.e. of pulse amplitudes). The red dashed lines indicate the boundaries of the amplitude bins used for extracting pulse-to-pulse spectra. In each distribution, the total number of counts is evenly distributed among the bins.

these GTIs, we extracted the broadband spectra for each amplitude bin.

Using the pulse-to-pulse method, we divided ObsIDs 10002007001, 30002007003, 90402339002, 30501003002, and 91002349002 into 4, 4, 4, 4, and 3 amplitude bins, respectively. The distributions of counts per individual pulse are shown in Figure 4. The distributions reveal that pulse amplitudes within a single observation cover a dynamic range of several times, indicating a strong intrinsic pulse-to-pulse variability of the source. For ObsIDs 30002007002, 90602328002, 90602328004, and 90602328006, due to limited exposure time, we retained only the time-averaged spectral results. For the spectral analysis, we employed the same model as used in the time-averaged analysis: `const×tbabs×pcfabs(gauss+gauss+gabs×gabs×fdcut)`. Given the shorter exposure time per pulse-to-pulse spectrum, we had to fix some parameters to their respective time-averaged

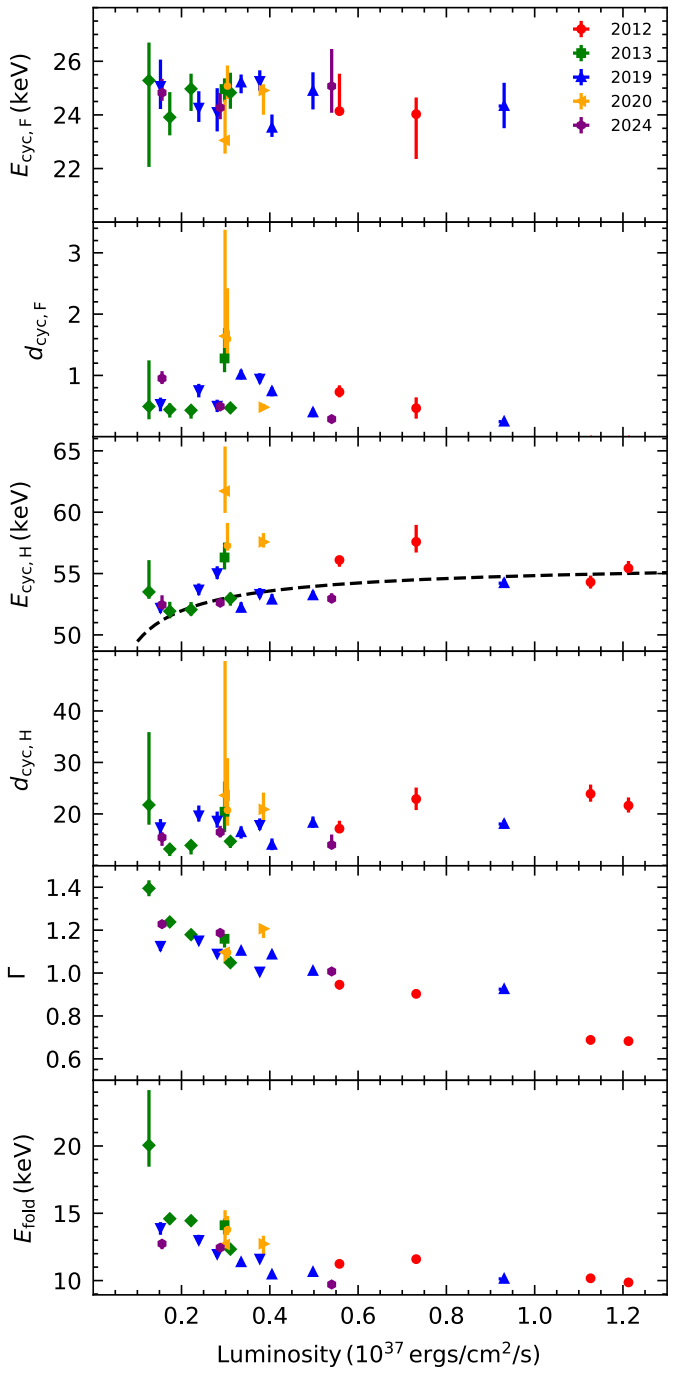


**Fig. 5.** Flux-resolved spectral parameters derived from the pulse-to-pulse analysis in the 3–70 keV energy range. Different colors represent different observation years, and distinct marker styles indicate observation IDs; time-averaged results for the short-exposure observations (30002007002, 90602328002, 90602328004, and 90602328006) are also shown. The dashed line in the second panel is the theoretical prediction for $E_* = 28.097 \pm 0.052$ keV (see Equation (4)).

values to achieve a good fit. We fixed the width of the iron line, $\sigma_{\rm K\alpha}$; the energy and the width of the 10 keV line, $E_{\rm 10\,keV}$ and $\sigma_{\rm 10\,keV}$; and the width of the two CRSFs, $\sigma_{\rm cyc,F}$ and $\sigma_{\rm cyc,H}$, to their respective time-averaged values. We initially attempted to leave $\sigma_{\rm cyc,H}$ and $E_{\rm cut}$ free. However, this approach resulted in poor constraints on $E_{\rm cut}$. The continuum parameter $E_{\rm cut}$ was therefore fixed because of its degeneracy with the fundamental line energy $E_{\rm cyc,F}$. With the adopted strategy of fixing the above parameters, we obtained very good fits for all spectra. The corresponding best-fit parameters are provided in the tables available at the CDS.

Figure 5 presents the spectral results obtained from the pulse-to-pulse analysis. The plot also includes the time-averaged results for the short-exposure observations 30002007002, 90602328002, 90602328004, and 90602328006. Our analysis extends the explored luminosity range to $(0.13-1.21) \times 10^{37}$ erg s$^{-1}$ and successfully disentangles the intrinsic long-term evolution of $E_{\rm cyc}$ from its luminosity dependence.

The fundamental line energy, $E_{\rm cyc,F}$, exhibits no significant variation with time or luminosity, remaining stable at approximately 25 keV. At higher luminosities ($L_{\rm X} \gtrsim 10^{37}$ erg s$^{-1}$), the spectra can be well fit without requiring an additional component for the fundamental line. Therefore, we do not include these two data points in the plot, as they are not meaningful when the corresponding spectral component is not necessary for the fit. To improve the statistics, we split this observation into two bins, with only one data point in the high-luminosity bin. The fit remains acceptable without the fundamental line. When included, we derived a $3\sigma$ upper limit on its strength of ~0.8, suggesting that the line may be present but undetectable due to limited sensitivity.

For the energy of harmonic line, $E_{\rm cyc,H}$, excluding the 2020 observations, the data appear fairly stable, with slightly lower values at lower luminosities. Moreover, at comparable luminosity levels, there is no time dependence of the $E_{\rm cyc,H}$ across different epochs, suggesting that the long-term decay of $E_{\rm cyc,H}$ likely ceased after 2012. Additionally, the photon index exhibits a negative correlation with luminosity, indicating a hardening of the continuum spectrum at higher flux levels.

## 4. Discussion

In this work, we investigate the dependence of the fundamental cyclotron line energy ($E_{\rm cyc,F}$) and the harmonic line energy ($E_{\rm cyc,H}$) on both time and X-ray luminosity ($L_{\rm X}$). By performing a time-averaged analysis of archival *Swift*/BAT monitoring data, we investigated the long-term evolution of $E_{\rm cyc,H}$ over 20 years. Using observations from *NuSTAR* we performed the pulse-to-pulse analysis to reveal the comprehensive scenario of the $E_{\rm cyc}$–$L_{\rm X}$ relation covering a luminosity range of $0.13 \times 10^{37}$ erg s$^{-1}$ to $1.21 \times 10^{37}$ erg s$^{-1}$.

### 4.1. Changes in $E_{\rm cyc}$ with time

To date, only two sources, Her X-1 and Vela X-1, have shown clear long-term variability in $E_{\rm cyc}$ over timescales of tens of years (Staubert et al. 2020; La Parola et al. 2016; Ji et al. 2019). In Her X-1 the long-term decay of $E_{\rm cyc}$ ended around 2012, stabilizing at approximately 37 keV, with a decline rate of ~0.26 keV yr$^{-1}$ between 1996 and 2012 (Staubert et al. 2020). For Vela X-1 our analysis confirms the previously reported decrease in the energy of the first cyclotron harmonic (La Parola et al. 2016; Ji et al. 2019), which now appears to remain constant. The decrease rate is ~0.36 keV yr$^{-1}$ and ~0.51 keV yr$^{-1}$ stated by La Parola et al. (2016) and Ji et al. (2019), similar to our result ~0.58 keV yr$^{-1}$ based on BAT observations.

The long-term decay of $E_{\rm cyc,H}$ in Vela X-1 is likely a local effect at the magnetic polar cap, rather than a change in the global dipole field. Similar scenarios have been proposed for Her

X-1 (Staubert et al. 2014, 2016, 2020). They suggested that the decay could be connected to a geometric displacement of the emission region in the dipole field or it could be related to the accreted matter that accumulates into a magnetically supported mound and causes a change in the magnetic field configuration at the polar cap. The end of the decay could be explained by the mound reaching its maximum stable size beyond which further accumulation no longer significantly affects the field structure.

In addition, we observed a sudden increase in the harmonic cyclotron line energy, reaching ~62 keV in 2020, with *NuSTAR* observations, followed by a decrease back to ~52 keV in 2024 at comparable luminosity levels of $\sim 0.3 \times 10^{36}$ erg s$^{-1}$. Such a dramatic evolution in the cyclotron line energy is unusual. This result is supported by *Swift*/BAT monitoring, which shows a significant increase in $E_{\rm cyc,H}$ between 2020 and 2023 (MJD 59000–60000). A similar hump around MJD 55000 was also detected in the *Swift*/BAT data and was reported by Ji et al. (2019). A comparable phenomenon was observed in Her X-1, where the line energy remained constant prior to 1991 and then increased to ~41 keV between 1990 and 1995 (Gruber et al. 1999; dal Fiume et al. 1998), followed by a more gradual, linear decay. This process may be cyclic (Staubert et al. 2017).

We present here a possible explanation for the sudden increase. Matter accumulation at the magnetic poles increases the overpressure until a critical threshold is reached. This triggers interchange instabilities (e.g., ballooning instabilities Litwin et al. 2001) near the column boundary, causing localized magnetic field deformation and mass leakage. As a result, $E_{\rm cyc,H}$ increases because of partial column collapse, and a reduction in height. The fact that only $E_{\rm cyc,H}$ exhibits this strong variability, while the $E_{\rm cyc,F}$ remains nearly constant, may suggest that the harmonic line is more sensitive to changes in the height of the emission region.

It is worth noting that previous studies have shown that sudden changes in cyclotron line energy generally occur during the declining phase of long-term evolution. In contrast, this work is the first to reveal that such abrupt shifts can also arise when the cyclotron line has entered a relatively stable, long-term plateau. This finding suggests that even when the polar-cap accretion structure appears to have reached a steady state, localized regions may still experience dynamic or structural changes. At present, no comprehensive theoretical framework can fully explain this behavior, but extensive future observations of Vela X-1 and other source (e.g. Her X-1, Cen X-3, 4U 1538-522) could provide critical constraints for refining models of polar-cap dynamics and magnetic-field evolution.

### 4.2. Changes in $E_{\rm cyc}$ with luminosity

The variation in $E_{\rm cyc}$ with luminosity has long been a key focus in the study of accreting X-ray pulsars because it directly reflects the strength of the local magnetic field. Previous observations suggest that cyclotron lines exhibit two distinct evolutionary trends depending on luminosity. A positive dependence of $E_{\rm cyc}$ on $L_{\rm X}$ was observed in low- to moderate-luminosity sources, such as Her X-1 (Staubert et al. 2007, 2014, 2016, 2017, 2020), Vela X-1 (Fuerst et al. 2014; La Parola et al. 2016; Diez et al. 2022), and Cep X-4 (Vybornov et al. 2017). A negative dependence of $E_{\rm cyc}$ on $L_{\rm X}$ was observed in relatively high-luminosity sources, such as V 0332+53 (Tsygankov et al. 2006; Cusumano et al. 2016; Doroshenko et al. 2017; Vybornov et al. 2018) and 1A 0535+262 (Kong et al. 2021). The luminosity at which these different evolutionary behaviors of $E_{\rm cyc}$ occur is often referred to as the critical luminosity ($L_{\rm crit}$) of the source, typically a few times $10^{37}$ erg s$^{-1}$. The $L_{\rm crit}$ separates the accretion regimes into sub-critical and super-critical states. In general, sub-critical accretion is associated with a positive $E_{\rm cyc}$–$L_{\rm X}$ correlation, while super-critical accretion corresponds to a negative correlation (Becker et al. 2012; Mushtukov et al. 2015a). The contrasting $E_{\rm cyc}$–$L_{\rm X}$ behaviors at sub-critical and super-critical luminosities can be interpreted within different theoretical models. An interpretation for the observed $E_{\rm cyc}$–$L_{\rm X}$ correlation relies on the relationship between the $E_{\rm cyc}$ and the height of the emission region above the NS surface (Becker et al. 2012). In low- to moderate-luminosity sources, including Vela X-1, the accreting material is primarily decelerated via Coulomb braking. As the accretion rate increases, the emission region is pushed closer to the NS surface, where the magnetic field is stronger, leading to an increase in $E_{\rm cyc}$. Mushtukov et al. (2015b) proposed that the positive correlation observed in sub-critical sources arises from Doppler shifts in the infalling plasma. In this model, CRSFs are formed as radiation from the polar-cap hotspot travels upward through the accretion column and interacts with the plasma at resonant energies. As luminosity increases, radiation pressure slows the plasma, thus reducing the Doppler redshift and causing the observed line energy to rise.

In our study we first focused on the harmonic cyclotron line energy, $E_{\rm cyc,H}$. Using two *NuSTAR* observations from 2012 and 2013, Fuerst et al. (2014) reported a positive correlation between $E_{\rm cyc,H}$ and luminosity. However, Diez et al. (2022), based on two *NuSTAR* observations from 2019, were unable to confirm this correlation. According to our results, the data remain relatively stable, exhibiting modestly reduced values at lower luminosities. Theoretical predictions for the $E_{\rm cyc}$–$L_{\rm X}$ relationship can be derived from Equations (51) and (58) of Becker et al. (2012):

$$E_{\rm theo} = \left[1 + 0.6\left(\frac{R_*}{10\,\mathrm{km}}\right)^{-\frac{13}{14}}\left(\frac{\Lambda}{0.1}\right)^{-1}\left(\frac{\tau_*}{20}\right)\times\left(\frac{M_*}{1.4\,M_\odot}\right)^{\frac{19}{14}}\left(\frac{E_*}{1\,\mathrm{keV}}\right)^{-\frac{4}{7}}\left(\frac{L_x}{10^{37}\,\mathrm{erg\,s^{-1}}}\right)^{-\frac{5}{7}}\right]^{-3}\times E_*. \quad (4)$$

Here $\tau_*$ is the Thomson optical depth, around 20 for typical HMXB parameters (Becker et al. 2012), and $E_*$ is the energy of the fundamental cyclotron line at the NS surface. We adopt the values $\Lambda = 1$, $R_* = 10$ km and $M_* = 1.8\,M_\odot$. Fitting the data using Equation (4) and excluding the anomalously high values from 2020 yields $E_* = 28.097 \pm 0.052$ keV, assuming a harmonic ratio of 2. The Pearson correlation coefficient is 0.462, with a $p$-value of 0.0405.

However, the fundamental line shows a different behavior as a function of luminosity. A possible anti-correlation up to $7 \times 10^{36}$ erg s$^{-1}$ was reported by Fuerst et al. (2014), beyond which the correlation seems to flatten. This result is obtained from the fitting of data from each orbit, with relatively short exposure times, which leads to large error bars. In our pulse-to-pulse analysis, we considered both the spectra with similar pulse amplitudes and those with longer exposures. As a result, our findings provide better constraints on the fundamental cyclotron line and confirm that its energy shows a flat evolutionary trend with luminosity. The lack of a clear luminosity dependence in the fundamental CRSF energy can be explained by the photon spawning effect (Schönherr et al. 2007). In this scenario, resonant scattering events produce additional low-energy photons that preferentially populate the energy range of the fundamental line, effectively filling in the absorption feature and diminishing its depth. As a result, the fundamental line becomes less sensitive to luminosity. Furthermore, based on Harding & Daugherty

(1991), the cross section of CRSF at the fundamental and the harmonic is different, which is related to the angle between the photon momentum and the magnetic field. In the subcritical regime, photons can escape from the top of the accretion column along the magnetic field lines (called pencil-beam geometry), where the cross section of the harmonic line is much lower than that of the fundamental, making it intrinsically weaker. However, when the infalling material reaches relativistic speeds, the resulting beaming effect can increase the effective viewing angle and enhance the cross section of the harmonic line. Such conditions may arise near the shock region of the accretion column, leading to a locally stronger harmonic feature (see discussion in Kong et al. 2022).

To further investigate the accretion regime of Vela X-1, we calculated the $L_{\rm crit}$ under different theoretical models. The expression for the $L_{\rm crit}$ as a function of the magnetic field strength at the neutron star (NS) surface, following Becker et al. (2012), is given by:

$$L_{\rm crit} = 1.49\times10^{37}\,{\rm erg\,s^{-1}}\left(\frac{\Lambda}{0.1}\right)^{-7/5} w^{-28/15} \times\left(\frac{M_*}{1.4\,M_\odot}\right)^{29/30}\left(\frac{R_*}{10\,{\rm km}}\right)^{1/10}\left(\frac{B_*}{10^{12}\,{\rm G}}\right)^{16/15}, \quad (5)$$

where $R_*$ is the radius of the NS, $M_*$ is the mass of the NS, $B_*$ is the magnetic field strength at the NS surface, $\Lambda$ is a constant that depends on the accretion flow geometry, and $w$ is a parameter describing the spectral shape inside the column. We adopt $R_* = 10\,{\rm km}$ and $M_* = 1.8\,M_\odot$ (Rawls et al. 2011), and assume $w = 1$, corresponding to a Bremsstrahlung-dominated emission spectrum inside the column. Accretion flow geometry is a source of principal uncertainties. If we take $\Lambda = 1$, appropriate for spherical or wind-fed accretion, and combine Equation (5) with Equation (1), assuming a surface fundamental cyclotron line energy of $E_{\rm cyc,F} = 25\,{\rm keV}$, we obtain $L_{\rm crit} \sim 0.17\times10^{37}\,{\rm erg\,s^{-1}}$. If we adopt $\Lambda = 0.1$, which corresponds to disc accretion, yields $L_{\rm crit} \sim 4.31\times10^{37}\,{\rm erg\,s^{-1}}$. These two scenarios represent limiting cases. In reality, the accretion flow may involve a combination of both modes, suggesting that the actual $L_{\rm crit}$ lies between these two limits.

Mushtukov et al. (2015a) provided a numerical solution by calculating the luminosity for two scenarios: one with purely extraordinary polarization and another with an equal mix of ordinary and extraordinary polarization. The real critical luminosity value is expected to fall between the two cases. In their prediction, assuming $E_{\rm cyc} = 25\,{\rm keV}$, the estimated $L_{\rm crit}$ for Vela X-1 is in the range of $\sim0.3 - 1.0\times10^{37}\,{\rm erg\,s^{-1}}$ (as shown in Fig. 7 of that study).

We observe a clear spectral hardening with increasing luminosity. In many accreting pulsars, the photon index $\Gamma$ exhibits a luminosity dependence similar to that of the $E_{\rm cyc}$: it decreases with increasing luminosity in high-luminosity sources (i.e., the spectrum softens), and increases with luminosity in low- to moderate-luminosity sources (i.e., the spectrum hardens) (Klochkov et al. 2011; Reig & Nespoli 2013). In the case of Vela X-1, this behavior can be interpreted as a result of the emission region moving closer to the neutron star surface at higher luminosities. As the sinking region becomes more compact, the optical depth increases, leading to enhanced Comptonization and the production of harder photons, thereby yielding a harder spectrum (Becker et al. 2012; Reig & Nespoli 2013). According to the model proposed by Postnov et al. (2015), at low luminosities the emerging X-ray spectrum is produced by ordinary photons in a magnetized optically thin slab-like atmosphere near the polar cap. As the accretion rate increases, the Comptonization rises, thus leading to a harder X-ray continuum.

## 5. Conclusions

We conducted a detailed study of the long-term evolution and the luminosity dependence of the cyclotron line energy in Vela X-1, based on archival *Swift*/BAT monitoring and nine *NuSTAR* observations from 2012 to 2024.

This work presented the first confirmation that the long-term decay of the harmonic line energy in Vela X-1 has ended. Moreover, we report the first detection of a renewed increase in $E_{\rm cyc,H}$ between 2020 and 2023. Such dramatic variability, which occurred after the line energy had settled into a relatively stable plateau, is unusual and likely reflects sudden magnetic or structural changes in the accretion environment. Continued long-term monitoring of Vela X-1 and other sources will be essential to determine whether this behavior is part of a broader cyclic phenomenon.

Using pulse-to-pulse analysis, we find that the fundamental line energy remains stable over both time and luminosity, showing no significant evolution. The harmonic line energy is found to be slightly lower at low luminosities and to flatten at higher luminosities.

## Data availability

The tables related to the *Swift*/BAT spectral parameters, the *NuSTAR* averaged spectral parameters, and the *NuSTAR* pulse-to-pulse spectral parameters for individual observations are available at the CDS via https://cdsarc.cds.unistra.fr/viz-bin/cat/J/A+A/vol/page

*Acknowledgements.* This work made use of data from the *NuSTAR* mission, a project led by the California Institute of Technology, and also benefited from the long-term support of the Burst Alert Telescope on board the Neil Gehrels *Swift* observatory. Y.J. Du would like to thank the support from China Scholarship Council (CSC 202108080247). P. J. Wang is grateful for the financial support provided by the Sino-German (CSC-DAAD) Postdoc Scholarship Program (57678375). L. Ji is supported by the National Natural Science Foundation of China under grant No. 12173103. LD acknowledges funding from the Deutsche Forschungsgemeinschaft (DFG, German Research Foundation) – Projektnummer 549824807.

## References

Barthelmy, S. D., Barbier, L. M., Cummings, J. R., et al. 2005, Space Sci. Rev., 120, 143
Becker, P. A., Klochkov, D., Schönherr, G., et al. 2012, A&A, 544, A123
Chodil, G., Mark, H., Rodrigues, R., Seward, F. D., & Swift, C. D. 1967, ApJ, 150, 57
Cusumano, G., La Parola, V., D'Aì, A., et al. 2016, MNRAS, 460, L99
dal Fiume, D., Orlandini, M., Cusumano, G., et al. 1998, A&A, 329, L41
DeCesar, M. E., Boyd, P. T., Pottschmidt, K., et al. 2013, ApJ, 762, 61
Diez, C. M., Grinberg, V., Fürst, F., et al. 2022, A&A, 660, A19
Doroshenko, V., Tsygankov, S. S., Mushtukov, A. A., et al. 2017, MNRAS, 466, 2143
Fuerst, F., Pottschmidt, K., Wilms, J., et al. 2014, American Astronomical Society Meeting Abstracts, 223, 438.20
Fürst, F., Kreykenbohm, I., Pottschmidt, K., et al. 2010, A&A, 519, A37
Gehrels, N., Chincarini, G., Giommi, P., et al. 2004, ApJ, 611, 1005
Gruber, D. E., Heindl, W. A., Rothschild, R. E., et al. 1999, in Highlights in X-ray Astronomy, eds. B. Aschenbach, & M. J. Freyberg, 272, 33
Harding, A. K., & Daugherty, J. K. 1991, ApJ, 374, 687
Harrison, F. A., Craig, W. W., Christensen, F. E., et al. 2013, ApJ, 770, 103
Hiltner, W. A., Werner, J., & Osmer, P. 1972, ApJ, 175, L19
Ji, L., Staubert, R., Ducci, L., et al. 2019, MNRAS, 484, 3797

Kendziorra, E., Mony, B., Kretschmar, P., et al. 1992, in Frontiers Science Series, eds. Y. Tanaka, & K. Koyama, 51

Klochkov, D., Staubert, R., Santangelo, A., Rothschild, R. E., & Ferrigno, C. 2011, A&A, 532, A126

Klochkov, D., Staubert, R., Postnov, K., et al. 2015, A&A, 578, A88

Kong, L. D., Zhang, S., Ji, L., et al. 2021, ApJ, 917, L38

Kong, L.-D., Zhang, S., Ji, L., et al. 2022, ApJ, 932, 106

Kretschmar, P., Pan, H. C., Kendziorra, E., et al. 1997, A&A, 325, 623

Kretschmar, P., El Mellah, I., Martínez-Núñez, S., et al. 2021, A&A, 652, A95

Kreykenbohm, I., Coburn, W., Wilms, J., et al. 2002, A&A, 395, 129

La Parola, V., Cusumano, G., Segreto, A., & D'Aì, A. 2016, MNRAS, 463, 185

Leahy, D. A. 1987, A&A, 180, 275

Litwin, C., Brown, E. F., & Rosner, R. 2001, ApJ, 553, 788

Maitra, C., & Paul, B. 2013, ApJ, 763, 79

Mushtukov, A. A., Suleimanov, V. F., Tsygankov, S. S., & Poutanen, J. 2015a, MNRAS, 447, 1847

Mushtukov, A. A., Tsygankov, S. S., Serber, A. V., Suleimanov, V. F., & Poutanen, J. 2015b, MNRAS, 454, 2714

Nabizadeh, A., Tsygankov, S. S., Ji, L., et al. 2021, A&A, 652, A89

Nespoli, E., Reig, P., & Zezas, A. 2012, A&A, 547, A103

Odaka, H., Khangulyan, D., Tanaka, Y. T., et al. 2013, ApJ, 767, 70

Postnov, K. A., Gornostaev, M. I., Klochkov, D., et al. 2015, MNRAS, 452, 1601

Rawls, M. L., Orosz, J. A., McClintock, J. E., et al. 2011, ApJ, 730, 25

Reig, P., & Nespoli, E. 2013, A&A, 551, A1

Sadakane, K., Hirata, R., Jugaku, J., et al. 1985, ApJ, 288, 284

Schanne, S., Götz, D., Gérard, L., et al. 2007, in The Obscured Universe. Proceedings of the VI Integral Workshop, ESA SP, 622, 479

Schönherr, G., Wilms, J., Kretschmar, P., et al. 2007, A&A, 472, 353

Shui, Q. C., Zhang, S., Wang, P. J., et al. 2024, MNRAS, 528, 7320

Staubert, R., Shakura, N. I., Postnov, K., et al. 2007, A&A, 465, L25

Staubert, R., Klochkov, D., Wilms, J., et al. 2014, A&A, 572, A119

Staubert, R., Klochkov, D., Vybornov, V., Wilms, J., & Harrison, F. A. 2016, A&A, 590, A91

Staubert, R., Klochkov, D., Fürst, F., et al. 2017, A&A, 606, L13

Staubert, R., Trümper, J., Kendziorra, E., et al. 2019, A&A, 622, A61

Staubert, R., Ducci, L., Ji, L., et al. 2020, A&A, 642, A196

Tanaka, Y. 1986, in IAU Colloquium 89: Radiation Hydrodynamics in Stars and Compact Objects, eds. D. Mihalas, & K.-H. A. Winkler, 255, 198

Tsygankov, S. S., Lutovinov, A. A., Churazov, E. M., & Sunyaev, R. A. 2006, MNRAS, 371, 19

Vybornov, V., Klochkov, D., Gornostaev, M., et al. 2017, A&A, 601, A126

Vybornov, V., Doroshenko, V., Staubert, R., & Santangelo, A. 2018, A&A, 610, A88

Wilms, J., Allen, A., & McCray, R. 2000, ApJ, 542, 914

## Appendix A: Additional figure

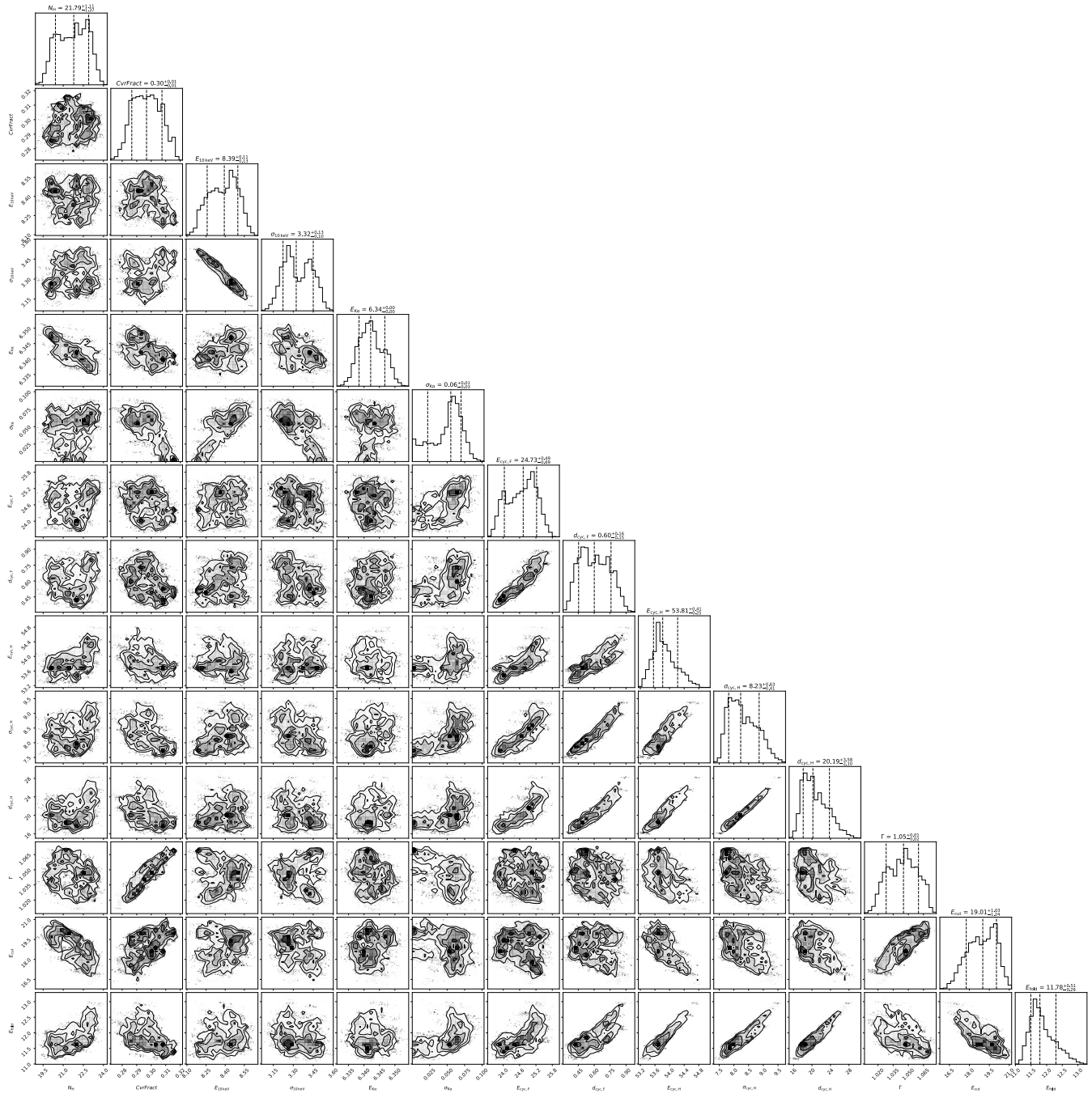

**Fig. A.1.** Corner plot of the posterior distributions of all model parameters for ObsID 91002349002.

A&A 675, A29 (2023)
https://doi.org/10.1051/0004-6361/202346581


Astronomy & Astrophysics

# A polarimetrically oriented X-ray stare at the accreting pulsar EXO 2030+375

Christian Malacaria[1], Jeremy Heyl[2], Victor Doroshenko[3], Sergey S. Tsygankov[4], Juri Poutanen[4], Sofia V. Forsblom[4], Fiamma Capitanio[5], Alessandro Di Marco[5], Yujia Du[3], Lorenzo Ducci[3,6], Fabio La Monaca[5], Alexander A. Lutovinov[7], Herman L. Marshall[8], Ilya A. Mereminskiy[7], Sergey V. Molkov[7], Alexander A. Mushtukov[9], Mason Ng[8], Pierre-Olivier Petrucci[10], Andrea Santangelo[3], Andrey E. Shtykovsky[7], Valery F. Suleimanov[3], Iván Agudo[11], Lucio A. Antonelli[12,13], Matteo Bachetti[14], Luca Baldini[15,16], Wayne H. Baumgartner[17], Ronaldo Bellazzini[15], Stefano Bianchi[18], Stephen D. Bongiorno[17], Raffaella Bonino[19,20], Alessandro Brez[15], Niccolò Bucciantini[21,22,23], Simone Castellano[15], Elisabetta Cavazzuti[24], Chien-Ting Chen[25], Stefano Ciprini[26,13], Enrico Costa[5], Alessandra De Rosa[5], Ettore Del Monte[5], Laura Di Gesu[24], Niccolò Di Lalla[27], Immacolata Donnarumma[24], Michal Dovčiak[28], Steven R. Ehlert[17], Teruaki Enoto[29], Yuri Evangelista[5], Sergio Fabiani[5], Riccardo Ferrazzoli[5], Javier A. Garcia[30], Shuichi Gunji[31], Kiyoshi Hayashida[32,†], Wataru Iwakiri[33], Svetlana G. Jorstad[34,35], Philip Kaaret[17], Vladimir Karas[28], Fabian Kislat[36], Takao Kitaguchi[29], Jeffery J. Kolodziejczak[17], Henric Krawczynski[37], Luca Latronico[19], Ioannis Liodakis[38], Simone Maldera[19], Alberto Manfreda[39], Frédéric Marin[40], Andrea Marinucci[24], Alan P. Marscher[34], Francesco Massaro[19,20], Giorgio Matt[18], Ikuyuki Mitsuishi[41], Tsunefumi Mizuno[42], Fabio Muleri[5], Michela Negro[43,44,45], Chi-Yung Ng[46], Stephen L. O'Dell[17], Nicola Omodei[27], Chiara Oppedisano[19], Alessandro Papitto[12], George G. Pavlov[47], Abel L. Peirson[27], Matteo Perri[13,12], Melissa Pesce-Rollins[15], Maura Pilia[14], Andrea Possenti[14], Simonetta Puccetti[13], Brian D. Ramsey[17], John Rankin[5], Ajay Ratheesh[5], Oliver J. Roberts[25], Roger W. Romani[27], Carmelo Sgrò[15], Patrick Slane[48], Paolo Soffitta[5], Gloria Spandre[15], Douglas A. Swartz[25], Toru Tamagawa[29], Fabrizio Tavecchio[49], Roberto Taverna[50], Yuzuru Tawara[26], Allyn F. Tennant[17], Nicholas E. Thomas[17], Francesco Tombesi[51,26,52], Alessio Trois[14], Roberto Turolla[50,53], Jacco Vink[54], Martin C. Weisskopf[17], Kinwah Wu[53], Fei Xie[55,5], and Silvia Zane[53]

*(Affiliations can be found after the references)*

Received 3 April 2023 / Accepted 10 May 2023

**ABSTRACT**

Accreting X-ray pulsars (XRPs) are presumed to be ideal targets for polarization measurements, as their high magnetic field strength is expected to polarize the emission up to a polarization degree of ∼80%. However, such expectations are being challenged by recent observations of XRPs with the Imaging X-ray Polarimeter Explorer (IXPE). Here, we report on the results of yet another XRP, namely, EXO 2030+375, observed with IXPE and contemporarily monitored with Insight-HXMT and SRG/ART-XC. In line with recent results obtained with IXPE for similar sources, an analysis of the EXO 2030+375 data returns a low polarization degree of 0%–3% in the phase-averaged study and a variation in the range of 2%–7% in the phase-resolved study. Using the rotating vector model, we constrained the geometry of the system and obtained a value of ∼60° for the magnetic obliquity. When considering the estimated pulsar inclination of ∼130°, this also indicates that the magnetic axis swings close to the observer's line of sight. Our joint polarimetric, spectral, and timing analyses hint toward a complex accreting geometry, whereby magnetic multipoles with an asymmetric topology and gravitational light bending significantly affect the behavior of the observed source.

**Key words.** magnetic fields – polarization – stars: neutron – X-rays: binaries – pulsars: individual: EXO 2030+375

## 1. Introduction

Accreting X-ray pulsars (XRPs) are binary systems consisting of a neutron star (NS) and a donor companion star (see Mushtukov & Tsygankov 2022, for a recent review). In these systems, the NS can accrete matter supplied by the companion either via stellar wind or Roche-lobe overflow, thereby producing emission in the X-ray domain. The NS can be strongly magnetized, with a dipolar magnetic field strength on the order of $10^{12}$ G. This leads to highly anisotropic accretion, where the matter is funneled by the magnetic field to the magnetic poles, giving rise to pulsating X-ray emission. Studying these systems is crucial for understanding the effects related to the interaction of X-ray radiation with strongly magnetized plasma. In fact, the emission from XRPs can be expected to be strongly polarized, up to a polarization degree (PD) of 80% due to magnetized plasma and vacuum birefringence (Gnedin et al. 1978; Pavlov & Shibanov 1979; Meszaros et al. 1988; Caiazzo & Heyl 2021b,a). However, recent observations of XRPs have revealed a polarization that is far lower than expected (Doroshenko et al. 2022; Tsygankov et al. 2022; Forsblom et al. 2023), with a

† Deceased.

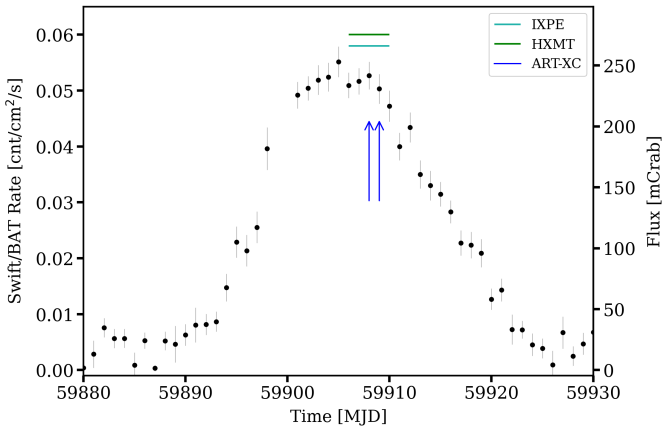


**Fig. 1.** *Swift*/BAT (15–50 keV) daily average light curve of EXO 2030+375 (black dots with gray error bars). Times of each continuous and pointed observations used in this work are marked by horizontal colored lines and vertical arrows, as detailed in the legend.

phase-averaged PD of about 5%–6% and ranging from 5% to 15% in the phase-resolved analysis.

EXO 2030+375 is an XRP discovered with the EXOSAT observatory (Parmar et al. 1989), which also detected pulsations at about 42 s. The orbital period of 46.02 days was derived from the Type I outburst periodicity by Wilson et al. (2008). These authors also obtained an orbital solution consisting of a rather eccentric (eccentricity of $e \sim 0.41$) and wide (semi-major axis of $a_x \sin i = 248 \pm 2$ lt-s) orbit. Besides being the most regular and prolific Type I outburst XRP, EXO 2030+375 also has shown sporadic Type II (or giant) outbursts (Parmar et al. 1989; Corbet & Levine 2006; Thalhammer et al. 2021). The source spectrum showed a hint of the cyclotron resonant scattering feature (CRSF) at 36 keV (Reig & Coe 1998) and 63 keV (Klochkov et al. 2008), however, this has not been securely confirmed in other works. More recently, the source spin period was measured to be around 41.2 s (Thalhammer et al. 2021), after the source underwent a significant spin-up episode following the Type II outburst, as monitored by *Fermi*/GBM[1]. The distance to the source is $2.4^{+0.5}_{-0.4}$ kpc, as given in the *Gaia* Data Release 3 (Bailer-Jones et al. 2021).

Here, we present the results of a multi-observatory campaign on EXO 2030+375. The observations by the Imaging X-ray Polarimeter Explorer (IXPE) were supplemented by contemporaneous observations with Insight-HXMT and Spectrum-Roentgen-Gamma/ART-XC at the peak of a Type I outburst in 2022.

## 2. Observations and data reduction

### 2.1. IXPE

IXPE (Weisskopf et al. 2022) is a NASA small explorer mission in collaboration with the Italian Space Agency (ASI), launched on 2021 December 9. It features three identical Mirror Module Assembly (MMAs), each comprising of a grazing incidence telescope and a polarization-sensitive Detector Unit (DU) at its focus (Baldini et al. 2021; Soffitta et al. 2021). The DUs consist of gas-pixel detectors (GPD) filled with dimethyl ether, whose interaction with X-ray photons produces photoelectrons that are ejected in a direction that is distributed as $\cos^2\varphi$, where $\varphi$ is the polarization direction of the incident radiation (Bellazzini & Angelini 2003). IXPE provides imaging polarimetry over a nominal energy band of 2–8 keV, within a field of view of about 12.9 arcmin$^2$ for each MMA and with an energy-dependent polarization sensitivity expressed by a modulation factor (i.e., the amplitude of the instrumental response to 100% polarized radiation) peaking at $\mu \sim 50\%$–$60\%$ at 8 keV.

IXPE observed EXO 2030+375 over the period 2022 November 23–27 (ObsID 02250201) for a total exposure of about 181 ks. A *Swift*/BAT (Gehrels et al. 2004; Krimm et al. 2013) light curve of the relevant outburst with IXPE and other pointed observations is shown in Fig. 1. IXPE data have been reduced using the IXPEOBSSIM software package (Baldini et al. 2022), version 30.0.0[2], and using the CALDB version 20221020. Source events were extracted from a 60″ radius circle centered on the brightest pixel, while background events are negligible given the relatively high source count rate (Di Marco et al. 2023). The `v12` version of the weighted response files (Di Marco et al. 2022) was used to produce and analyze spectral products. Based on Silvestri (2023), we added a systematic error of 2% to the IXPE spectra.

### 2.2. SRG/ART-XC

The Mikhail Pavlinsky ART-XC telescope (Pavlinsky et al. 2021) carried out two consecutive observations (ObsIDs: 12210071001, 12210071002) of EXO 2030+375, from 2022 November 25–26 (MJD 59908.87–59909.62 and 59909.71–59909.83), simultaneously with IXPE, with a total net exposure of 75 ks. ART-XC is a grazing incidence-focusing X-ray telescope on board the SRG observatory (Sunyaev et al. 2021). The telescope includes seven independent modules and provides imaging, timing, and spectroscopy in the 4–30 keV energy range, with a total effective area of ~450 cm$^2$ at 6 keV, angular resolution of 45″, energy resolution of 1.4 keV at 6 keV, and timing resolution of 23 μs. The ART-XC data were processed with the software ARTPRODUCTS v1.0 and the CALDB version 20230228. We limited the ART-XC energy band to the 6.5–25 keV energy range, where the instrument calibration is better known. Following standard procedures, we merged data from both observations, rebinned the spectrum to match the energy resolution of the detectors, and added a systematic error of 2% to it.

### 2.3. Insight-HXMT

Hard X-ray Modulation Telescope (HXMT, also dubbed as Insight-HXMT) excels in its broad energy band (1–250 keV) and a large effective area in the hard X-ray energy band (Zhang et al. 2020). EXO 2030+375 was observed by HXMT from 2022 November 18 (MJD 59901) to November 27 (MJD 59910). In this work, we only analyze quasi-simultaneous observations with IXPE from 2022 November 23 (MJD 59905) to November 27 (MJD 59910). The resulting total exposure times are 42 ks, 71 ks and 67 ks for the detectors of three payloads on board HXMT, LE (1–15 keV), ME (5–30 keV), and HE (20–250 keV), respectively. The detectors were used to generate the events in good time intervals (GTIs). The time resolution of the HE, ME, and LE instruments are ~25 μs, ~280 μs, and ~1 ms, respectively. Data from HXMT were considered in the range 2–70 keV, with the exclusion of 21–24 keV data due to the presence of an Ag feature (Li et al. 2020). Insight-HXMT Data Analysis software[3]

[1] https://gammaray.nsstc.nasa.gov/gbm/science/pulsars/lightcurves/exo2030.html

[2] https://github.com/lucabaldini/ixpeobssim

[3] http://hxmtweb.ihep.ac.cn/

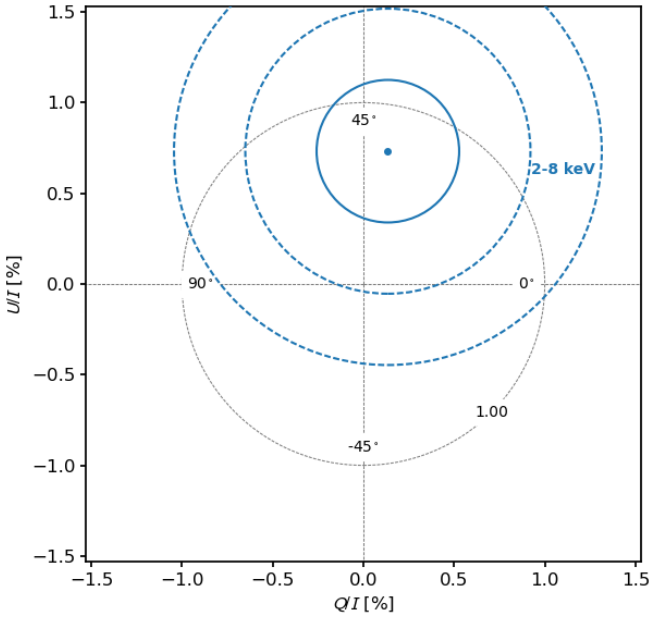


**Fig. 2.** Pulse phase-averaged normalized Stokes parameters $U/I$ ($y$-axis) and $Q/I$ ($x$-axis) over the 2–8 keV energy range. The $1\sigma$, $2\sigma$, and $3\sigma$ contours are plotted as concentric circles around the nominal value (continuous and dashed lines, respectively). The gray dotted circle represents loci of constant 1% PD, while radial lines are labeled for specific electric vector position angles (that is, the polarization angle, PA) with respect to north. The phase-averaged PD upper limit is about 2% at 99% c.l.

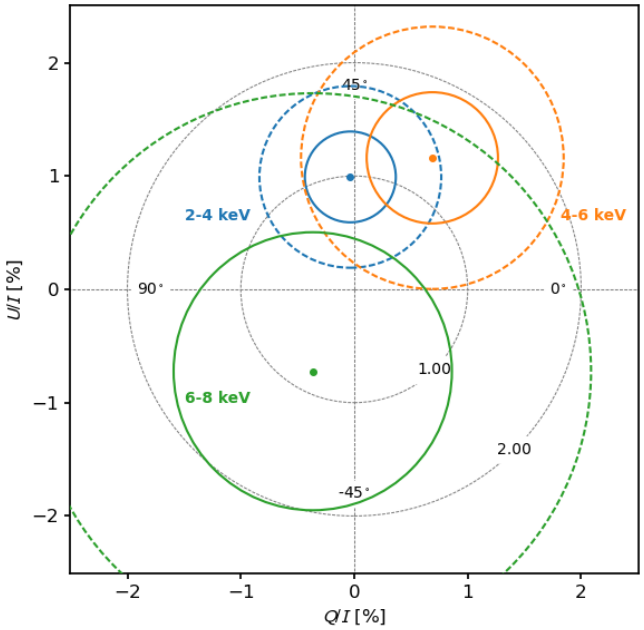


**Fig. 3.** Same details as in Fig. 2 for energy-dependent normalized Stokes parameters. Gray dotted circles represents loci of constant 1% and 2% PD. Blue, orange, and green circles represent the 2–4, 4–6 and 6–8 keV energy bands, respectively.

(HXMTDAS) v2.05 and HXMTCALDB v2.05 are used to analyze the data. We screened events for three payloads in HXMTDAS using `legtigen`, `megtigen`, `hegtigen` tasks according to the following criteria for the selection of GTIs: (1) pointing offset angle <0.1°; (2) the elevation angle >10°; (3) the geomagnetic cut-off rigidity >8 GeV; (4) the time before and after the South Atlantic Anomaly passage >300 s; (5) for LE observations, pointing direction above bright Earth >30°. We selected events from the small field of views (FoVs) for LE and ME observations, and from both small and large FoVs for HE observations due to the limitation of the background calibration. The instrumental background is estimated by blocking the collimators of some detectors completely. The background model is developed by taking the correlations of the count rates between the blind and other detectors. The background is generated with `lebkgmap`, `mebkgmap`, and `hebkgmap` implemented in HXMTDAS, respectively. We restricted the energy band for spectral analysis to 1–10, 10–30, and 30–70 keV for LE, ME, and HE, respectively, as these ranges suffer smaller calibration uncertainties given the available observational background. Following the official team recommendations, we added a systematic error of 1% to LE and ME spectra, and 3% to the HE spectrum.

## 3. Data analysis and results

Polarimetric parameters were derived following the approach based on the formalism by Kislat et al. (2015), as implemented in the `pcube` software algorithm and through spectro-polarimetric analysis available in XSPEC (Strohmayer 2017). The spectra were fitted simultaneously in XSPEC allowing for a cross-calibration constant to account for calibration uncertainties of different DUs with respect to other detectors and for intrinsic source variability. The source spectra were rebinned to have at least 30 counts per energy channel in order to adopt the $\chi^2$ fit statistic, given the non-Poissonian nature of the source spectra. The adopted test statistic was the $\chi^2$. Spectral data were analyzed with XSPEC version 12.13.0b (Arnaud 1996) available with HEASOFT v6.31.

### 3.1. Timing analysis

Barycentric correction was applied to the events using the `barycorr` tool for IXPE and ART-XC, and the HXMTDAS task `hxbary` for HXMT. DE421 Solar system ephemeris and the SIMBAD (Wenger et al. 2000) ICRS coordinates of the source were employed to this aim. Binary demodulation also was performed, employing the orbital solution from Fu et al. (2023). The final estimate of the spin period $P_s = 41.1187(1)$ s was then obtained using the phase connection technique (Deeter et al. 1981) and HXMT/LE events. The obtained spin period was used to fold the events from all employed instruments and obtain corresponding pulse profiles.

For completeness, we also extracted the IXPE light curve in the 2–8 keV energy band summed over the three DUs and rebinned at 300 s. The resulting light curve shows a steady count rate of about 5 cnt s$^{-1}$ over the whole IXPE observation.

### 3.2. Phase-averaged analysis

#### 3.2.1. Phase-averaged polarimetric analysis

Polarization quantities were initially derived following the model-independent approach described in Kislat et al. (2015) and Baldini et al. (2022). Normalized Stokes parameters, $Q/I$ and $U/I$, were extracted using the `pcube` algorithm within IXPEOBSSIM and then used to obtain the PD and PA. Figure 2 shows those parameters for the full 2–8 keV energy band, while Fig. 3 shows the same in different energy bands. Both plots show

**Table 1.** Best-fit parameters of the phase-averaged IXPE data on EXO 2030+375 obtained from spectro-polarimetric analysis using model `const×tbabs(powerlaw×polconst)` in the 2–8 keV energy band.

| Parameter | Value |
|---|---|
| $C_{\rm DU1}$ (fixed) | 1 |
| $C_{\rm DU2}$ | $0.963 \pm 0.003$ |
| $C_{\rm DU3}$ | $0.928 \pm 0.003$ |
| $N_{\rm H}$ [$10^{22}$ cm$^{-2}$] | $1.93 \pm 0.06$ |
| $\Gamma$ | $1.29 \pm 0.01$ |
| Norm [a] | $0.315 \pm 0.006$ |
| PD [%] | $1.2 \pm 0.4$ |
| PA [deg] | $39 \pm 9$ |
| $\rm Flux_{2-10\,keV}$ [b] | $2.47 \pm 0.05$ |
| $\chi^2$/d.o.f. | 1372/1334 |

**Notes.** All reported errors are at the 68% confidence level and based on the MCMC chain values. [a]Normalization of the power law in units of photon keV$^{-1}$ cm$^{-2}$ s$^{-1}$ at 1 keV. [b]Unabsorbed flux calculated for the entire model (in units of $10^{-9}$ erg cm$^{-2}$ s$^{-1}$), obtained using the `cflux` model from XSPEC as resulting from DU1.

that the normalized Stokes parameters are consistent with zero, which implies that the PD is also consistent with zero and is lower than ∼3% at 99% c.l.

### 3.2.2. Phase-averaged spectro-polarimetric analysis

To perform the spectro-polarimetric analysis, we first limited the study to IXPE data only. The $I$, $Q$, and $U$ spectra from the source were extracted using the `xpbin` algorithm for each DU. Given the narrow energy range of IXPE data, the spectra can be fitted with a simpler model than that required for broader-band analysis. We therefore employed a simple absorbed power-law model for the IXPE-only analysis. A constant polarization component (energy-independent PD and PA) was also added to the model in XSPEC. The final form of the model was thus `const×tbabs(powerlaw×polconst)`. This model returns a fit-statistic $\chi^2$/d.o.f. = 1372/1334 (see Table 1 and Fig. 4). Errors are calculated through MCMC simulations using the Goodman-Weare algorithm of length $2\times10^5$ with 20 walkers and $10^4$ burn-in steps. Best-fit results are shown in Table 1. The analysis reveals a PD of $1.2 \pm 0.6$% at the 90% c.l.

To test a possible energy-dependence of the polarization properties in EXO 2030+375, different polarization model components were also tested, namely `pollin` and `polpow` in XSPEC, corresponding to a linear and a power-law dependence with energy, respectively, of the PD and PA. However, these models did not further reduce the $\chi^2$ value, nor returned significantly different polarimetric quantities and were, therefore, not explored further.

Finally, we simultaneously fitted IXPE, HXMT, and ART-XC spectra. In principle, with a broadband spectrum available, polarimetric results suffer less contamination from a possibly incorrect spectral model derived by the restricted IXPE energy band. Following previous works (Klochkov et al. 2008; Epili et al. 2017; Fürst et al. 2018; Tamang et al. 2022), we adopted an absorbed power-law model with high-energy cutoff and an iron K$\alpha$ line. To this, we added a constant polarization component as above. As the iron line is produced by fluorescence, it is not expected to be polarized. We verified this by adding a separate `polconst` component for the continuum and for the iron line. This resulted in a best-fit model whose PD value for the iron line was pegged at its lower limit. Therefore, we left that component unaffected by polarization. The final model expression is thus `const×tbabs (powerlaw×highecut×polconst+gauss)`. For the fitting procedure, IXPE and SRG/ART-XC spectral parameters were tied to those from HXMT/LE, leaving a cross-calibration

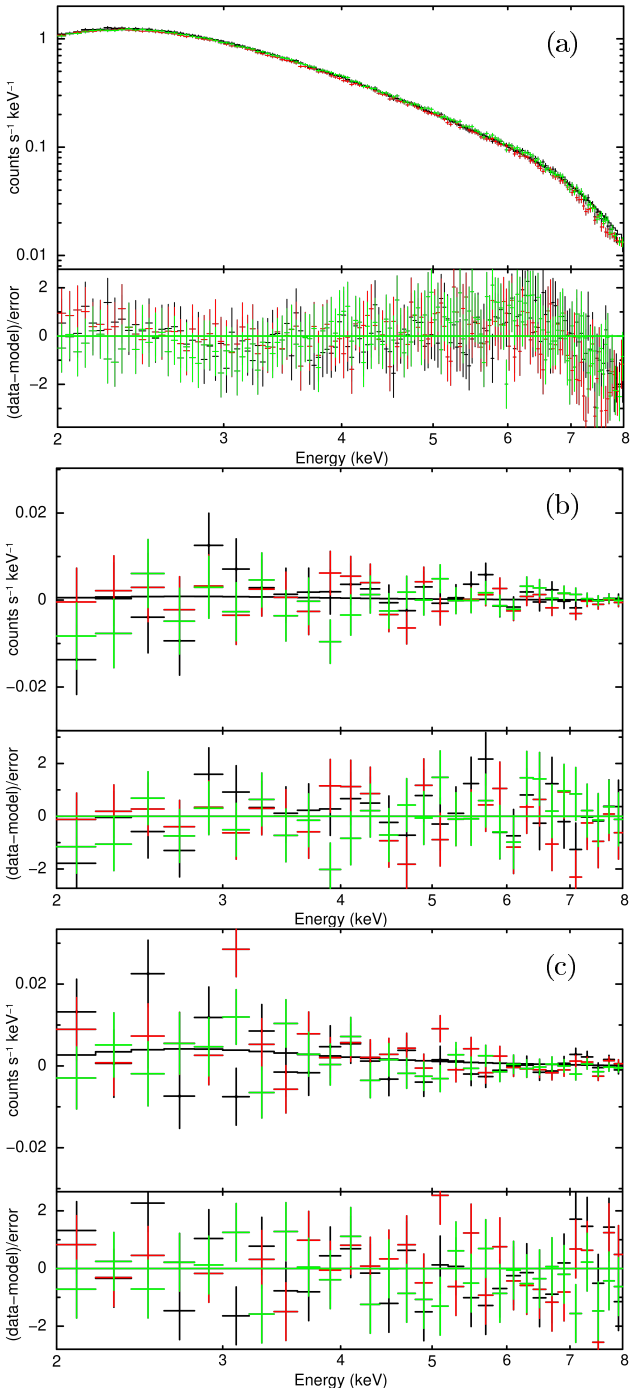


**Fig. 4.** EXO 2030+375 spectral energy distribution of the phase-averaged Stokes parameters $I$, $Q$, and $U$ as observed by IXPE – panels (a), (b), and (c), respectively. Continuous lines in the top panels represent the best-fit model `const×tbabs(powerlaw×polconst)` reported in Table 1. Bottom panels show the residuals. Different colors represent different detectors – black for DU1, red for DU2, and green for DU3. Data have been rebinned and re-normalized for plotting purpose.

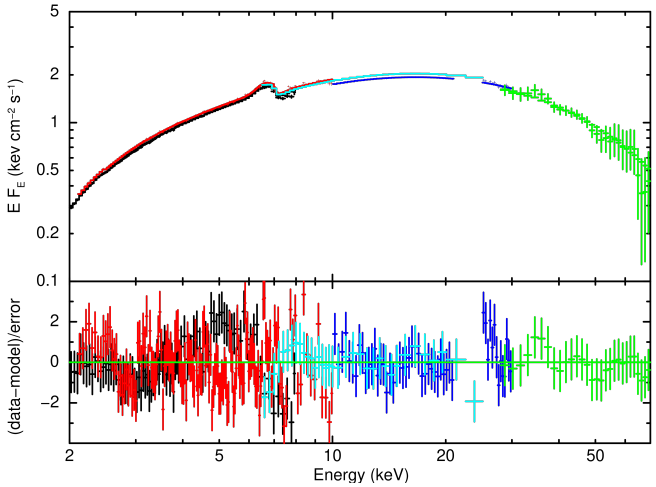


**Fig. 5.** Phase-averaged broadband spectrum of EXO 2030+375. Top: EXO 2030+375 unfolded $EF_E$ spectrum as observed by IXPE, HXMT, and ART-XC. For plotting purpose, data from the three IXPE DUs are combined and re-normalized, and all spectra are rebinned. IXPE data are in red, HXMT LE, ME, and HE in black, blue and green, respectively, ART-XC data are in cyan. Bottom: residuals of the best-fit model (also see Table 2).

constant free for each instrument. For the photoelectric absorption from neutral interstellar matter, we employed the `tbabs` model from Wilms et al. (2000) and relative `wilm` abundances. The Galactic column density in the direction of the source is about $8.8 \times 10^{21}$ cm$^{-2}$ (HI4PI Collaboration 2016).

Despite the more elaborate model (with respect to the IXPE-only analysis) and the broad 2–70 keV energy band, we were still able to verify that the obtained best-fit values of the PD and PA are in agreement with those reported in Sect. 3.2.1 within $1\sigma$. The broadband spectral results are shown in Fig. 5 and reported in Table 2.

### 3.3. Phase-resolved (spectro-)polarimetric analysis

To perform a phase-resolved polarization analysis of IXPE data, we selected seven phase bins to sample different flux levels shown by the pulse profile (see Fig. 6). The phase bins were extracted with respect to $T_0$ = 59906.82181991 MJD.

For the polarimetric analysis, we followed the Kislat et al. (2015) formalism as outlined in Sect. 3.2.1. The results, shown in Fig. 6, exhibit only a moderate variability of the Stokes parameters as a function of the pulse phase.

To perform the spectro-polarimetric analysis of the phase-resolved spectra, we used the same model as we did for the phase-averaged analysis in Sect. 3.2.2. Phase-resolved spectra were rebinned analogously to the phase-averaged analysis. For IXPE, cross-normalization constants were kept fixed at their correspondent phase-averaged value (see Table 1). The resulting best-fit values are reported in Table 3 and shown in Fig. 6. The analysis reveals significant detection of polarization up to about 7%. Both the PD and PA show pronounced variation with spin phase.

### 3.4. Phase-resolved spectral analysis

Taking advantage of the long, broadband HXMT observations, we also performed a pulse phase-resolved spectral analysis of the HXMT data. For this, 11 phase bins were chosen to provide similar statistics of spectra in each bin. However, given the limited statistics with respect to phase-averaged analysis, we limited HXMT/HE data to 50 keV. To model the phase-resolved spectra, we used the same model employed for the phase-averaged spectrum (see Sect. 3.2.2). The best-fit results are reported in Fig. 7. The analysis shows strong variability of the spectral parameters with pulse phase. We notice that the observed parameter variations might at least partly due to artificial correlations of degenerate parameters. We tested this through the calculation of contour plots for different pairs of parameters and verified that although the parameters show some intrinsic correlations, their variability is still significant. Although part of this variability is known to be model-dependent (Klochkov et al. 2008; Hemphill et al. 2014), it is nonetheless useful to test luminosity-dependence of the parameters variability with pulse phase (see Sect. 4.3).

**Table 2.** Best-fit parameters of the phase-averaged broadband spectrum of EXO 2030+375 as observed by IXPE, HXMT and ART-XC and obtained from spectro-polarimetric analysis using the model `const×tbabs(powerlaw×highecut×polconst+gauss)` in the 2–70 keV energy band.

| Parameter | Value |
|---|---|
| $N_{\rm H}$ [$10^{22}$ cm$^{-2}$] | $1.94 \pm 0.03$ |
| $\Gamma$ | $1.289 \pm 0.006$ |
| Norm$_\Gamma$ $^{(a)}$ | $0.310 \pm 0.004$ |
| $E_{\rm cut}$ [keV] | $5.8 \pm 0.1$ |
| $E_{\rm fold}$ [keV] | $23.5 \pm 0.3$ |
| $E_{{\rm K}\alpha}$ [keV] | $6.56 \pm 0.02$ |
| $\sigma_{{\rm K}\alpha}$ [keV] | $0.24 \pm 0.03$ |
| norm$_{{\rm K}\alpha}$ [ph cm$^{-2}$ s$^{-1}$] | $0.0025 \pm 0.0002$ |
| PD [%] | $1.2 \pm 0.2$ |
| PA [deg] | $39 \pm 8$ |
| $C_{\rm DU1}$ (fixed) | 1 |
| $C_{\rm DU2}$ | $0.963 \pm 0.001$ |
| $C_{\rm DU3}$ | $0.928 \pm 0.001$ |
| $C_{\rm LE}$ | $1.400 \pm 0.004$ |
| $C_{\rm ME}$ | $1.343 \pm 0.004$ |
| $C_{\rm HE}$ | $1.255 \pm 0.002$ |
| $C_{\rm ART-XC}$ | $1.395 \pm 0.004$ |
| Flux$_{1-70\,{\rm keV}}$ $^{(b)}$ | $4.44 \pm 0.01$ |
| $\chi^2$/d.o.f. | 2448/2592 |

**Notes.** All reported errors are at the 68% confidence level and based on the MCMC chain values. $^{(a)}$Normalization of the power law in units of photon cm$^{-2}$ s$^{-1}$ keV$^{-1}$ at 1 keV. $^{(b)}$Unabsorbed flux (in units of $10^{-9}$ erg cm$^{-2}$ s$^{-1}$) calculated for the entire model, obtained using the `cflux` command from XSPEC as resulting from the HXMT/LE data.

## 4. Discussion

### 4.1. Polarization degree: Expectations versus observations

Our analysis shows a low polarization for the X-ray radiation from EXO 2030+375, with the phase-averaged PD in the 0%–3% range and the phase-resolved PD values in the range of 2%–7%. High values for the PD were expected from theoretical models of accreting XRPs (Caiazzo & Heyl 2021b,a, and references therein). This is due to both plasma and vacuum birefringence, which modify the opacity in the magnetic field depending on polarization of photons. Thus, emitted photons get polarized in two normal modes, namely: ordinary (O) and extraordinary

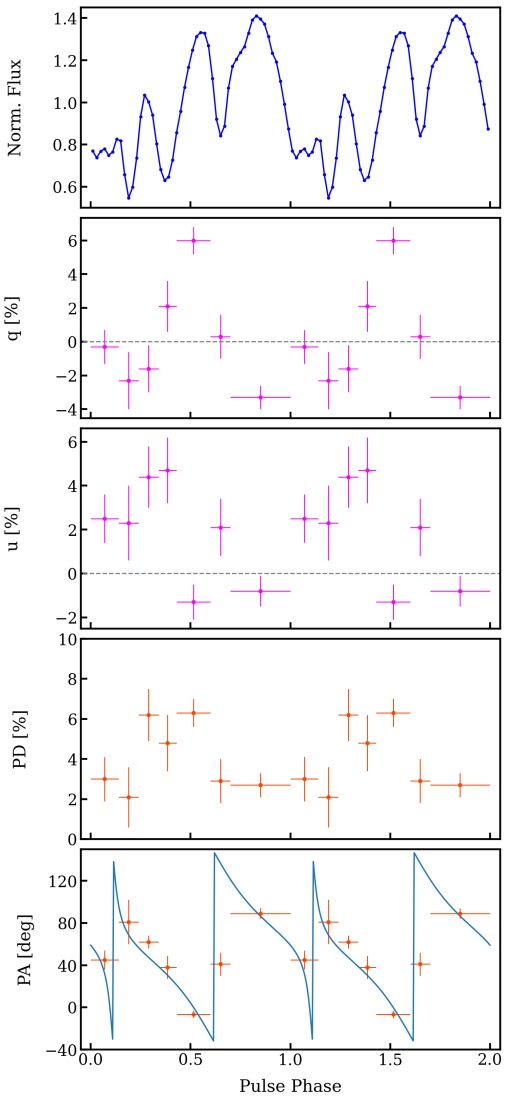


**Fig. 6.** Phase-resolved results of EXO 2030+375 in the 2–8 keV range, combining data from all IXPE DUs. From top to bottom, we show the pulse profile, normalized Stokes parameters $q$ and $u$ based on the polarimetric analysis, and the PD and PA, as obtained from the spectro-polarimetric analysis. The blue line in the PA panel corresponds to the best-fit rotating vector model (see Sect. 4.2).

(X), representing oscillations of the electric field parallel and perpendicular to the plane formed by the local magnetic field and the photon momentum, respectively.

Recently, however, those models have been challenged by IXPE observations of several accreting XRPs, namely: Her X-1 (Doroshenko et al. 2022), Cen X-3 (Tsygankov et al. 2022), 4U 1626−67 (Marshall et al. 2022), Vela X-1 (Forsblom et al. 2023), and GRO J1008−57 (Tsygankov et al. 2023). In fact, all those sources show a far lower PD than expected. The observed relatively low polarization was interpreted in terms of a "vacuum resonance" occurring where the contributions from plasma and vacuum are equal (Lai & Ho 2002). Passing through the resonance, ordinary and extraordinary polarization modes of X-ray photons would convert to each other, with a net effect of depolarizing the radiation. This process takes place at a plasma density $\rho_V \approx 10^{-4}\, B_{12}^2\, E_{\rm keV}^2\, {\rm g\,cm^{-3}}$, where $B_{12}$ is the magnetic field strength in units of $10^{12}$ G and $E_{\rm keV}$ is the photon energy in keV. Doroshenko et al. (2022) found that a transition layer of about $3\,{\rm g\,cm^{-2}}$ (corresponding to a Thomson optical depth of about unity) would depolarize the observed radiation consistently with the measured polarimetric quantities – if the vacuum resonance is located in the overheated atmospheric layer, which happens in the sub-critical (or low-) accretion regime. With the 2–10 keV flux of $2.5 \times 10^{-9}\,{\rm erg\,cm^{-2}\,s^{-1}}$ (see Table 1) and at a distance of 2.4 kpc, the observed source luminosity is $2 \times 10^{36}\,{\rm erg\,s^{-1}}$. This luminosity value is comparable to the low luminosity state of Cen X-3 (Tsygankov et al. 2022) and to the bright state of GRO J1008−57 (Tsygankov et al. 2023), as observed by IXPE. The former also shows no significant polarization in the phase-averaged analysis, while the latter shows significant polarization of about 4%. Therefore, it is possible that some other mechanisms beyond those linked to the accretion luminosity are responsible for the observed polarization degree.

One qualitative interpretation of the observed low PD is pointed by the complex pulse profile of EXO 2030+375 (see Figs. 6 and 7). Such a complexity may derive from a complex magnetic field geometry where different hot spots simultaneously contribute to the observed emission at different pulse phases. The observed low PD might therefore be interpreted as due to mixing of emission from several parts of NS surface observed at different angles.

Another interpretation can be linked to the relation between the magnetic field geometry, in particular, the magnetic obliquity and the observer's line of sight. If the magnetic dipole is nearly aligned with the rotation axis and the observer looks from the side (as seems to be the case for Her X-1 and Cen X-3), the changes in the PA with the pulsar phase are rather small and the average polarization is significant. On the other hand, for a highly inclined dipole (especially when observed at small inclinations), the variations of the dipole position angle (that is reflected in the PA) are large, resulting in a strongly reduced average polarization. This interpretation is in line with the results obtained for the system geometry in EXO 2030+375 and further discussed in the next section.

### 4.2. Geometry of the system

The polarimetric quantity PA can be exploited to constrain the geometry of the system by fitting the unbinned polarimetric measurements from individual photoelectric angles with the rotating-vector model (RVM, Radhakrishnan & Cooke 1969; Poutanen 2020). If radiation escapes in the $O$-mode, the RVM describes the PA as follows:

$$\tan({\rm PA} - \chi_{\rm p}) = \frac{-\sin\theta\,\sin(\phi-\phi_0)}{\sin i_{\rm p}\cos\theta - \cos i_{\rm p}\sin\theta\cos(\phi-\phi_0)}, \quad (1)$$

where $i_{\rm p}$ is the pulsar inclination (the angle between the pulsar spin vector and the line of sight), $\chi_{\rm p}$ is the position angle (measured from north to east) of the pulsar spin, $\theta$ is the magnetic obliquity (the angle between the magnetic dipole and the spin axis), $\phi$ is the pulse phase, and $\phi_0$ is the phase when the northern magnetic pole is closest to the observer. The other pole makes its closest approach half a period later. Using the RVM fit to the unbinned Stokes parameters on a photon-by-photon basis (González-Caniulef et al. 2023) and running Markov chain Monte Carlo (MCMC) simulations, we obtained estimates of the pulsar inclination, namely: $i_{\rm p} = 129^{+9}_{-7}$ deg, along with the co-latitude of the magnetic pole (or magnetic obliquity), $\theta = 59^{+5}_{-6}$ deg, and the position angle of the pulsar spin, $\chi_{\rm p} = \chi_{\rm p,O} = -30 \pm 5$ deg (see Fig. 8). With the pulsar inclination and magnetic obliquity angles being almost supplementary, $i_{\rm p} + \theta \approx 180°$,

**Table 3.** Best-fit results of the spectro-polarimetric analysis of the phase-resolved IXPE data of EXO 2030+375 using the `const×tbabs(powerlaw×polconst)` model in the 2–8 keV energy band.

| Phase | $N_{\rm H}$ ($10^{22}$ cm$^{-2}$) | $\Gamma$ | Norm [(a)] | PD (%) | PA (deg) | $\chi^2$/d.o.f. |
|---|---|---|---|---|---|---|
| 0.00–0.18 | 2.9 ± 0.1 | 1.42 ± 0.02 | 4.9 ± 0.2 | 3.0 ± 1.1 | 45 ± 9 | 991/1037 |
| 0.18–0.26 | 3.2 ± 0.2 | 1.53 ± 0.04 | 2.3 ± 0.1 | 2.1 ± 1.5 | 81 ± 21 | 1015/1098 |
| 0.26–0.35 | 3.4 ± 0.1 | 1.44 ± 0.03 | 3.2 ± 0.1 | 6.2 ± 1.3 | 62 ± 6 | 938/974 |
| 0.35–0.44 | 2.3 ± 0.1 | 1.07 ± 0.03 | 1.4 ± 0.1 | 4.8 ± 1.5 | 38 ± 11 | 754/788 |
| 0.44–0.63 | 3.34 ± 0.09 | 1.17 ± 0.02 | 6.4 ± 0.2 | 6.3 ± 0.7 | −6.5 ± 3.3 | 878/905 |
| 0.63–0.72 | 2.5 ± 0.1 | 1.22 ± 0.03 | 2.4 ± 0.1 | 2.9 ± 1.1 | 41 ± 11 | 1009/1048 |
| 0.72–1.00 | 3.06 ± 0.07 | 1.30 ± 0.02 | 10.9 ± 0.2 | 2.7 ± 0.6 | 89 ± 5 | 1103/1222 |

**Notes.** All reported errors are at 68% confidence level. [(a)]Normalization of the power law in units of $10^{-2}$ photon keV$^{-1}$ cm$^{-2}$ s$^{-1}$ at 1 keV as obtained from DU1.

the southern magnetic pole swings close to the observer line of sight at each pulsar rotation at half a period from phase $\phi_0/(2\pi)$, that is: at $\phi = 0.11^{+0.02}_{-0.01}$.

Interestingly, in the case of EXO 2030+375 the RVM suggests a relatively high magnetic obliquity. Other XRPs (e.g., Her X-1, Cen X-3) show $\theta \approx 15°$, while a value of $\theta \approx 60°$ observed from EXO 2030+375 is closer to the orthogonal rotator GRO J1008−57 (Tsygankov et al. 2023). These results indicate that EXO 2030+375 stands in between the bimodal distribution peaking at 0° and 90° of the magnetic obliquity expected for isolated NSs (Dall'Osso & Perna 2017; Lander & Jones 2018), although such results do not necessarily apply to accreting XRPs (Biryukov & Abolmasov 2021).

The orbital inclination can be obtained from the orbital parameters measured by Wilson et al. (2008). For the optical companion stellar mass in the range 17–20 $M_\odot$, corresponding to B0V spectral class (Coe et al. 1988), and assuming a NS mass of 1.4 $M_\odot$, the inclination is in the range 49°–55° (see also Laplace et al. 2017). This value is consistent with the pulsar inclination value derived through the RVM fit because the sense of rotation cannot be determined from the X-ray pulse arrival times (i.e., solutions in the range $i_{\rm orb} = 125°$–$131°$ are equally probable).

### 4.3. HXMT phase-resolved spectral results

Spectral parameters are expected to show pulse phase-dependence due to the highly anisotropic accretion geometry in XRPs. We therefore performed phase-resolved spectroscopy of HXMT EXO 2030+375 data (see Fig. 7). Phase-resolved spectroscopy of EXO 2030+375 was also performed in earlier works (Klochkov et al. 2008; Naik & Jaisawal 2015; Tamang et al. 2022). However, despite the main continuum model used in past works is similar to the one adopted here, several important differences prevent a direct comparison. In fact, XRP spectra are known to be luminosity-dependent (Mushtukov & Tsygankov 2022) and, as a consequence, different spectral components can be adopted to fit the data collected at different luminosity levels.

For EXO 2030+375, the main continuum model was modified in different works with additional components such as a Gaussian absorption line around 10 keV (Klochkov et al. 2008) or a partial covering component (Naik & Jaisawal 2015; Tamang et al. 2022). Therefore, only a qualitative comparison can be made between the results obtained here and those from previous works. For example, observations carried out by Klochkov et al. (2008) of EXO 2030+375 show that the power-law photon index reaches a minimum around the main pulse

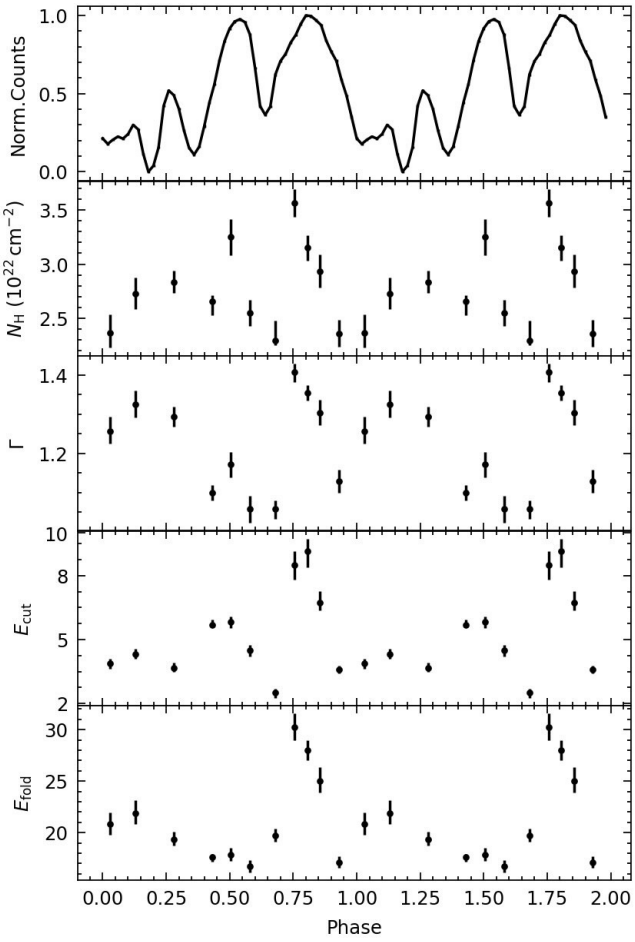


**Fig. 7.** Best-fit parameters for the broadband (2−50 keV) phase-resolved spectra of EXO 2030+375 as observed by HXMT. Panels from top to bottom show the pulse profile as observed by HXMT/LE in the 2–10 keV energy band; the column density, $N_{\rm H}$; the power-law photon index Γ; the cutoff energy; and the folding energy (both in keV).

profile peak (corresponding to the broad main peak at $\phi \sim 0.8$ in Fig. 7). A similar trend has emerged also from the phase-resolved results observed in Her X-1 (Vasco et al. 2013). Here, in contrast, we observe a maximum value of the photon index around the same peak (see Fig. 7). This is likely a consequence of the luminosity difference, as the above-mentioned works derive their results in the high-luminosity accretion regime

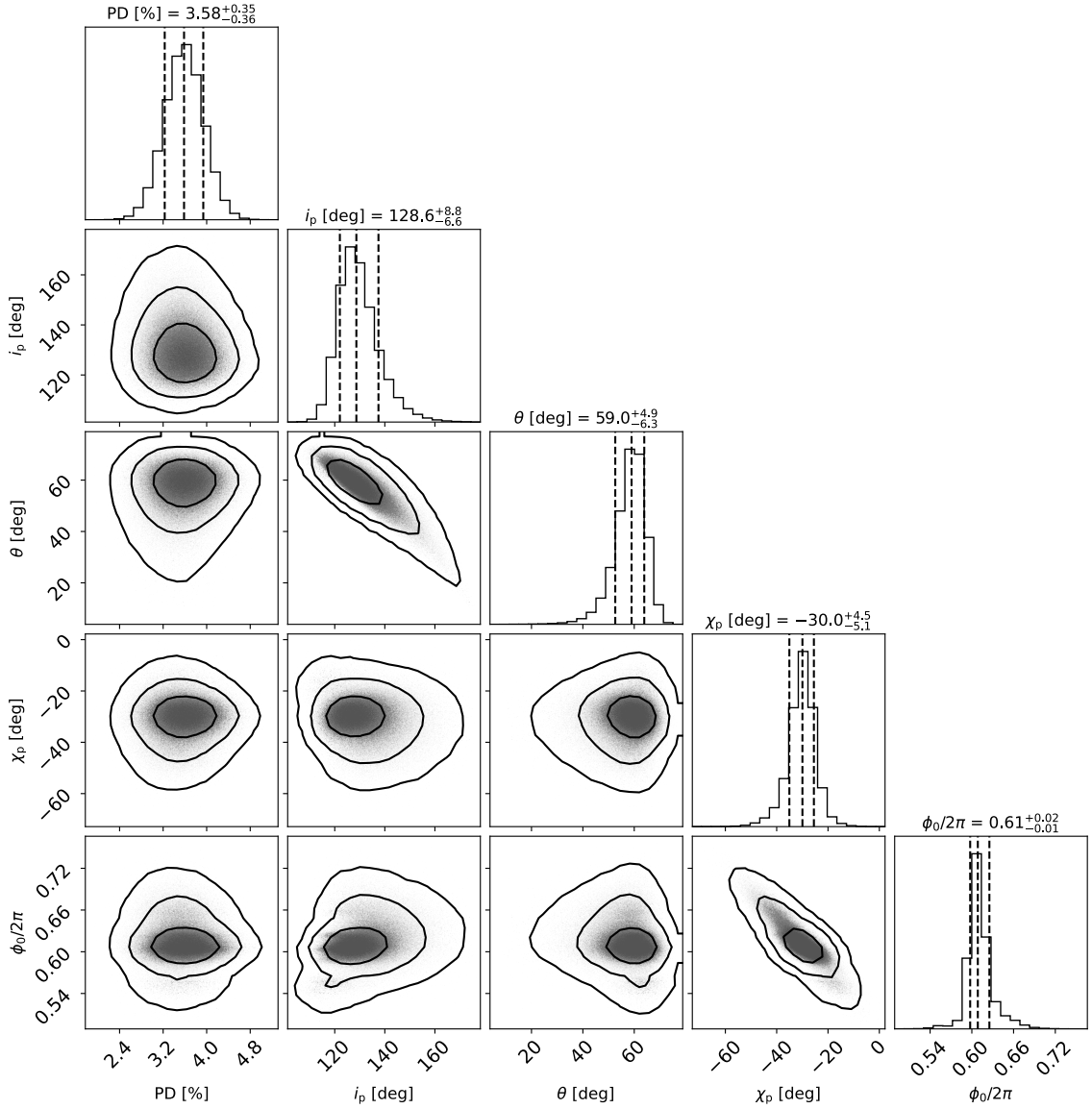


**Fig. 8.** Corner plot of the posterior distribution for the RVM parameters for the pulsar geometry obtained using the PA values. Parameters are the PD of radiation escaping from the magnetic pole, pulsar inclination, $i_p$; magnetic obliquity, $\theta$; position angle, $\chi_p$; and the phase, $\phi_0$. 2D contours correspond to 68%, 95% and 99% confidence levels. The histograms show the normalized 1D distribution for a given parameter derived from the posterior samples. The mean value and $1\sigma$ confidence levels for the derived parameters are reported above the corresponding histogram.

($10^{37-38}$ erg s$^{-1}$, that is near or above the critical luminosity), whereas in the present work the source has been observed at sub-critical luminosity ($\sim 4 \times 10^{36}$ erg s$^{-1}$). Such a difference is reflected in two main aspects. On the one side, the accretion structure beaming pattern is expected to drastically change at different regimes. In fact, the EXO 2030+375 pulse profile observed in the high-luminosity regime (see, e.g., the 2–9 keV panel in Fig. 2 of Klochkov et al. 2008) exhibits substantial differences with what is observed in the present work (see top panel in Fig. 7). This can lead to opposite observational signatures if the observer looks through the optically deep walls of the accretion column in the super-critical regime or through the optically thin hot-spots in the sub-critical regime (Mushtukov et al. 2015; Becker & Wolff 2022). On the other hand, opposite luminosity-dependences of spectral parameters have been observed in different accretion regimes in XRPs, depending on whether a gas-mediated or a radiation-dominated shock is responsible for the infalling plasma deceleration (Klochkov et al. 2011, and references therein). Although such behavior has generally been observed in the pulse-averaged analysis (see, e.g., Müller et al. 2013; Reig & Nespoli 2013; Malacaria et al. 2015; Diez et al. 2022), pulse-to-pulse spectroscopy hints at the possibility that similar trends are at work on shorter timescales (Klochkov et al. 2011; Vybornov et al. 2017; Müller et al. 2013) and that even phase-resolved spectroscopy exhibits a pulse-phase dependence of most parameters on luminosity (Lutovinov et al. 2016).

The system geometry derived in Sect. 4.2 shows that the southern magnetic pole swings close to the observer line of sight at phase 0.1 (that is, half a period from $\phi_0$). As the observation is carried out at sub-critical accretion, an accretion column with emitting walls contributing at neighbor phases is not expected. Thus, the main pulse profile peak at phase 0.8 is perhaps due to light bending from pencil beam emission at the magnetic poles. Such emission is generated in an optically thin environment at the hot-spot and it is therefore intrinsically soft, leading to a maximum of the photon index. However, this

scenario would likely produce a symmetrical behavior of the spectral parameters dependence around the phase $\phi_0$, which is not observed here. This result, together with the highly-structured pulse profile, hints to a more complex NS configuration, such as a multipolar or asymmetric topology of the magnetic field. This kind of magnetic field configuration has also been recently proposed for other XRPs (Postnov et al. 2013; Tsygankov et al. 2017; Israel et al. 2017; Mönkkönen et al. 2022).

## 5. Summary

Our main results can be summarized as follows:

- EXO 2030+375 was observed in November 2022 by IXPE, HXMT and ART-XC at the peak of a low-luminosity Type I outburst.
- Only a low polarization degree of 0%–3% has been found in the phase-averaged analysis, while the phase-resolved analysis reveals a PD in the range of 2%–7%.
- The observed low PD can be explained in terms of an overheated NS atmosphere scenario, with additional depolarizing mechanisms possibly at work in EXO 2030+375. We propose that mixing of emission from several parts of the NS surface observed at different angles, on one hand, and variations of the dipole position angle resulting in changes in the PA on the other, would lead to further depolarization.
- By means of the rotating vector model, we constrained the geometry of the accreting pulsar. The pulsar inclination is ∼130°, almost supplementary to the magnetic obliquity angle, at ∼60° (that is, their sum is ∼180°). The obtained pulsar geometry implies that the magnetic axis swings close to the observer line of sight and the system obliquity stands between orthogonal and aligned rotators.
- The spectral phase-resolved analysis shows evidence that the pulse phase dependence of spectral parameters is different for different luminosities. This possibly reflects changes in the accretion structure at different accretion regimes, accompanied by beam pattern changes.
- Polarimetric, spectral, and timing analyses all hint toward a complex accretion geometry, where magnetic multipoles with asymmetric topology and gravitational light bending have significant effects on the resulting spectral and timing behavior of EXO 2030+375.

Our analysis of EXO 2030+375 characterized the X-ray polarimetric and spectral properties of the source at the sub-critical accretion regime. Additional future observations at different luminosities would help discerning the various mechanisms at work that shape the X-ray emission properties.

*Acknowledgements.* The Imaging X-ray Polarimetry Explorer (IXPE) is a joint US and Italian mission. The US contribution is supported by the National Aeronautics and Space Administration (NASA) and led and managed by its Marshall Space Flight Center (MSFC) with industry partner Ball Aerospace (contract NNM15AA18C). The Italian contribution is supported by the Italian Space Agency (Agenzia Spaziale Italiana, ASI) through contract ASI-OHBI-2017-12-I.0, agreements ASI-INAF-2017-12-H0 and ASI-INFN-2017.13-H0, and its Space Science Data Center (SSDC) with agreements ASI-INAF-2022-14-HH.0 and ASI-INFN 2021-43-HH.0, and by the Istituto Nazionale di Astrofisica (INAF) and the Istituto Nazionale di Fisica Nucleare (INFN) in Italy. This research used data products provided by the IXPE Team (MSFC, SSDC, INAF, and INFN) and distributed with additional software tools by the High-Energy Astrophysics Science Archive Research Center (HEASARC), which is a service of the Astrophysics Science Division at NASA/GSFC and the High Energy Astrophysics Division of the Smithsonian Astrophysical Observatory. We acknowledge extensive use of the NASA Abstract Database Service (ADS). This research was supported by the International Space Science Institute (ISSI) in Bern, through ISSI International Team project 495. JH acknowledges support from the Natural Sciences and Engineering Research Council of Canada (NSERC) through a Discovery Grant, the Canadian Space Agency through the co-investigator grant program, and computational resources and services provided by Compute Canada, Advanced Research Computing at the University of British Columbia, and the SciServer science platform (www.sciserver.org). We also acknowledge support from the Academy of Finland grants 333112, 349144, 349373, and 349906 (SST, JP), the German Academic Exchange Service (DAAD) travel grant 57525212 (VD, VFS), the Väisälä Foundation (SST), the Russian Science Foundation grant 19-12-00423 (AAL, IAM, SVM, AES), the French National Centre for Scientific Research (CNRS), and the French National Centre for Space Studies (CNES) (POP). We thank Lingda Kong and Youli Tuo for their helpful assistance in the HXMT data analysis.

## References

Arnaud, K. A. 1996, in Astronomical Data Analysis Software and Systems V, eds. G. H. Jacoby, & J. Barnes (San Francisco: ASP), ASP Conf. Ser., 101, 17
Bailer-Jones, C. A. L., Rybizki, J., Fouesneau, M., Demleitner, M., & Andrae, R. 2021, AJ, 161, 147
Baldini, L., Barbanera, M., Bellazzini, R., et al. 2021, Astropart. Phys., 133, 102628
Baldini, L., Bucciantini, N., Lalla, N. D., et al. 2022, SoftwareX, 19, 101194
Becker, P. A., & Wolff, M. T. 2022, ApJ, 939, 67
Bellazzini, R., & Angelini, F. 2003, in Polarimetry in Astronomy, ed. S. Fineschi, Proc. SPIE, 4843, 383
Biryukov, A., & Abolmasov, P. 2021, MNRAS, 505, 1775
Caiazzo, I., & Heyl, J. 2021a, MNRAS, 501, 129
Caiazzo, I., & Heyl, J. 2021b, MNRAS, 501, 109
Coe, M. J., Longmore, A., Payne, B. J., & Hanson, C. G. 1988, MNRAS, 232, 865
Corbet, R. H. D., & Levine, A. M. 2006, ATel, 843, 1
Dall'Osso, S., & Perna, R. 2017, MNRAS, 472, 2142
Deeter, J. E., Boynton, P. E., & Pravdo, S. H. 1981, ApJ, 247, 1003
Diez, C. M., Grinberg, V., Fürst, F., et al. 2022, A&A, 660, A19
Di Marco, A., Costa, E., Muleri, F., et al. 2022, AJ, 163, 170
Di Marco, A., Soffitta, P., Costa, E., et al. 2023, AJ, 165, 143
Doroshenko, V., Poutanen, J., Tsygankov, S. S., et al. 2022, Nat. Astron., 6, 1433
Epili, P., Naik, S., Jaisawal, G. K., & Gupta, S. 2017, MNRAS, 472, 3455
Forsblom, S. V., Poutanen, J., Tsygankov, S. S., et al. 2023, ApJ, 947, L20
Fu, Y.-C., Song, L. M., Ding, G. Q., et al. 2023, MNRAS, 521, 893
Fürst, F., Falkner, S., Marcu-Cheatham, D., et al. 2018, A&A, 620, A153
Gehrels, N., Chincarini, G., Giommi, P., et al. 2004, ApJ, 611, 1005
Gnedin, Y. N., Pavlov, G. G., & Shibanov, Y. A. 1978, Sov. Astron. Lett., 4, 117
González-Caniulef, D., Caiazzo, I., & Heyl, J. 2023, MNRAS, 519, 5902
Hemphill, P. B., Rothschild, R. E., Markowitz, A., et al. 2014, ApJ, 792, 14
HI4PI Collaboration (Ben Bekhti, N., et al.) 2016, A&A, 594, A116
Israel, G. L., Belfiore, A., Stella, L., et al. 2017, Science, 355, 817
Kislat, F., Clark, B., Beilicke, M., & Krawczynski, H. 2015, Astropart. Phys., 68, 45
Klochkov, D., Santangelo, A., Staubert, R., & Ferrigno, C. 2008, A&A, 491, 833
Klochkov, D., Staubert, R., Santangelo, A., Rothschild, R. E., & Ferrigno, C. 2011, A&A, 532, A126
Krimm, H. A., Holland, S. T., Corbet, R. H. D., et al. 2013, ApJS, 209, 14
Lai, D., & Ho, W. C. G. 2002, ApJ, 566, 373
Lander, S. K., & Jones, D. I. 2018, MNRAS, 481, 4169
Laplace, E., Mihara, T., Moritani, Y., et al. 2017, A&A, 597, A124
Li, X., Li, X., Tan, Y., et al. 2020, J. High Energy Astrophys., 27, 64
Lutovinov, A. A., Buckley, D. A. H., Townsend, L. J., Tsygankov, S. S., & Kennea, J. 2016, MNRAS, 462, 3823
Malacaria, C., Klochkov, D., Santangelo, A., & Staubert, R. 2015, A&A, 581, A121
Marshall, H. L., Ng, M., Rogantini, D., et al. 2022, ApJ, 940, 70
Meszaros, P., Novick, R., Szentgyorgyi, A., Chanan, G. A., & Weisskopf, M. C. 1988, ApJ, 324, 1056
Mönkkönen, J., Tsygankov, S. S., Mushtukov, A. A., et al. 2022, MNRAS, 515, 571
Müller, D., Klochkov, D., Caballero, I., & Santangelo, A. 2013, A&A, 552, A81
Mushtukov, A., & Tsygankov, S. 2022, in Handbook of X-ray and Gamma-ray Astrophysics, eds. C. Bambi, & A. Santangelo (Singapore: Springer)
Mushtukov, A. A., Suleimanov, V. F., Tsygankov, S. S., & Poutanen, J. 2015, MNRAS, 447, 1847
Naik, S., & Jaisawal, G. K. 2015, RAA, 15, 537
Parmar, A. N., White, N. E., Stella, L., Izzo, C., & Ferri, P. 1989, ApJ, 338, 359
Pavlinsky, M., Tkachenko, A., Levin, V., et al. 2021, A&A, 650, A42
Pavlov, G. G., & Shibanov, Y. A. 1979, Sov. J. Exp. Theoret. Phys., 49, 741
Postnov, K., Shakura, N., Staubert, R., et al. 2013, MNRAS, 435, 1147
Poutanen, J. 2020, A&A, 641, A166
Radhakrishnan, V., & Cooke, D. J. 1969, ApJ, 3, 225

Reig, P., & Coe, M. J. 1998, MNRAS, 294, 118
Reig, P., & Nespoli, E. 2013, A&A, 551, A1
Silvestri, S., & IXPE Collaboration 2023, Nucl. Instrum. Methods Phys. Res. A, 1048, 167938
Soffitta, P., Baldini, L., Bellazzini, R., et al. 2021, AJ, 162, 208
Strohmayer, T. E. 2017, ApJ, 838, 72
Sunyaev, R., Arefiev, V., Babyshkin, V., et al. 2021, A&A, 656, A132
Tamang, R., Ghising, M., Tobrej, M., Rai, B., & Paul, B. C. 2022, MNRAS, 515, 5407
Thalhammer, P., Ballhausen, R., Pottschmidt, K., et al. 2021, ATel, 14911, 1
Tsygankov, S. S., Doroshenko, V., Lutovinov, A. A., Mushtukov, A. A., & Poutanen, J. 2017, A&A, 605, A39
Tsygankov, S. S., Doroshenko, V., Poutanen, J., et al. 2022, ApJ, 941, L14
Tsygankov, S. S., Doroshenko, V., Mushtukov, A. A., et al. 2023, A&A, in press https://doi.org/10.1051/0004-6361/202346134
Vasco, D., Staubert, R., Klochkov, D., et al. 2013, A&A, 550, A111
Vybornov, V., Klochkov, D., Gornostaev, M., et al. 2017, A&A, 601, A126
Weisskopf, M. C., Soffitta, P., Baldini, L., et al. 2022, JATIS, 8, 026002
Wenger, M., Ochsenbein, F., Egret, D., et al. 2000, A&AS, 143, 9
Wilms, J., Allen, A., & McCray, R. 2000, ApJ, 542, 914
Wilson, C. A., Finger, M. H., & Camero-Arranz, A. 2008, ApJ, 678, 1263
Zhang, S.-N., Li, T., Lu, F., et al. 2020, Sci. China Phys. Mech. Astron., 63, 249502

[1] International Space Science Institute, Hallerstrasse 6, 3012 Bern, Switzerland
e-mail: cmalacaria.astro@gmail.com
[2] University of British Columbia, Vancouver, BC V6T 1Z4, Canada
[3] Institut für Astronomie und Astrophysik, Universität Tübingen, Sand 1, 72076 Tübingen, Germany
[4] Department of Physics and Astronomy, University of Turku, 20014 Turku, Finland
[5] INAF Istituto di Astrofisica e Planetologia Spaziali, Via del Fosso del Cavaliere 100, 00133 Roma, Italy
[6] ISDC Data Center for Astrophysics, Université de Genève, 16 chemin d'Écogia, 1290 Versoix, Switzerland
[7] Space Research Institute (IKI) of Russian Academy of Sciences, Prosoyuznaya ul 84/32, 117997 Moscow, Russian Federation
[8] MIT Kavli Institute for Astrophysics and Space Research, Massachusetts Institute of Technology, 77 Massachusetts Avenue, Cambridge, MA 02139, USA
[9] Astrophysics, Department of Physics, University of Oxford, Denys Wilkinson Building, Keble Road, Oxford OX1 3RH, UK
[10] Université Grenoble Alpes, CNRS, IPAG, 38000 Grenoble, France
[11] Instituto de Astrofísicade Andalucía – CSIC, Glorieta de la Astronomía s/n, 18008 Granada, Spain
[12] INAF – Osservatorio Astronomico di Roma, Via Frascati 33, 00040 Monte Porzio Catone, RM, Italy
[13] Space Science Data Center, Agenzia Spaziale Italiana, Via del Politecnico snc, 00133 Roma, Italy
[14] INAF – Osservatorio Astronomico di Cagliari, Via della Scienza 5, 09047 Selargius, CA, Italy
[15] Istituto Nazionale di Fisica Nucleare, Sezione di Pisa, Largo B. Pontecorvo 3, 56127 Pisa, Italy
[16] Dipartimento di Fisica, Università di Pisa, Largo B. Pontecorvo 3, 56127 Pisa, Italy
[17] NASA Marshall Space Flight Center, Huntsville, AL 35812, USA
[18] Dipartimento di Matematica e Fisica, Università degli Studi Roma Tre, Via della Vasca Navale 84, 00146 Roma, Italy
[19] Istituto Nazionale di Fisica Nucleare, Sezione di Torino, Via Pietro Giuria 1, 10125 Torino, Italy
[20] Dipartimento di Fisica, Università degli Studi di Torino, Via Pietro Giuria 1, 10125 Torino, Italy
[21] INAF – Osservatorio Astrofisico di Arcetri, Largo Enrico Fermi 5, 50125 Firenze, Italy
[22] Dipartimento di Fisica e Astronomia, Università degli Studi di Firenze, Via Sansone 1, 50019 Sesto Fiorentino, FI, Italy
[23] Istituto Nazionale di Fisica Nucleare, Sezione di Firenze, Via Sansone 1, 50019 Sesto Fiorentino, FI, Italy
[24] Agenzia Spaziale Italiana, Via del Politecnico snc, 00133 Roma, Italy
[25] Science and Technology Institute, Universities Space Research Association, Huntsville, AL 35805, USA
[26] Istituto Nazionale di Fisica Nucleare, Sezione di Roma "Tor Vergata", Via della Ricerca Scientifica 1, 00133 Roma, Italy
[27] Department of Physics and Kavli Institute for Particle Astrophysics and Cosmology, Stanford University, Stanford, CA 94305, USA
[28] Astronomical Institute of the Czech Academy of Sciences, Bocní- II 1401/1, 14100 Praha 4, Czech Republic
[29] RIKEN Cluster for Pioneering Research, 2-1 Hirosawa, Wako, Saitama 351-0198, Japan
[30] California Institute of Technology, Pasadena, CA 91125, USA
[31] Yamagata University, 1-4-12 Kojirakawa-machi, Yamagata-shi 990-8560, Japan
[32] Osaka University, 1-1 Yamadaoka, Suita, Osaka 565-0871, Japan
[33] International Center for Hadron Astrophysics, Chiba University, Chiba 263-8522, Japan
[34] Institute for Astrophysical Research, Boston University, 725 Commonwealth Avenue, Boston, MA 02215, USA
[35] Department of Astrophysics, St. Petersburg State University, Universitetsky pr. 28, Petrodvoretz 198504, St. Petersburg, Russia
[36] Department of Physics and Astronomy and Space Science Center, University of New Hampshire, Durham, NH 03824, USA
[37] Physics Department and McDonnell Center for the Space Sciences, Washington University in St. Louis, St. Louis, MO 63130, USA
[38] Finnish Centre for Astronomy with ESO, University of Turku, 20014 Turku, Finland
[39] Istituto Nazionale di Fisica Nucleare, Sezione di Napoli, Strada Comunale Cinthia, 80126 Napoli, Italy
[40] Université de Strasbourg, CNRS, Observatoire Astronomique de Strasbourg, UMR 7550, 67000 Strasbourg, France
[41] Graduate School of Science, Division of Particle and Astrophysical Science, Nagoya University, Furo-cho, Chikusa-ku, Nagoya, Aichi 464-8602, Japan
[42] Hiroshima Astrophysical Science Center, Hiroshima University, 1-3-1 Kagamiyama, Higashi-Hiroshima, Hiroshima 739-8526, Japan
[43] University of Maryland, Baltimore County, Baltimore, MD 21250, USA
[44] NASA Goddard Space Flight Center, Greenbelt, MD 20771, USA
[45] Center for Research and Exploration in Space Science and Technology, NASA/GSFC, Greenbelt, MD 20771, USA
[46] Department of Physics, University of Hong Kong, Pokfulam, Hong Kong
[47] Department of Astronomy and Astrophysics, Pennsylvania State University, University Park, PA 16801, USA
[48] Center for Astrophysics, Harvard & Smithsonian, 60 Garden St, Cambridge, MA 02138, USA
[49] INAF – Osservatorio Astronomico di Brera, Via E. Bianchi 46, 23807 Merate, LC, Italy
[50] Dipartimento di Fisica e Astronomia, Università degli Studi di Padova, Via Marzolo 8, 35131 Padova, Italy
[51] Dipartimento di Fisica, Università degli Studi di Roma "Tor Vergata", Via della Ricerca Scientifica 1, 00133 Roma, Italy
[52] Department of Astronomy, University of Maryland, College Park, Maryland 20742, USA
[53] Mullard Space Science Laboratory, University College London, Holmbury St Mary, Dorking, Surrey RH5 6NT, UK
[54] Anton Pannekoek Institute for Astronomy & GRAPPA, University of Amsterdam, Science Park 904, 1098, XH Amsterdam, The Netherlands
[55] Guangxi Key Laboratory for Relativistic Astrophysics, School of Physical Science and Technology, Guangxi University, Nanning 530004, PR China

# 4

# REFERENCES


Arnaud, K. A. 1996, in Astronomical Society of the Pacific Conference Series, Vol. 101, Astronomical Data Analysis Software and Systems V, ed. G. H. Jacoby & J. Barnes, 17

Avakyan, A., Neumann, M., Zainab, A., et al. 2023, Astronomy  Astrophysics, 675, A199

Bailer-Jones, C. A. L., Rybizki, J., Fouesneau, M., Demleitner, M., & Andrae, R. 2021, The Astronomical Journal, 161, 147

Bambi, C. & Santangelo, A. 2022, Handbook of X-ray and Gamma-ray Astrophysics

Barthelmy, S. D., Barbier, L. M., Cummings, J. R., et al. 2005, Space Science Reviews, 120, 143

Basko, M. M. & Sunyaev, R. A. 1976, Monthly Notices of the Royal Astronomical Society, 175, 395

Becker, P. A., Klochkov, D., Schönherr, G., et al. 2012, Astronomy  Astrophysics, 544, A123

Becker, P. A. & Wolff, M. T. 2007, The Astrophysical Journal, 654, 435

Cao, X., Jiang, W., Meng, B., et al. 2020, Science China Physics, Mechanics, and Astronomy, 63, 249504

Chandrasekhar, S. 1931, The Astrophysical Journal, 74, 81

Chen, Y., Cui, W., Li, W., et al. 2020, Science China Physics, Mechanics, and Astronomy, 63, 249505

Chodil, G., Mark, H., Rodrigues, R., Seward, F. D., & Swift, C. D. 1967, The Astrophysical Journal, 150, 57

Cusumano, G., La Parola, V., D'Aì, A., et al. 2016, Monthly Notices of the Royal Astronomical Society, 460, L99

Daugherty, J. K. & Harding, A. K. 1986, The Astrophysical Journal, 309, 362

Diez, C. M., Grinberg, V., Fürst, F., et al. 2022, Astronomy  Astrophysics, 660, A19

Doroshenko, V., Tsygankov, S. S., Mushtukov, A. A., et al. 2017, Monthly Notices of the Royal Astronomical Society, 466, 2143

Du, Y.-J., Ducci, L., Ji, L., et al. 2025, Astronomy  Astrophysics, 694, A156

Fürst, F., Kreykenbohm, I., Pottschmidt, K., et al. 2010, Astronomy  Astrophysics, 519, A37

Fürst, F., Pottschmidt, K., Wilms, J., et al. 2014, in American Astronomical Society Meeting Abstracts, Vol. 223, American Astronomical Society Meeting Abstracts #223, 438.20

Gehrels, N., Chincarini, G., Giommi, P., et al. 2004, The Astrophysical Journal, 611, 1005

Gnedin, I. N. & Sunyaev, R. A. 1974, Astronomy  Astrophysics, 36, 379

Harrison, F. A., Craig, W. W., Christensen, F. E., et al. 2013, The Astrophysical Journal, 770, 103

Heger, A., Fryer, C. L., Woosley, S. E., Langer, N., & Hartmann, D. H. 2003, The Astrophysical Journal, 591, 288

Hertzsprung, E. 1911, Publikationen des Astrophysikalischen Observatoriums zu Potsdam, 63

Hilditch, R. W. 2001, An Introduction to Close Binary Stars

Hiltner, W. A., Werner, J., & Osmer, P. 1972, The Astrophysical Journal Letters, 175, L19

Hou, X., Ge, M. Y., Ji, L., et al. 2022, The Astrophysical Journal, 938, 149

Inoue, H. 1975, Publications of the Astronomical Society of Japan, 27, 311

Ji, L., Doroshenko, V., Santangelo, A., et al. 2020, Monthly Notices of the Royal Astronomical Society, 491, 1851

Ji, L., Staubert, R., Ducci, L., et al. 2019, Monthly Notices of the Royal Astronomical Society, 484, 3797

Kendziorra, E., Mony, B., Kretschmar, P., et al. 1992, in Frontiers Science Series, ed. Y. Tanaka & K. Koyama, 51

Klochkov, D., Horns, D., Santangelo, A., et al. 2007, Astronomy Astrophysics, 464, L45

Klochkov, D., Santangelo, A., Staubert, R., & Ferrigno, C. 2008a, Astronomy Astrophysics, 491, 833

Klochkov, D., Staubert, R., Postnov, K., et al. 2008b, Astronomy Astrophysics, 482, 907

Klochkov, D., Staubert, R., Postnov, K., et al. 2015, Astronomy Astrophysics, 578, A88

Klochkov, D., Staubert, R., Santangelo, A., Rothschild, R. E., & Ferrigno, C. 2011, Astronomy Astrophysics, 532, A126

Kong, L. D., Zhang, S., Ji, L., et al. 2021, The Astrophysical Journal Letters, 917, L38

Kretschmar, P., El Mellah, I., Martínez-Núñez, S., et al. 2021, Astronomy Astrophysics, 652, A95

La Parola, V., Cusumano, G., Segreto, A., & D'Aì, A. 2016, Monthly Notices of the Royal Astronomical Society, 463, 185

Lamb, F. K., Pethick, C. J., & Pines, D. 1973, The Astrophysical Journal, 184, 271

Leahy, D. A. 1987, Astronomy Astrophysics, 180, 275

Lewin, W. H. G., van Paradijs, J., & van den Heuvel, E. P. J. 1997, X-ray Binaries

Li, X., Li, X., Tan, Y., et al. 2020, Journal of High Energy Astrophysics, 27, 64

Lipunov, V. M. 1987, Astrophysics of neutron stars

Litwin, C., Brown, E. F., & Rosner, R. 2001, The Astrophysical Journal, 553, 788

Liu, C., Zhang, Y., Li, X., et al. 2020, Science China Physics, Mechanics, and Astronomy, 63, 249503

Malacaria, C., Heyl, J., Doroshenko, V., et al. 2023, Astronomy Astrophysics, 675, A29

Martin, R. G., Nixon, C., Armitage, P. J., Lubow, S. H., & Price, D. J. 2014, The Astrophysical Journal Letters, 790, L34

Meszaros, P. 1992, High-energy radiation from magnetized neutron stars

Mushtukov, A. & Tsygankov, S. 2023, in Handbook of X-ray and Gamma-ray Astrophysics, 138

Mushtukov, A. A., Suleimanov, V. F., Tsygankov, S. S., & Poutanen, J. 2015, Monthly Notices of the Royal Astronomical Society, 447, 1847

Nelson, R. W., Salpeter, E. E., & Wasserman, I. 1993, The Astrophysical Journal, 418, 874

Neumann, M., Avakyan, A., Doroshenko, V., & Santangelo, A. 2023, Astronomy Astrophysics, 677, A134

Oppenheimer, J. R. & Volkoff, G. M. 1939, Physical Review, 55, 374

Parmar, A. N., White, N. E., Stella, L., Izzo, C., & Ferri, P. 1989, The Astrophysical Journal, 338, 359

Parsotan, T., Laha, S., Palmer, D. M., et al. 2023, The Astrophysical Journal, 953, 155

Reig, P. 2011, Astrophysics and Space Science, 332, 1

Reig, P. & Coe, M. J. 1999, Monthly Notices of the Royal Astronomical Society, 302, 700

Reig, P. & Nespoli, E. 2013, Astronomy Astrophysics, 551, A1

Schönherr, G., Wilms, J., Kretschmar, P., et al. 2007, Astronomy Astrophysics, 472, 353

Staubert, R., Ducci, L., Ji, L., et al. 2020, Astronomy Astrophysics, 642, A196

Staubert, R., Klochkov, D., Fürst, F., et al. 2017, Astronomy Astrophysics, 606, L13

Staubert, R., Klochkov, D., Vybornov, V., Wilms, J., & Harrison, F. A. 2016, Astronomy Astrophysics, 590, A91

Staubert, R., Klochkov, D., Wilms, J., et al. 2014, Astronomy Astrophysics, 572, A119

Staubert, R., Shakura, N. I., Postnov, K., et al. 2007, Astronomy Astrophysics, 465, L25

Staubert, R., Trümper, J., Kendziorra, E., et al. 2019, Astronomy Astrophysics, 622, A61

Trümper, J., Pietsch, W., Reppin, C., et al. 1977, Mitteilungen der Astronomischen Gesellschaft Hamburg, 42, 120

Tsygankov, S. S., Doroshenko, V., Mushtukov, A. A., Lutovinov, A. A., & Poutanen, J. 2018, Monthly Notices of the Royal Astronomical Society, 479, L134

Tsygankov, S. S., Doroshenko, V., Poutanen, J., et al. 2022, The Astrophysical Journal Letters, 941, L14

Tsygankov, S. S., Lutovinov, A. A., Churazov, E. M., & Sunyaev, R. A. 2006, Monthly Notices of the Royal Astronomical Society, 371, 19

Vybornov, V., Doroshenko, V., Staubert, R., & Santangelo, A. 2018, Astronomy Astrophysics, 610, A88

Vybornov, V., Klochkov, D., Gornostaev, M., et al. 2017, Astronomy Astrophysics, 601, A126

Wang, P. J., Kong, L. D., Zhang, S., et al. 2022, The Astrophysical Journal, 935, 125

Zhang, S.-N., Li, T., Lu, F., et al. 2020, Science China Physics, Mechanics, and Astronomy, 63, 249502